Physics – Uspekhi **47** (8) 749 – 788 (2004)

REVIEWS OF TOPICAL PROBLEMS PACS numbers: **05.40. – a**, 05.45.Df, **05.65. + b**, **94.30. – d**

Fractal topology and strange kinetics: from percolation theory to problems in cosmic electrodynamics

L M Zelenyĭ, A V Milovanov

DOI: 10.1070/PU2004v047n08ABEH001705

Contents

L M Zelenyĭ, A V Milovanov
Space Research Institute, Russian Academy of Sciences
ul. Profsoyuznaya 84/32, 117997 Moscow, Russian Federation
Tel. (7-095) 333 45 34
E-mail: lzelenyi@iki.rssi.ru; amilovan@mx.iki.rssi.ru

Received 4 July 2003, revised 30 March 2004
Uspekhi Fizicheskikh Nauk **174** (8) 809 – 852 (2004)
Translated by K A Postnov; edited by A M Semikhatov

Abstract. The goal of this review is to outline some unconventional ideas behind new paradigms in the modern theory of turbulence. Application of nonstandard, topological methods to describe the structural properties of the turbulent state is considered and the transition to kinetic equations in fractional derivatives for describing the microscopic behavior of a medium is examined. Central to the discussion is the concept of the percolation constant $\mathcal{C} \approx 1.327\ldots$, a universal parameter describing the topology of nonequilibrium (quasi)stationary states

in complex nonlinear dynamical systems allowing self-organized critical behavior. Much attention is given to the formation of power-law energy density spectra in turbulent media. A number of topical problems in modern cosmic electrodynamics, including the self-consistent fractal model of a turbulent current sheet, substorm dynamics, and the formation and dynamical evolution of large-scale magnetic fields in the solar photosphere and interplanetary space, are also discussed.

1. Introduction

The development of modern physics (both theoretical and experimental) in many respects relies on the notion of sets with noninteger dimensions. The concept of fractional dimension was first introduced in papers by Hausdorff [1] and Besicovitch [2], which were preceded by studies by outstanding mathematicians of the end of the 19th and the beginning of the 20th centuries, such as Cantor, Weierstrass, Peano, Koch, and Sierpinski. The foundations of the topological theory of dimension were formulated by the remarkable Russian mathematician P S Uryson, who tragically died at the age of 26 in 1924. The generalized (fractal) dimension plays the key role in abstract mathematics, in particular in number theory [3 – 5].

The term fractal dimension entered the physical lexicon about 25 years ago starting from the fundamental studies on geometry of random processes by Mandelbrot [6 – 8]. One of Mandelbrot's undeniable contributions was the demonstration that a broad diversity of phenomena lead to formation of fractal structures, as well as an original definition of a fractal set as an object whose parts are in some sense similar to the whole [9]. Classic examples of fractals include indented shores [6], random time series [7], river-beds [8], trajectories of Brownian particles [8], etc.

Presently, the notion of fractals is recognized to be a paradigm in modern theoretical physics. Numerous studies of fractals have appeared in many basic branches of physics, such as nonequilibrium thermodynamics [10, 11], cosmology [12 – 14], dynamical chaos theory [10, 15, 16], hydrodynamic turbulence [10, 17, 18], and investigations of phase transitions [19, 20] and transport phenomena [21 – 23]. The rich applications of fractal geometry are discussed in essay [24] and monographs [25 – 28]. Mathematical foundations of modern fractal geometry can be found in [9, 29, 30].

Sets describing the geometry of percolation constitute an important class of fractal objects. By percolation, we mean random propagation of a fluid through a medium; the abstract notions of the 'fluid' and 'medium' can be interpreted differently depending on the physical meaning of the problem [9]. An extensive literature is devoted to the percolation theory, see, e.g., monographs [9, 31 – 33] and reviews [34 – 37]. Percolation is a critical process [36], i.e., it assumes the existence of a certain threshold below which the propagation of the liquid is restricted within a finite area of the medium. Near the threshold, the percolation occurs on a fractal set with the geometry entirely determined by the critical laws. The critical condition renders the geometric characteristics of the fractal independent on the microscopic properties of the medium. This phenomenon can be interpreted as the universality of fractal geometry of percolating sets at the percolation threshold. The most conspicuous formulation of the universality property is known as the Alexander – Orbach (AO) conjecture that the spectral dimension of a fractal set (i.e., the effective number of its 'internal' degrees of freedom) near the percolation transition is equal to 4/3 for all embedding (integer) dimensions n not less than two [37, 38].

The proof of the AO conjecture in higher dimensions $n \geqslant 6$ is based on the mean-field theory [21, 22, 37, 39]. The mean-field theory approximation corresponds to percolation processes on Cayley trees (referred to as Bethe lattices in physics). A Cayley tree is a graph without loops with the same number of branches at all knots. The embedding space with $n \geqslant 6$ is ample enough for the branches of the Cayley trees to avoid each other (i.e., they do not form loops – closed cycles). In lower dimensions $2 \leqslant n \leqslant 5$, not enough room is available: Cayley trees join in a 'tangle' and the mean-field approximation is invalidated due to the 'destructive' role of closed orbits, which give a nonrenormalizable contribution to the propagator at the percolation threshold [21]. The problem is aggravated by the fact that abandoning the mean-field description in $2 \leqslant n \leqslant 5$ affects the conceptual basics of fractal geometry [37], including the fractal definition itself [9]. The lack of ideas in this field has made the general analytical proof (or disproof) of the AO conjecture (as well as its possible modifications in $2 \leqslant n \leqslant 5$) one of the most difficult problems in the fundamental theory of percolation.

The progress here has been achieved in the context of the topological theory of fractal sets, originally proposed in papers [40 – 43]. The key point was the merging of the 'traditional' fractal geometry [9, 28] with the differential topology [44 – 46], which has led to the appearance of principally new mathematical concepts [40], such as a fractional Euclidean space and a fractal manifold. Percolating fractal structures turned out to be what can be called a fractional disk, by which we mean the existence of a connecting diffeomorphic (smooth and one-to-one) mapping. At the percolation threshold, the spectral dimension of the disk is minimal, and the condition of linear connectedness (i.e., the integrity of the disk as a topological object) must be satisfied. The solid angle that can be subtended by such a disk is in any case not smaller than π, i.e., the angle at the base of a semi-circle connecting the north and south poles (see Section 2, where we discuss the corresponding geometrical constructions in more detail). In order for the disk to subtend such a small angle, its spectral dimension must be sufficiently low; its precise value (to be denoted by $\mathcal{C}$) is an irrational number approximately equal to 1.327... . The obtained quantity has a fundamental mathematical meaning — it is the minimal fractional number of the degrees of freedom that a particle must have in order to reach an infinitely remote point by randomly walking in Euclidean space. To embed a disk with the spectral dimension $\mathcal{C} \approx 1.327\ldots$ into a Euclidean space of dimension n, not more than $n = 5$ embedding dimensions are required. In papers [41 – 43], the number $\mathcal{C} \approx 1.327\ldots$ is called the percolation constant; essentially, it is a new fundamental constant that characterizes the most general topological properties of fractals, such as connectedness. Because the value of the percolation constant is different from 4/3, the topological theory of fractals disproves the AO conjecture in lower dimensions $2 \leqslant n \leqslant 5$. It can be said that the AO conjecture is valid only in higher dimensions $n \geqslant 6$, where the mean field approximation holds. The deviation of the value $\mathcal{C} \approx 1.327\ldots$ from 4/3 in $2 \leqslant n \leqslant 5$ provides the convergence of the renormalization-group expansion [22] of thermodynamic quantities at the percolation threshold.

The interest in the topological properties of percolating fractal structures arises not only (and even not so much) because of the universality of critical phenomena in random media noted above but also because it is necessary to understand the most common relations in the behavior of complex dynamical systems revealing a self-consistent tendency to critical regimes. In such systems, we deal with the existence of nonequilibrium (quasi)-stationary states (NESS's) having the topology of a percolating fractal set. Examples include multi-scale interaction of fields and currents in the distant Earth's magnetotail [47], self-organization processes in low-temperature magnetized plasma [48], and the formation of a fractal 'web' of conducting elements in self-organizing organic polymers [43].

As a rule, the transition to a NESS is related to the simultaneous development of numerous instabilities, 'interfering' with each other. As nonlinear effects are enhanced, different instabilities lose their 'individuality' by transforming into some universal collective 'mode'. The idealized properties of this mode are independent of the kinetics of the 'partial' linear modes at the initial stages of the system evolution (Fig. 1). This ideology underlies the geometrical description of turbulence, which is used in some applications in cosmic electrodynamics [47, 49 – 54]. We note that the universality of the collective mode is nothing but the universality of the NESS fractal geometry in the context of the percolation transition.

The stabilization of a system near the NESS is perceived by the observer as a transition into a turbulent state, which is adequate for the appearance of complex space distributions in the critical domain [50]. It is important to understand that this type of 'turbulence' is fully determined by self-organization processes in the system and is the signature of 'order' rather than 'chaos'. The large-scale order of a turbulent state can then be identified with the generalized symmetries of a fractal disk diffeomorphic to a fractal set at the percolation threshold [40]. The structural stability of the NESS as a 'symmetric' turbulent phase is maintained due to multi-scale correlations, which play the crucial role in strongly nonlinear regimes [55 – 58]. In statistically homogeneous isotropic systems, the appearance of large-scale ordering assumes the divergence of the correlation length for the fractal distribution:

$$\xi \to \infty . \tag{1.1}$$

Condition (1.1) can be satisfied along two or three directions, for example in the plane perpendicular to the external homogeneous magnetic field. Because the stabilization of the NESS one way or another is due to the existence of a local extremum (minimum) of the free energy, condition (1.1), related to the effects of self-organization of a turbulent ensemble, simultaneously requires its fractal geometry to be 'minimal' (critical), which corresponds to the percolation transition in the medium.

Long-range correlation effects manifest themselves in a 'strange' (non-Gaussian) behavior of kinetic processes near the NESS; kinetic anomalies have been discovered, in particular, in modeling transport processes [21, 59 – 64], in determining spectra of excited states [37, 38], in studies of chemical reactions [22, 65], and in test particle acceleration experiments [66]. The strangeness and fractality can be considered to be mutually consistent characteristics of one phenomenon — the self-organization of a system towards a nonequilibrium turbulent state whose dynamics is fully controlled by multi-scale correlation interactions.

The aim of this review is to acquaint the reader with the principal ideas and methods underlying the topological description of turbulence. The selection of material (which was a difficult task in preparing the review!) was determined both by scientific interests of the authors and by the relevance

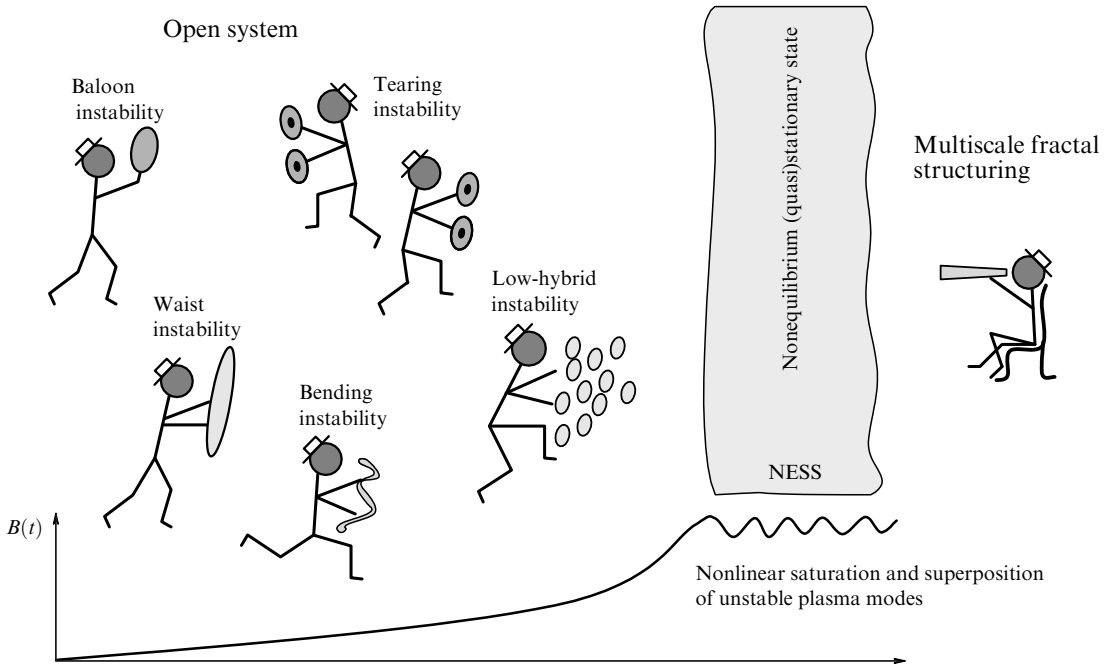

Figure 1. Development of a universal collective 'mode' corresponding to the transition of complex nonlinear dynamic systems towards a nonequilibrium (quasi)-stationary state. Examples are the processes of nonlinear stabilization and saturation of unstable plasma modes in the distant magnetotail of the earth (see Section 7 for more details). The characteristic dependence of the nonlinear amplitude of magnetoplasmic waves B on time is shown in the bottom part of the figure.

of most problems in the modern theory of turbulence, including its applications in cosmic electrodynamics and plasma physics. The structure of the review is as follows. The most important definitions and theorems that characterize topological properties of fractal structures are collected in Section 2. In the first reading, mathematical details, for example, the proof of the universal value theorem, can be omitted. The transition from topology to dynamics is described in Section 3, where we consider strangle transport processes on percolating fractal sets. The transport kinetics is discussed in Section 4 using a nontraditional formalism that invokes the notion of derivatives of an arbitrary (fractional) order. In Section 5, we describe the concept of self-organized criticality (SOC), which became a paradigm in the modern nonlinear physics. As an illustration, in Section 6, we analyze spectral properties of magnetoplasmic turbulence in the Earth's magnetotail. A fractal model of the self-consistent current sheet, which describes the electrodynamic system of the magnetotail near the marginal nonequilibrium (quasi)-stationary state, is constructed in Section 7. In the same section, a model for magnetosphere substorm as a topological phase transition on a percolating fractal network is presented. Particle acceleration processes near the NESS are considered in Section 8, where the notion of a strange Fermi process is introduced (as a fractal counterpart of the random acceleration model). The self-consistent kinetic description of the NESS is given in Section 9 with a focus on nonlinear generalizations of dynamical equations in fractional derivatives. In Section 11, we again consider nonlinear generalizations. We derive the fractional parabolic equation (with account of the strange diffraction phenomenon), the fractional nonlinear Schrödinger equation (as a particular case of the parabolic one), and the fractional Ginzburg – Landau equation, which follows from nonlocal expansion of the system free energy near a second-order phase transition point. In Section 10, aggregation and growth effects in nonequilibrium systems are considered. In that Section, we briefly describe structural models of sun spots and the interplanetary magnetic field. In Section 11, we discuss wave processes on percolating fractal sets, including self-focusing and self-squeezing phenomena of fracton excitations (i.e., proper (quasi)acoustic modes of a fractal medium). We also discuss the application of fractons to the dynamical model of solar wind, which admits the formation of 'Kolmogorov' turbulence spectra at earlier (compared to the structural models) stages of the plasma outflow from the corona. The principal points considered in the review are summarized in the Conclusion (Section 12).

2. Basic definitions and theorems

2.1 Definition of the Hausdorff dimension

We consider a set of points $F \subseteq E^n$ embedded in a Euclidean space E^n of dimension $n \geqslant 1$. By definition, the number n (called the embedding dimension) takes positive integer values 1, 2, 3, ... Next, let $\varepsilon > 0$ be an arbitrarily small number. We define an n-dimensional ε-cube in E^n as the topological product $\bar{I}(\varepsilon) \times \ldots [n] \ldots \times \bar{I}(\varepsilon)$, where $\bar{I}(\varepsilon)$ denotes a closed segment of length ε. (The topological product $A \times B$ of sets A and B is given by all possible pairs of points (x, y), where $x \in A$ and $y \in B$ [46]). Let $\mathcal{N}_n(\varepsilon)$ be the minimum number of n-dimensional ε-cubes covering the set of points F with accuracy ε. Following Kolmogorov [67], we define the Hausdorff fractal dimension of the set F as

$$d_\mathrm{f} = d_\mathrm{f}[F] = -\lim_{\varepsilon \to +0} \frac{\ln \mathcal{N}_n(\varepsilon)}{\ln \varepsilon} \,. \tag{2.1}$$

It is easy to see that the Hausdorff dimension of the Euclidean space E^n is $d_\mathrm{f} = n$. In general, $d_\mathrm{f} \leqslant n$ in accordance with the meaning of the embedding $F \subseteq E^n$. Moreover, for any subset $F' \subseteq F$, the inequality $d_\mathrm{f}[F'] \leqslant d_\mathrm{f}[F]$ holds. It can be shown that definition (2.1) (in the sense of Kolmogorov's paper [67]) is equivalent to the definition of the Hausdorff – Besicovitch dimension [1, 2], which is an alternative to (2.1). Only some pathological cases that have no physical interest provide an exception [36]. We note that the Hausdorff dimension d_f can take arbitrary real values, including negative (as a characteristic of how empty the set is) and irrational ones.

The limit in Eqn (2.1) exists for sets F that have the self-similarity, or scale invariance property. This property can be realized with different exponents along different directions in space. In that case, the fractal is said to be self-affine. Fractals are subdivided into deterministic and random. An example of a deterministic fractal is given by the Koch curve, which is constructed by infinite repetition of the operation of splitting

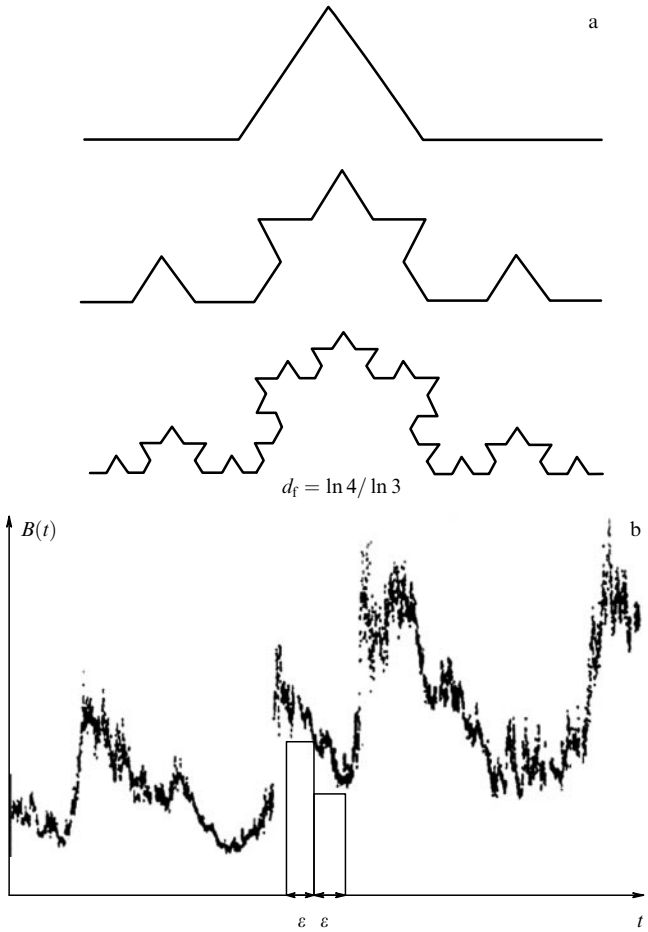

Figure 2. (a) Consecutive steps of the Koch curve construction. The iterative process ultimately results in the self-affine fractal curve with the Hausdorff dimension $d_\mathrm{f} = \ln 4 / \ln 3$. (b) The example of a statistically self-affine time series. The function $B(t)$ represents the interplanetary magnetic field as measured by the ISEE-3 satellite. Approximating $B(t)$ by a histogram with step ε, we find that the length of the latter (treated as the sum of the corresponding variations $\sum_i |B(t_i + \varepsilon) - B(t_i)|$) diverges (as $\varepsilon \to 0$) in accordance with the power law $\propto \varepsilon^{-S}$. The Hausdorff dimension of the set $B(t)$ is $d_\mathrm{f} = 1 + S$.

a segment in three equal parts and constructing an equilateral triangle on the middle part at a progressively smaller scale (Fig. 2a). It is easy to verify that the Hausdorff dimension of the Koch curve is $d_f = \ln 4/\ln 3 \approx 1.26\ldots$. Unlike deterministic fractals, most fractal objects occurring in nature are somehow related to stochastic processes and are random in this sense. As an example, we consider the stochastic series shown in Fig. 2b, which represents variations of the interplanetary magnetic field in a wide range of time scales [68]. Such series are said to be statistically self-affine fractal curves. A statistically self-affine curve is a set of points $\mathcal{I}_S(t)$ such that $h^{S-1}\mathcal{I}_S(ht)$ is statistically equivalent to $\mathcal{I}_S(t)$ for any real h [9]. The parameter h determines a scale transformation of the curve $\mathcal{I}_S(t)$ with the similarity exponent $0 \leqslant S \leqslant 1$. The curve $\mathcal{I}_S(t)$ has a self-affine structure at all scales determined by the parameter t, which is assumed to be continuous. Approximating the set of points $\mathcal{I}_S(t)$ by a histogram with step ε (Fig. 2b), it is easy to show [69] that the length of the histogram $\sum_i |B(t_i+\varepsilon) - B(t_i)|$ diverges as ε^{-S} for $\varepsilon \to 0$. It follows from definition (2.1) that the Hausdorff dimension of the set $\mathcal{I}_S(t)$ is

$$d_f[\mathcal{I}_S] = 1 + S. \tag{2.2}$$

For smooth curves, we have $S = 0$ and $d_f[\mathcal{I}_0] = 1$. For an arbitrary continuous self-affine curve $\mathcal{I}_S(t)$, the Hausdorff dimension $d_f[\mathcal{I}_S]$ ranges from one to two.

As a rule, scale-invariant sets fill only a part of the embedding Euclidean space E^n. Domains of E^n that do not belong to F are considered voids, which can lie both inside and outside F. (It is impossible to escape from the inner voids without crossing F.) A consequence of the existence of voids is a power-law decrease of the mean density of the set F in E^n as a function of the scale length r (Fig. 3a). Indeed, we assume for simplicity that the fractal set F is 'isotropic' (i.e., the similarity exponents coincide along all directions). Then the effective 'mass' contained inside a hypersphere of radius r grows as r^{d_f} with r, where d_f is the Hausdorff fractal dimension. Similarly, the effective 'mass' of the embedding Euclidean space E^n grows as r^n, where n is the Hausdorff dimension of E^n, coincident with its topological dimension. Consequently, the density of the fractal F in E^n behaves as

$$\Im[F](r) = \Im_0 \times \frac{r^{d_f}}{r^n} = \Im_0 \times r^{d_f - n}, \tag{2.3}$$

where $\Im_0$ is a normalization constant. Expression (2.3) plays an important role in applications of fractal geometry, when real physical objects are approximated by fractal structures (see Section 7).

The definition of the Hausdorff dimension in (2.1) leads to a conceptual generalization of the notion of measure in modern geometry [8]. Indeed, the classic notions such as length, area, and volume are just 1-measure, 2-measure, and

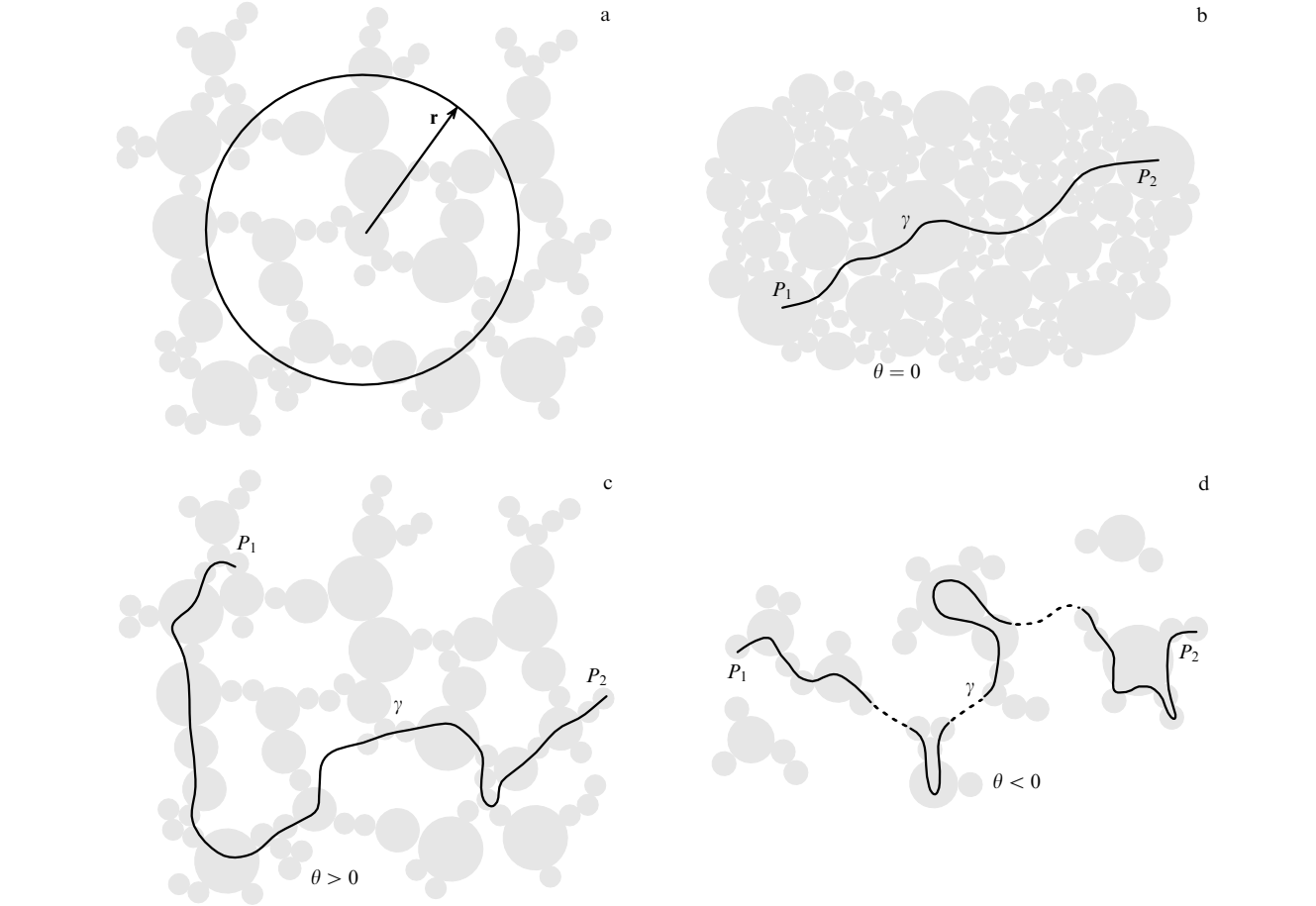

Figure 3. (a) Definition of the Hausdorff dimension d_f. The number of the fractal structural elements inside a hypersphere of radius r is proportional to r^{d_f}. Definition of the connectivity index: (b) $\theta = 0$, the Hausdorff dimension of the geodesic γ connecting points P_1 and P_2 is equal to one; (c) $\theta > 0$, the Hausdorff dimension of the geodesic γ connecting points P_1 and P_2 is necessarily greater than one; (d) $\theta < 0$, the geodesic γ connecting points P_1 and P_2 is everywhere discontinuous and its Hausdorff dimension is strictly less than one.

3-measure of a set, respectively. With the Hausdorff dimension introduced in (2.1), it is possible to consider an arbitrary real measure of a set, or its d_f-measure. The d_f-measure has the following important property [36]. The only nonzero finite measure of a fractal set of dimension d_f is its d_f-measure. In particular, 1) any d'_f-measure of a fractal set is zero for $d'_f > d_f$; 2) any d'_f-measure of a fractal set is infinite for $d'_f < d_f$. An illustration is provided by the divergence of the length (i.e., of the 1-measure, $d'_f = 1$) of the histogram approximating the statistically self-affine curve in Fig. 3.

We emphasize that the definition of the Hausdorff dimension of a fractal in (2.1) essentially involves the embedding $F \subseteq E^n$. Indeed, the value of d_f is determined through the capacity of the covering of F by n-dimensional ε-cubes, and is therefore an external characteristic of the fractal, a characteristic related to E^n. At the same time, the Hausdorff dimension d_f does not account for the inherent topological properties of a fractal set, which are not directly related to the embedding $F \subseteq E^n$. This feature is manifested in that the Hausdorff dimension of a fractal is not a topological invariant — this dimension can change under homeomorphic (continuous one-to-one) mappings of fractal structures. For example, the Koch curve in Fig. 2a is homeomorphic to the unit interval $\bar{I}$, but its Hausdorff dimension $d_f = \ln 4/\ln 3 \approx 1.26\ldots$ is different from $d_f[\bar{I}] = 1$. This is because the homeomorphism of the Koch curve on I is not smooth (due to acute angles at the bending points). Under smooth (diffeomorphic) mappings, the Hausdorff dimension d_f is preserved [16].

2.2 Definition of the connectivity index

To describe the topology of a fractal set as such (irrespective of the embedding in a Euclidean space E^n), we introduce a new geometric characteristic of a fractal called the connectivity index. Let P_1 and P_2 be two arbitrary points of a fractal set F in a general position [37], and γ be a path connecting P_1 and P_2. (We recall that a path in F is a continuous mapping γ: $\bar{I} \to F$ of the closed unit interval $\bar{I} \equiv [0, 1]$ into F.) The points $P_1 = \gamma(0)$ and $P_2 = \gamma(1)$ are identified with the initial and final points of the path, respectively. Because F is a fractal, the mapping γ: $\bar{I} \to F$ defines a certain self-affine curve lying in F. In general, there exist infinitely many paths γ connecting P_1 and P_2 in F. We choose the path with the minimal Hausdorff dimension. We next consider all possible homeomorphisms $f: F \to F'$ that transform the fractal F into a fractal F'. (It is sufficient that $f: F \to F'$ does not violate the scale invariance property; the Hausdorff dimensions of the fractals F and F' may be different: $d_f[F] \neq d_f[F']$.) Clearly, the image of the path $\gamma \subset F$ under the homeomorphism f is a path $\gamma' \subset F'$ connecting the images of points P_1 and P_2. Among all paths γ', we select the one with the minimal Hausdorff dimension. Let d_θ be the number thus obtained. We have

$$d_\theta = \inf_{f:\,\gamma \to \gamma'} \inf_{\gamma} d_f[\gamma : P_1 \to P_2]\,. \tag{2.4}$$

The parameter d_θ has the meaning of the Hausdorff dimension of geodesic lines on F. We further represent the parameter d_θ in the form $d_\theta \equiv (2 + \theta)/2$. The value $\theta = \theta[F]$ is called the connectivity index of the fractal set F,

$$\theta = 2(d_\theta - 1)\,. \tag{2.5}$$

Definition (2.4) implies that the index θ is a topological invariant of the fractal F. In other words, the parameter θ describes a class of fractal sets that are identified with each other via homeomorphic mappings; then $\theta[F] = \theta[F']$ for all $f: F \to F'$, where f is a homeomorphism of F on F'.

Obviously, the connectivity index θ is zero for any smooth set, including Euclidean spaces E^n with $n \geqslant 1$ (Fig. 3b). Indeed, $d_\theta = 1$ for an arbitrary smooth structure, and hence $\theta = 0$. Self-affine fractal curves (for example, the Koch curve) are examples of fractal sets with a nontrivial Hausdorff dimension and zero connectivity index. The condition

$$\theta = 0 \tag{2.6}$$

for self-affine fractal curves follows from the existence of a homeomorphism $f: \mathcal{I}_S(t) \to I$ of the curve $\mathcal{I}_S(t)$ on the open unit interval $I \equiv (0, 1)$ (or on the one-dimensional Euclidean space E^1 equivalent to I). If a fractal curve contains self-crossings, the homeomorphic relation to I is violated. In that case, the index $\theta > 0$.

For dimensions $n \geqslant 2$, the connectivity index θ is determined by the topology of voids formed by the set F. It is then essential to determine whether the voids are internal or external. If F does not contain internal voids, then $\theta[F] = 0$. In this case, F can be extended to the entire E^n by 'inflating' the fractal from inside (as a ball in which the pressure has dropped). It can be claimed that $\theta = 0$ for fractal clusters without internal voids.

The situation changes radically if there are internal voids. Because a homeomorphism prohibits any gluing when transforming a set, it is impossible to eliminate voids, whatever deformations (allowed by the definition) are applied to a fractal. We note that in constructing the curve γ, the internal voids should be rounded on all spatial scales such that γ lies everywhere within F. Therefore, the curve γ cannot be straightened out by homeomorphic deformations of the fractal F. As a result, γ remains a wavy line with the Hausdorff dimension limited from below by the value $d_\theta > 1$. Correspondingly, $\theta > 0$ for fractal sets with internal voids (Fig. 3c).

The above consideration somehow assumes that the set F is path-connected. A set is called path-connected if along with any pair of points it also contains a path connecting these points [46]. For path-connected sets, $d_\theta \geqslant 1$ and $\theta \geqslant 0$. The Hausdorff dimension of a path-connected fractal set is such that $d_f \geqslant d_\theta \geqslant 1$. For fractal (Cantor) sets that are not path-connected, the condition $0 \leqslant d_f < d_\theta < 1$ holds. The self-similarity property suggests that such fractal sets are discontinuous at each point. The Hausdorff dimension of a 'path' γ discontinuous everywhere in fractal structures must be strictly less than unity (Fig. 3d). From Eqn (2.5), we obtain the index $\theta < 0$ for fractals that are not path-connected. Finally, there is an interesting class of fractal objects with the Hausdorff dimension $d_f \geqslant 1$ and a negative connectivity index $\theta < 0$. Such sets, called asymptotically path-connected, are considered in [70].

Therefore, the sign of the connectivity index, $\operatorname{sign}\theta$, is determined by the path-connectedness (or disconnectedness) of the set F. We note that the linear connectedness (disconnectedness) of a set is a topological invariant [46], which is consistent with the invariance of $\operatorname{sign}\theta$. The invariance of the index θ itself under homeomorphic mappings $f: F \to F'$ of a fractal to a fractal enhances the statement in [46] for fractal sets [41].

2.3 Definition of the spectral fractal dimension

Following [40], we introduce an axiomatic definition of the spectral dimension of a fractal. We say that the spectral

fractal dimension d_s of a fractal set F is the ratio of the Hausdorff dimension $d_f = d_f[F]$ to the minimal Hausdorff dimension d_θ of paths connecting images of generic points $P_1 \in F$ and $P_2 \in F$ under all possible homeomorphisms $f: F \to F'$ transforming the fractal F to a fractal F'. We have

$$d_s \equiv \frac{d_f}{d_\theta} = \frac{2d_f}{2+\theta}\,. \tag{2.7}$$

The spectral fractal dimension d_s determines the measure of a fractal set $F \subseteq E^n$ with respect to the minimal measure of paths that allow the bypassing of the internal voids in F. The value of d_s is a 'mixed' characteristic of the fractal, which accounts for both the properties of the embedding $F \subseteq E^n$ into a Euclidean space E^n and the inherent structure of the fractal set.

It is easy to see that for path-connected fractals, a path γ connecting arbitrary points $P_1 \in F$ and $P_2 \in F$ of a fractal set F is a subset of F, i.e., $\gamma \subseteq F$. Indeed, using the general properties of the Hausdorff dimension, we obtain $d_f[\gamma : P_1 \to P_2] \leqslant d_f[F]$. In accordance with Eqn (2.4), the path-connectedness implies that the value of $d_f[\gamma : P_1 \to P_2]$ is limited from below by the value of d_θ. From the inequality $d_f[\gamma : P_1 \to P_2] \leqslant d_f[F]$, we have $d_\theta \leqslant d_f$, and hence $d_s \geqslant 1$. Finally, for linearly connected fractals, Eqns (2.5) and (2.7) imply that

$$d_f \geqslant d_\theta \equiv \frac{2+\theta}{2} \geqslant 1\,, \qquad d_s \geqslant 1\,. \tag{2.8}$$

Taking the second inequality in (2.8) into account, we readily obtain $d_f \geqslant d_s$. For continuous self-affine fractal curves without self-crossings, we see from Eqn (2.6) that $\theta = 0$, $d_\theta = 1$, $d_s = d_f \geqslant 1$, For fractal sets that are not path-connected, a relation inverse to Eqn (2.8) holds,

$$d_f < d_\theta \equiv \frac{2+\theta}{2} < 1\,, \qquad d_s < 1\,, \tag{2.9}$$

and hence $d_f < d_s$. It can be shown [40] that the spectral dimension d_s determines the number of pairwise orthogonal directions on the fractal set F. This feature underlies the axiomatic definition of a fractal manifold as the most general concept of a fractal structure [40]. In applications, it is convenient to treat the parameter d_s as an effective number of the degrees of freedom in fractal geometry [23].

2.4 The universal value theorem

The spectral dimension of a contractible fractal set at the percolation threshold is equal to $\mathcal{C} \approx 1.327\ldots$ for all $2 \leqslant n \leqslant 5$ [40, 70]:

$$d_s = \mathcal{C} \approx 1.327\ldots \qquad (2 \leqslant n \leqslant 5)\,. \tag{2.10}$$

We recall that a set F is called contractible if the identical mapping $F \to F$ is homotopic to the mapping transforming the entire F into a point [46]. (Homotopy means the existence of a continuous parameterization whereby different mappings $F \to F$ are united into an equivalence class.) For example, the disk $\bar{D}^n$ is contractible for any $n \geqslant 1$, while the sphere S^{n-1} bounding the disk $\bar{D}^n$, as well as the torus $T^n \sim S^1 \times \ldots [n] \ldots \times S^1$, which is diffeomorphic to the direct product of n circles S^1, are not contractible because of the presence of internal voids. The contractibility condition is similar to the assumption of the absence of loops in constructing Cayley trees in the mean-field theory [21, 22, 37, 39]. The value of $\mathcal{C}$ in the statement of the theorem is determined as the smaller of two possible roots of the transcendental equation [40]

$$\mathcal{C}\,\frac{\pi^{\mathcal{C}/2}}{\Gamma(\mathcal{C}/2+1)} = \pi\,, \tag{2.11}$$

where Γ is the Euler gamma-function. The universal value theorem allows us to consider the parameter $\mathcal{C} \approx 1.327\ldots$ a fundamental topological constant characterizing the percolation transition geometry in lower dimensions $2 \leqslant n \leqslant 5$. Following [41], we refer to $\mathcal{C}$ as the 'percolation constant'. The percolation constant determines the minimal fractional number of the degrees of freedom that a particle must have to reach the infinitely remote point in the Euclidean space E^n whose dimension is in the interval from 2 to 5. The set of points visited by the particle then forms a percolating fractal network with the spectral dimension $d_s = \mathcal{C} \approx 1.327\ldots$.

The general proof of the universal value theorem is considered in [40] and can be split into 'easy' and 'difficult' parts [70]. The proof of the easy part requires the preliminary introduction of nonstandard notions such as the (closed) d_s-dimensional fractional disk $\bar{D}^{d_s}$ and (d_s-1)-dimensional fractional sphere S^{d_s-1}, which represents an effective (visible) surface of the disk $\bar{D}^{d_s}$. Formally,

$$\bar{D}^{d_s}: \quad z_1^2 + \ldots + z_{d_s}^2 \leqslant 1\,, \tag{2.12}$$

$$S^{d_s-1}: \quad z_1^2 + \ldots + z_{d_s}^2 = 1\,, \tag{2.13}$$

where the components $z_1, \ldots, z_{d_s}$ correspond to the 'Cartesian' coordinates in d_s dimensions. The sets $\bar{D}^{d_s}$ and S^{d_s-1} are examples of fractal manifolds characterizing the topology of percolation in statistically homogeneous isotropic systems [40]. The smooth manifolds $\bar{D}^n$ and S^{n-1} known from differential geometry can be considered the limit of the respective fractal manifolds $\bar{D}^{d_s}$ and S^{d_s-1} as $d_s \to n$. We note that in the general case, the sphere S^{d_s-1} does not coincide with the total topological boundary $\partial\bar{D}^{d_s}$ of the disk $\bar{D}^{d_s}$ because the manifold $\partial\bar{D}^{d_s}$ can contain elements shading each other. In that case, the visible surface $S^{d_s-1} \subseteq \partial\bar{D}^{d_s}$ is a subset of $\partial\bar{D}^{d_s}$. Accordingly, for the Hausdorff dimensions $d_f[S^{d_s-1}]$ and $d_f[\partial\bar{D}^{d_s}]$, we have $d_f[S^{d_s-1}] \leqslant d_f[\partial\bar{D}^{d_s}]$. For integer $d_s = n$, the standard sphere is $S^{n-1} \sim \partial\bar{D}^n$, and hence $d_f[S^{n-1}] = d_f[\partial\bar{D}^n] = n-1$.

The key point is the construction of a path $\tilde{\gamma}$ that covers the entire disk $\bar{D}^{d_s}$ everywhere densely and passes through each point once and only once (Fig. 4). Below the threshold, this construction is impossible because the set $\bar{D}^{d_s}$ is not path-connected by definition. In that case, the curve $\tilde{\gamma}$ is discontinuous everywhere. Above the threshold, the percolating domain becomes 'too large'; an everywhere dense covering of such a region is similar to constructing a Peano curve, which inevitably contains points of self-intersection. It can be said that at the percolation threshold, the disk $\bar{D}^{d_s}$ is indistinguishable from the path $\tilde{\gamma}$ that is related to the existence of the percolation transition in the system.

Next, it is easy to see that $\tilde{\gamma}$ subtends the same solid angle as the entire disk $\bar{D}^{d_s}$; this angle, however, cannot be smaller than π, i.e., the solid angle at the base of a semicircle (see Fig. 4). The statement follows from the analysis of all possible continuous deformations of the curve $\tilde{\gamma}$ whose endpoints are fixed at the opposite poles of the sphere S^{d_s-1} [40]. Taking into account that the sphere S^{d_s-1} is viewed from the center of

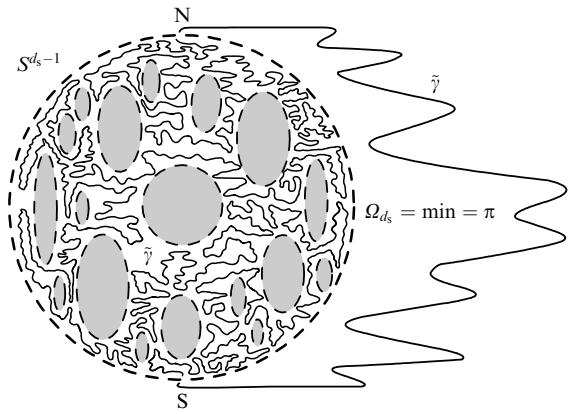

Figure 4. The construction of the limiting path $\tilde{\gamma}$ densely covering the ball $\bar{D}^{d_s}$ everywhere at the percolation threshold.

the disk $\bar{D}^{d_s}$ at the solid angle

$$\Omega_{d_s} \equiv d_s \frac{\pi^{d_s/2}}{\Gamma(d_s/2+1)}\,, \tag{2.14}$$

we find that $\Omega_{d_s} \geqslant \pi$. On the other hand, the criticality condition (i.e., the condition for a percolating set to be minimal) requires $\Omega_{d_s} = \min$, and hence $\Omega_{d_s} = \pi$. Identity (2.11) is evident from the obtained relation. We note that the condition $\Omega_{d_s} = \min = \pi$ can be treated as the topological definition of the percolation threshold.

Embeddings of fractional spheres into the Euclidean space E^n are discussed in the difficult part of the theorem, where the general restriction $2 \leqslant n \leqslant 5$ on the topological dimension n is obtained [40]. The proof of the restriction $2 \leqslant n \leqslant 5$ is based on constructing a smooth two-dimensional envelope of $\bar{D}^{d_s}$ and subsequently applying the weak Whitney embedding theorem [45].

In the usual three-dimensional space, the fractional disk can be visualized as the crown of a large tree, which, although it blocks direct sunlight, is sufficiently transparent to allow one to see the sky. To see only the crown (without the sky) requires a smaller number of the degrees of freedom than the embedding space dimension. But in order for the crown to shade all the horizon, the number of the degrees of freedom cannot be too small. There is an optimal number of the degrees of freedom when the entire crown has just become visible and the maximum amount of sunlight is simultaneously received. This number determines the spectral dimension of a fractal at the percolation threshold $\mathcal{C} \approx 1.327\ldots$.

2.5 The fractal boundary theorem

At the percolation threshold, the topological boundary $\partial\bar{D}^{d_s}$ is dense everywhere in the fractional disk $\bar{D}^{d_s}$ [42, 43]. In other words, the percolating fractal set $\bar{D}^{d_s}$ at the transition point consists solely of its boundary: $\bar{D}^{d_s} \sim \partial\bar{D}^{d_s}$. Indeed, $\partial\bar{D}^{d_s}$ coincides with the curve $\tilde{\gamma}$ that covers $\bar{D}^{d_s}$ everywhere densely. The equality of the Hausdorff dimensions $d_f \equiv d_f[\bar{D}^{d_s}] = d_f[\partial\bar{D}^{d_s}] = d_f[\tilde{\gamma}]$ at the percolation threshold is a consequence of this theorem.

As noted above (see Section 2.4), the capacity of a fractal set at the transition point cannot be too large, otherwise the path $\tilde{\gamma}$ providing an everywhere dense covering of the disk $\bar{D}^{d_s}$ inevitably includes self-crossing points. The corresponding restriction on the Hausdorff dimension d_f is obtained in [43]:

$$1 \leqslant d_f \leqslant \mathcal{S}_n \equiv \frac{\ln(3^n-1)}{\ln 3} \qquad (2 \leqslant n \leqslant 5)\,. \tag{2.15}$$

The parameter $\mathcal{S}_n \equiv \ln(3^n-1)/\ln 3$ on the right-hand side of Eqn (2.15) is the Hausdorff dimension of the set dubbed the Cantor cheese. It is 'cooked' by taking the n-fold product of complements to 'Cantor dust', the Cantor set of the 'dropped one third' [28, 71]. The two-dimensional ($n = 2$) Cantor cheese is also called the Sierpinski carpet: $\mathcal{S}_2 \equiv \ln 8/\ln 3 \approx \approx 1.89\ldots$. The Sierpinski carpet has a remarkable property: any line that can be embedded into the plane E^2 can also be embedded into the Sierpinski carpet. This feature allows us to consider the Sierpinski carpet as the universal line on the plane [71]. (We recall that in topology, a line is defined as a homeomorphism of the unit interval $\bar{I} \sim [0,1]$. A path without self-crossing points is a line.) Because $\mathcal{S}_2 < 2$, a line covering E^2 everywhere densely does not exist in nature. As is well known [71], an everywhere dense covering of a plane is achieved at the expense of relaxing the global homeomorphicity and passing to the Peano curves with a countable number of self-crossing points. The value $\mathcal{S}_n \equiv \ln(3^n-1)/\ln 3$ can be said to determine the Hausdorff dimension of a maximal fractal set, all of whose points can be visited without self-crossings in the space E^n. Interestingly, there is a line visiting the entire E^∞; this statement follows from $\lim_{n\to\infty}[n/\mathcal{S}_n] = 1$.

3. Strange transport processes

3.1 Transport processes in self-similar fractal structures

We consider a random walk of a point particle in a self-similar fractal set F embedded in the Euclidean space E^n of dimension $n \geqslant 2$. Let k be the effective number of the degrees of freedom on F. Clearly, $k \leqslant n$ because of the embedding $F \subseteq E^n$. Because the spectral dimension d_s determines the number of pairwise orthogonal directions on F, $k \equiv d_s$.

We assume that the particle starts traveling from the origin $\mathbf{r} = 0$ at the time instant $t = 0$. In k dimensions, the probability of the particle returning to the starting point $\mathbf{r} = 0$ within a time interval $t > 0$ is, up to a normalization constant [72],

$$\psi(t,0) \sim t^{-k/2}\,. \tag{3.1}$$

Correspondingly, the number of structural elements of the set F that the particle visits in time t is, by the order of magnitude,

$$\aleph(t) \sim \frac{1}{\psi(t,0)} \sim t^{k/2}\,. \tag{3.2}$$

The characteristic size $r(t)$ of the domain that the particle can visit in the time t can be easily estimated from relation (2.3) for the density of the fractal F in E^n: we have $\aleph(t) \sim r^n\,\Im[F](r) \sim [r(t)]^{d_f}$, where $d_f = d_f[F]$. Therefore,

$$r(t) \sim \left[\aleph(t)\right]^{1/d_f} \sim t^{k/2d_f}\,. \tag{3.3}$$

With the identity $k \equiv d_s$, we find from Eqn (2.7) that

$$r(t) \sim t^{1/(2+\theta)}\,, \tag{3.4}$$

where $\theta \equiv \theta[F]$ is the connectivity index of the set F. The mean-square distance of the particle from the origin increases

with t as

$$\left\langle \mathbf{r}^2(t) \right\rangle = 2\mathcal{D} \times t^{\mu}\,, \tag{3.5}$$

with the normalization constant $\mathcal{D}$ having the meaning of the generalized transport coefficient, and the time exponent is

$$\mu = \frac{d_s}{d_f} = \frac{2}{2+\theta}\,. \tag{3.6}$$

Expression (3.6) was first derived in [59] from the phenomenological analysis of the dc (direct-current) conductivity of percolating clusters. According to Eqn (2.5), the index μ is nothing but the inverse Hausdorff dimension of geodesic lines on F, namely $\mu = 1/d_\theta$. We stress that the value $\mu = d_s/d_f$ is controlled solely by the connectivity index of F and is independent of the Hausdorff dimension d_f. Indeed, as follows from Eqn (2.7), the spectral dimension $d_s = 2d_f/(2+\theta)$ is proportional to the Hausdorff dimension d_f, and hence $\mu = 2/(2+\theta)$. From Eqn (2.4), the parameter μ is invariant under homeomorphisms $f: F \to F'$ and characterizes the topology of voids in F. Accordingly, expression (3.6) leads to the following important conclusion [42]. The behavior of transport processes on self-similar fractal sets is governed by topological invariants of these sets.

The topological invariance of sign θ (see Section 2) can be related to the existence of qualitative differences in the transport kinetics for positive and negative values of the connectivity index. A set F with $\theta > 0$ necessarily contains internal voids, and the particle spends an appreciable fraction of time to bypass them. 'Delays' typically occur because of multiple ('cyclic') excursions around the voids and because the particle can be trapped in internal 'dead-ends' (Fig. 5). Because $\theta > 0$ implies that the set F is path-connected by definition, all points of F are accessible to particles. By penetrating F deeper, the particle has a chance to be 'lost' in complex passages surrounding the internal voids and ultimately to return to the starting point. Such a trip gives no long-term contribution to the mean-square particle displacement $\langle \mathbf{r}^2(t) \rangle$. As a result, $\langle \mathbf{r}^2(t) \rangle$ grows more slowly than the dynamical time t, and hence the index μ is smaller than one, $\mu < 1$. Conversely, for $\theta < 0$, the propagation of particles over F is limited to the path-connected components, and hence the transport phenomena can only occur for asymptotically path-connected sets [70] with the Hausdorff dimension $d_f \geqslant 1$. (For $d_f < 1$, the set is disconnected everywhere and the notion of the mean-square displacement $\langle \mathbf{r}^2(t) \rangle$ loses its natural meaning.) Asymptotically path-connected fractals combine properties of path-connectedness and disconnectedness; they can be viewed as disconnected distributions of path-connected subsets. Because the Hausdorff dimension of each such subset cannot be smaller than one, the particles may freely migrate along F remaining within the limits of the 'their own' path-connected component (see Fig. 5). They are prohibited from leaving the chosen component because the entire fractal is disconnected, $\theta < 0$. The last condition restricts the possibilities for particles to 'wander' in space, and they have to move away from the original location in a more 'disciplined' way. At the microscopic level, the process looks like a ballistic rather than a diffusion one, and $\langle \mathbf{r}^2(t) \rangle$ then grows faster than time t, and therefore the exponent μ in (3.5) becomes greater than one, $\mu > 1$.

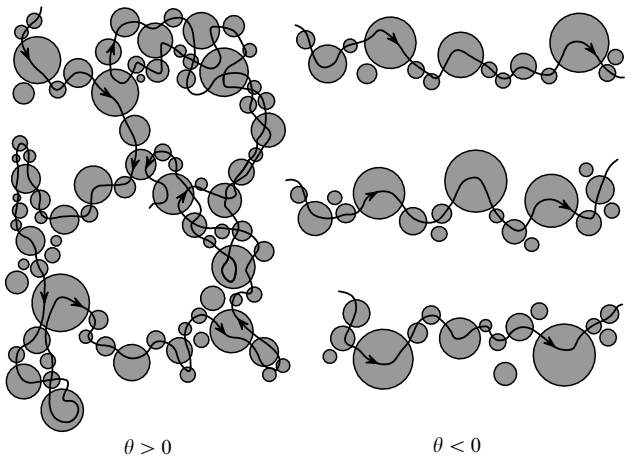

Figure 5. The behavior of transport processes in self-similar fractal structures for positive ($\theta > 0$) and negative ($\theta < 0$) values of the connectivity index.

Relation (3.5) describes a diversity of strange transport processes in nonlinear dynamical systems. In the narrow sense, the term 'strange transport' implies a nonlinear ($\mu \neq 1$) time dependence of the mean-square displacement of a point particle $\langle \mathbf{r}^2(t) \rangle$. In a broad sense, strange transport always emerges in considering non-Gaussian processes that allow correlation at arbitrarily large space–time scales. In particular, strange processes of type (3.5) have been discovered in laboratory plasma [63, 73, 74], in turbulent fluids above some critical Reynolds number $\mathcal{R}_*$ (~ 15) [75, 76], in magnetized vortical flows [77, 78], etc. Applications of strange processes to cosmic electrodynamics are used in studies of dynamical phenomena occurring in the solar photosphere [79], in the earth's dayside magnetopause [64], and in the earth's turbulent magnetotail [49]. Effects related to the finite correlation length for 'real' fractal structures were discussed in [64, 80].

3.2 Subdiffusion and superdiffusion

Putting the kinetics of nonequilibrium systems aside, we note that the theory of turbulence typically involves strange transport processes (3.5) with the index μ ranging from zero to two,

$$0 \leqslant \mu \leqslant 2\,. \tag{3.7}$$

If $0 \leqslant \mu < 1$, the transport processes are called subdiffusive, while for $1 < \mu \leqslant 2$, they are called superdiffusive. We also introduce the notion of a superballistic process corresponding to $\mu > 2$ [81]. Superballistic processes imply particle acceleration along the trajectories [81]. A number of physical realizations are considered in [82, 83]. The dynamics of acceleration is discussed in more detail in Section 8.

Along with the parameter μ, the exponent H related to μ as

$$\mu = 2H \tag{3.8}$$

is often used in the literature. In the context of fractal generalizations [9] of random Brownian motion [72], the quantity H is called the Hurst exponent. Under condition (3.7), we have

$$0 \leqslant H \leqslant 1\,. \tag{3.9}$$

It is easy to see that subdiffusive processes correspond to $0 \leqslant H < 1/2$ and superdiffusion ones to $1/2 < H \leqslant 1$. The value of H determines the fractal dimension of particle trajectories in the turbulent domain [59]:

$$d_w = \frac{1}{H} \qquad (d_w \geqslant 1)\,. \tag{3.10}$$

Combining Eqns (3.6), (3.8), and (3.10), we express the parameter d_w through the connectivity index of the fractal set F:

$$d_w = 2 + \theta\,. \tag{3.11}$$

Expression (3.11) establishes the dependence between the dynamical (d_w) and structural (θ) characteristics of transport processes in media with fractal geometry. Because dynamical trajectories are path-connected (here, we do not consider quantum mechanical effects where discontinuities along trajectories can occur), the value of d_w cannot be smaller than one. Thus, in the realm of classical physics, transport is possible only in sets with the connectivity index $\theta \geqslant -1$. Depending on the value of θ, the quantity $d_w = 2 + \theta$ can exceed the embedding space dimension ($n = 2$ for transport processes on a plane). The explanation is that the dynamical trajectory can have (multiple) self-intersection points, whose contribution to d_w is proportional to their multiplicities. For zero connectivity $\theta = 0$, the transport process becomes diffusive,

$$\left\langle \mathbf{r}^2(t) \right\rangle = 2\mathcal{D} \times t^1\,. \tag{3.12}$$

In this case, the mean-square particle displacement increases linearly with time. The parameters μ, H, and d_w are equal to

$$\mu = 1\,, \qquad H = \frac{1}{2}\,, \qquad d_w = 2\,. \tag{3.13}$$

The last equality shows that the capacity of diffusion trajectories is sufficient for covering the plane E^2 everywhere densely — a famous feature of the Peano curves! In the Euclidean space E^n, process (3.12) implies Gaussian increments $\delta\mathbf{r}(t)$ of $\mathbf{r}(t)$. The corresponding kinetic (diffusion) equation characterizing the evolution of the particle distribution function $\psi = \psi(t, \mathbf{r})$ is

$$\frac{\partial \psi}{\partial t} = \Delta_{\mathbf{r}}(\mathcal{B}\psi)\,, \tag{3.14}$$

where $\Delta_{\mathbf{r}} \equiv \partial^2/\partial \mathbf{r}^2$ is the Laplacian in E^n and $\mathcal{B} = \mathcal{D}/n$. We recall that the function $\psi(t, \mathbf{r})$ is defined as the probability density of finding a particle at point $\mathbf{r}$ at time t. The normalization condition

$$\int \psi(t, \mathbf{r})\, \mathrm{d}\mathbf{r} = 1 \tag{3.15}$$

is used in kinetic equation (3.14). Equations (3.13) and (3.14) describe the diffusion process as the Gaussian Brownian random walk in E^n [72].

3.3 Transport processes at the percolation threshold

We now consider a special case where the criticality of the fractal geometry of a set F is assumed in the context of the percolation transition. According to Eqn (2.10), the spectral dimension at the percolation threshold is $\mathcal{C} \approx 1.327\ldots$. From Eqn (3.6), we then find

$$\mu = 2H = \frac{\mathcal{C}}{d_{\mathrm{f}}}\,. \tag{3.16}$$

As is evident from Eqn (3.16), in order to calculate the exponent μ, it suffices to find the Hausdorff dimension d_{f} of the fractal set F on which transport processes are concentrated. Combining Eqns (2.15) and (3.16) yields restrictions on the parameter μ,

$$\frac{\mathcal{C}}{\mathcal{S}_n} \leqslant \mu \leqslant \mathcal{C}\,, \tag{3.17}$$

which are of an inherently topological nature. Correspondingly, for the exponent H, we have

$$\frac{\mathcal{C}}{2\mathcal{S}_n} \leqslant H \leqslant \frac{\mathcal{C}}{2}\,. \tag{3.18}$$

The embedding dimension n in Eqns (3.17) and (3.18) can vary from two to five. Thus, transport processes at the percolation threshold are subdiffusive ($\mathcal{C}/2\mathcal{S}_n \leqslant H < 1/2$) for $\mathcal{C} < d_{\mathrm{f}} \leqslant \mathcal{S}_n$ and superdiffusive ($1/2 < H \leqslant \mathcal{C}/2$) for $1 \leqslant d_{\mathrm{f}} < \mathcal{C}$. Interestingly, the upper limit for the exponent H, which is

$$H_{\max} = \frac{\mathcal{C}}{2} \approx 0.66\ldots \sim \frac{2}{3}\,, \tag{3.19}$$

is independent of the embedding dimension $2 \leqslant n \leqslant 5$. At $d_{\mathrm{f}} = \mathcal{C}$, we find from Eqn (3.16) that $H = 1/2$. Therefore, transport processes on a percolating fractal set F whose Hausdorff dimension is equal to the percolation constant $d_{\mathrm{f}}[F] = \mathcal{C}$ demonstrate diffusive behavior [84], namely $\langle \mathbf{r}^2(t) \rangle \sim t$. This result clarifies the physical interpretation of the parameter $\mathcal{C}$.

We emphasize that diffusion processes on percolating fractal structures are essentially non-Gaussian (in contrast to diffusion (3.14) in the Euclidean spaces E^n). Linear dependence (3.12) of the particle mean-square displacement on time is then a result of a complex 'interplay' of correlations operating at arbitrarily large spatial scales $r \to \infty$. Therefore, diffusion processes on F are strange in the broad sense. Equation (3.14) is inapplicable to strange (non-Gaussian) diffusion processes!

Consistently taking the correlations into account requires abandoning the Gaussian diffusion equation (3.14) and the traditional concept of transport process in a medium as the random Brownian motion of particles [85]. The required generalizations can be achieved using the methods of strange, or fractional, dynamics [86]. It is a powerful analytical tool that is adequate for complex nonlinear systems with multi-scale correlations in space and time. (The term 'strange kinetics' introduced in [86] is used in the literature along with the term 'fractional dynamics'.) Fractional differential equations used in 'strange' kinetics take the effects of memory, nonlocality, and intermittency into account; these effects go far beyond the conventional Gaussian statistics (3.14). Models of strange kinetic phenomena in turbulent media include Levy processes [85, 87] and fractal-time random walks (FTRW) [87 – 89], dating back to the a generalized (fractal) Brownian motion discovered by Mandelbrot and Van Ness [9, 90]. A phenomenological description of turbulent transport based on fractional

dynamics was obtained in [62, 91]. Difficulties emerging in deriving the corresponding kinetic equations from microscopic characteristics of the motion of individual particles were addressed in [92–95]. A thermodynamic justification of fractional dynamics is given in [96]. Multifractal generalizations were proposed in [97, 98]. Papers [47, 99] are devoted to a self-consistent analysis of strange kinetic processes near the NESS.

The mathematical formalism underlying fractional dynamics is in a certain sense equivalent to the method of the generalized master equation [92, 100]. This approach is extremely appealing because it does not break the analytic structure of the most important equations of mathematical physics. In particular, the solution of boundary value problems, the study of kinetic processes in an external field, and the calculation of the moments of the probability density function are quite similar to the standard mathematical algorithms.

We note in conclusion that the application of strange kinetics in modern theoretical and mathematical physics is by no means limited to the realm of turbulent diffusion. A great variety of phenomena matching the ideology of fractional calculus is considered in [92, 94, 101, 102]. In Section 11, we consider the fractional dynamic equation [43] describing fracton excitations in irregular systems. An analysis of the modulation instability of fracton modes with diffraction effects taken into account leads to a fractional generalization of the parabolic equation. Particular cases of this equation include the nonlinear fractional Schrödinger equation that allow solutions similar to envelope solitons in media with Euclidean geometry. The interest in fractons arises mainly in connection with the physics of high-temperature superconductors [103] and with superconductivity in complex molecular compounds, for example, in self-assembling organic polymers [43]. The spatial distribution of the order parameter corresponding to the superconducting phase in 'self-assembling' materials can be governed by an equation that is a fractional generalization of the Ginzburg–Landau equation known from the theory of phase transitions [104].

4. Fractional kinetic equation

4.1 Formulation of the equation

Following the general principles of strange kinetics [92, 93], we consider a fractional transport equation that generalizes Eqn (3.14) to dynamical systems with multi-scale correlations,

$$\frac{\partial^\alpha \psi}{\partial t^\alpha} = \nabla_{\mathbf{r}}^{2\beta}(\mathcal{B}\psi)\,. \tag{4.1}$$

To avoid unnecessary complications, the parameter $\mathcal{B}$ in Eqn (4.1) is considered coordinate-independent. Advection terms are omitted for simplicity. The radius vector $\mathbf{r}$ runs through the points lying on a percolating set F embedded into a Euclidean space E^n of dimension $n \geqslant 2$: $\{\mathbf{r}\} \sim F \subset E^n$. No external field is assumed in Eqn (4.1). Equation (4.1) is written in terms of the generalized (fractional) derivatives with respect to both time t, $\partial^\alpha/\partial t^\alpha$, and the real-space (or phase-space) variable $\mathbf{r}$, $\nabla_{\mathbf{r}}^{2\beta} \equiv \partial^{2\beta}/\partial \mathbf{r}^{2\beta}$. Introducing the fractional derivatives $\partial^\alpha/\partial t^\alpha$ and $\partial^{2\beta}/\partial \mathbf{r}^{2\beta}$ into kinetic equation (4.1) allows us to take the effects of memory (α) and nonlocality (β) into account within a unified mathematical formalism.

4.2 Fractional time derivative

The fractional time derivative in the right-hand side of Eqn (4.1) is expressed through the Riemann–Liouville operator [27]

$$\frac{\partial^\alpha}{\partial t^\alpha}\,\psi(t,\mathbf{r}) = \frac{1}{\Gamma(m-\alpha)}\,\frac{\partial^m}{\partial t^m}\int_0^t \frac{\mathrm{d}\vartheta}{(t-\vartheta)^{1+\alpha-m}}\,\psi(\vartheta,\mathbf{r})\,, \tag{4.2}$$

where $m-1 < \alpha \leqslant m$ for some integer m. (Below, we consider values of α ranging from zero to two.) The lower integration limit $t = 0$ in Eqn (4.2) determines the time instant t when dynamical phenomena in the medium are initialized; setting this time to zero is a matter of convention. By virtue of the Abel identity [105], fractional derivative (4.2) transforms into the standard 'integer' derivative $\partial\psi/\partial t$ as $\alpha \to 1$. In the static limit as $\alpha \to 0$, expression (4.2) yields $\partial^0\psi(t,\mathbf{r})/\partial t^0 \equiv \psi(t,\mathbf{r})$. For negative integer values $\alpha = -n$, the derivative $\partial^{-n}\psi(t,\mathbf{r})/\partial t^{-n}$ reproduces the n-fold repeated integral over the variable t. Putting strict formulations aside, we can say that $(-\alpha)$-fold fractional differentiation is equivalent to α-fold fractional integration. In a certain sense, the operations of fractional differentiation and fractional integration are inverse to each other. A systematic presentation of the fractional calculus can be found in monographs [100, 102, 106, 107].

Introducing the fractional derivative $\partial^\alpha/\partial t^\alpha$ in kinetic equation (4.1) allows us to take fractal-time random walks (FTRWs) into account; FTRW is the 'temporal component' of strange dynamical processes in turbulent media [92]. A distinctive feature of FTRWs is the absence of any noticeable jumps in particle behavior; here, the mean-square displacement $\langle \mathbf{r}^2(t)\rangle$ grows with time t as t^α. Equation (3.5) implies $\mu = \alpha$. The parameter α has the meaning of the fractal dimension of an 'active' time in which real walks of particles look like random processes; the active time interval is proportional to t^α.

Depending on the specific value of α, persistent (superdiffusive, $1 < \alpha \leqslant 2$) and antipersistent (subdiffusive, $0 \leqslant \alpha < 1$) processes are distinguished. For an antipersistent process, the active time forms a Cantor set ($0 \leqslant \alpha < 1$) with discontinuities at each point of the ray t. Each time the particle 'is stuck' in the turbulent field, a discontinuity emerges. The power-law distribution of the waiting time $\phi(\tau) \propto 1/\tau^{1+\alpha}$ between the subsequent displacements of particles in the configuration space $\{\mathbf{r}\}$ provides an example of the statistical model of an antipersistent process. On the other hand, persistent processes assume a more rapid movement ($1 < \alpha \leqslant 2$) of the active time compared to the real time t. The active time in the case of a persistent process can be 'laid' on a continuous self-affine curve 'overhanging' the ray t. The corresponding dynamical phenomena occur with an accelerated rate that does not allow particles to stay long in different 'interesting' points of the turbulent region. At present, the construction of an adequate probability theory justification of persistent processes is far from being complete. Following [9], we obtain the correlator

$$\mathcal{O}(t) \equiv -\frac{\langle \delta\mathbf{r}(-t)\,\delta\mathbf{r}(t)\rangle}{\langle \delta\mathbf{r}^2(t)\rangle} \tag{4.3}$$

of past and future increments of the radius vector $\mathbf{r}(t)$ during the fractal-time random walk:

$$\mathcal{O}(t) = 2^{\alpha-1} - 1 \equiv \mathrm{const}(t)\,. \tag{4.4}$$

As follows from Eqn (4.4), the correlation function $\mathcal{O}(t)$ takes a constant value (depending solely on the parameter α) at arbitrary (unlimitedly large) instants of time t. The property that the correlation function $\mathcal{O}(t)$ is constant is referred to as the persistency property [9], which is the conservation of tendencies in the behavior of a time series describing dynamical fluctuations of $\mathbf{r}(t)$. The persistency property assumes that correlations do not decouple at any time scales, i.e., rises and drops of the time series $\delta\mathbf{r}(t)$ are interrelated for all $-\infty \leqslant t \leqslant +\infty$.

Persistent (antipersistent) fractal-time processes have a positive (negative) correlation function $\mathcal{O}(t)$ and correspond to superdiffusion (subdiffusion) transport processes in a turbulent region, respectively. For $\alpha \neq 1$, FTRWs are essentially non-Markovian (because in this case, $\mathcal{O}(t) \neq 0$ for any time interval t). Non-Markovianness (i.e., the system memory of its past [72]) is expressed through the presence of the nonlocal kernel $(t-\vartheta)^{-(1+\alpha-m)}$ in Riemann – Liouville operator (4.2). In the Markovian limit $\alpha \to 1$, we have $\mathcal{O}(t) \equiv 0$ [there are no correlations between past and future increments of $\mathbf{r}(t)$]; integro-differential operator (4.2) is then the integer (local with respect to time) derivative $\partial/\partial t$.

4.3 Fractional real-space derivative

We now turn to the 'spatial counterpart' of strange transport processes corresponding to the operation $\nabla_{\mathbf{r}}^{2\beta}$ in kinetic equation (4.1). Without losing the generality, we assume the parameter 2β to vary from one to two. We decompose $\mathbf{r}$ over a Cartesian coordinate basis x_i in E^n. We have $\mathbf{r} = \mathbf{e}^i x_i$, where $\mathbf{e}^i$ is the unit vector in the direction $i = 1, \ldots, n$. (Summation over repeated indices is assumed.) The fractional derivative $\partial^\beta/\partial x_i^\beta$ of the order β is the integro-differential operator defined as

$$\frac{\partial^\beta}{\partial x_i^\beta}\,\psi(t,\mathbf{r}) = \frac{1}{\Gamma(1-\beta)}\,\frac{\partial}{\partial x_i}\int_{-\infty}^{x_i}\frac{\mathrm{d}x_i'}{(x_i - x_i')^\beta}\,\psi(t,\mathbf{r}')\,. \quad (4.5)$$

In contrast to Eqn (4.2), the integration in Eqn (4.5) starts not from zero but from minus infinity. This 'normalization' is due to the assumption that the set $F \subset E^n$ is percolating, i.e., contains arbitrarily large spatial scales. Integro-differential operator (4.5) with an infinite lower limit is often called the Riesz – Weyl operator [92]. Like the Riemann – Liouville operator, the Riesz – Weyl operator correctly reproduces the notion of integer derivative with respect to x_i as $\beta \to 1$. However the improper integration in Eqn (4.5) significantly 'improves' analytic properties of the Riesz – Weyl operator due to the vanishing of the corresponding substitutions at the lower limit [94]. Treating $\partial^\beta/\partial x_i^\beta$ as components of the vector $\partial^\beta/\partial\mathbf{r}^\beta$, we obtain a natural generalization of the gradient: $\nabla_{\mathbf{r}}^\beta \equiv \partial^\beta/\partial\mathbf{r}^\beta \equiv \mathbf{e}^i\partial^\beta/\partial x_i^\beta$. The operation $\nabla_{\mathbf{r}}^{2\beta}$ is defined as a scalar product $\nabla_{\mathbf{r}}^\beta\nabla_{\mathbf{r}}^\beta$ in the bases $\{\mathbf{e}^i\}$. In formal representation, $\nabla_{\mathbf{r}}^{2\beta} \equiv \partial^{2\beta}/\partial\mathbf{r}^{2\beta} \equiv \delta^{ik}\partial^{2\beta}/\partial x_i^\beta\partial x_k^\beta$, where the Kronecker symbol $\delta^{ik} \equiv \mathbf{e}^i\mathbf{e}^k$ represents the metric tensor components in the Cartesian basis. The scalar product of fractional differentiation operators $\nabla_{\mathbf{r}}^{2\beta} \equiv \nabla_{\mathbf{r}}^\beta\nabla_{\mathbf{r}}^\beta$ can be treated as a generalized Laplacian. As $\beta \to 1$, we have $\Delta_{\mathbf{r}} \equiv \nabla_{\mathbf{r}}^2$. We note that definition (4.5) remains meaningful for all $0 \leqslant \beta < 1$. The constraint $1 \leqslant 2\beta < 2$ is imposed in order for the scalar product $\nabla_{\mathbf{r}}^\beta\nabla_{\mathbf{r}}^\beta$ to have a simpler analytic structure. The generalization to the case $0 \leqslant 2\beta < 1$ is straightforward, but we do not discuss it in the context of Eqn (4.1). The transport equation involving the fractional Laplacian $\Delta_{\mathbf{r}}^{1/3}$ was first studied by Monin [108, 109] in the framework of the Kolmogorov theory K41: $2\beta = 2/3$.

The fractional Riesz – Weyl operator corresponds to Levy processes in the real space $\{\mathbf{r}\}$. Levy processes are Markovian, they do not keep track of their history, but they are nonlocal, i.e., they interpret entire regions of the phase space simply as points. The particle dynamics in such regions looks like instant jumps — the 'Levy flights' — from one point to another. The jumps correspond to the singular kernel $(x_i - x_i')^{-\beta}$ in the integrand Eqn (4.5). In the Levy statistics, the lengths ℓ of the jumps are power-law distributed, $\phi(\ell) \propto 1/\ell^{1+2\beta}$ [92[. For comparison, fractal-time random walks assume an exponentially rapid decay of probability $\phi(\ell) \propto \exp(-\ell^2)$, which ensures FTRW continuity with respect to $\mathbf{r}$. The Levy processes thus assume appreciable jumps with much larger probability than FTRWs. A consequence of such behavior is an unpleasant divergence of the mean-square particle displacement in the Levy statistics [92]: $\langle\mathbf{r}^2(t)\rangle \to \infty$.

Clearly, real particles with finite mass cannot instantly fly from one point of space to another. Therefore, the Levy statistics should be considered as a convenient model describing rapid coherent transport phenomena in turbulent media, for example, convection of particles together with the cyclone capturing them. The mean-square displacement divergence in the Levy processes can be eliminated by imposing certain space – time constraints that force particles to move 'more quietly' in space [92]. Constrained Levy processes are usually called Levy walks. The fractional kinetic equation for Levy walks was obtained in [110] by requiring particles to move with a restricted velocity. An alternative approach is based on integrating kinetic equations for free Levy processes in an imaginary nonstationary domain expanding with time [111]. The divergence problem can also be bypassed by using a fractional normalization condition that redefines the total probability in the Levy statistics [70]. This condition must be made consistent with the fractal geometry of the set F.

4.4 Fractional normalization condition and the radial part of the generalized Laplacian

In fact, we restrict the Laplacian $\nabla_{\mathbf{r}}^{2\beta} \equiv \partial^{2\beta}/\partial\mathbf{r}^{2\beta}$ to an d_s-dimensional fractal subset $F \subseteq E^n$ of a Euclidean space E^n. The self-consistent normalization of the function $\psi(t,\mathbf{r})$ can be chosen as

$$\int_F \psi(t,\mathbf{r})\,\mathrm{d}\mathbf{r}^\beta = 1. \quad (4.6)$$

Condition (4.6) regulates Levy flights (β) in the 'fractal sky' of the fractal set F (due to $\int_F$). Next, we consider the fractional integration operator $\int\mathrm{d}\mathbf{r}^\beta \equiv \partial^{-\beta}/\partial\mathbf{r}^{-\beta}$ as the inverse to the differentiation operator $\nabla_{\mathbf{r}}^\beta \equiv \partial^\beta/\partial\mathbf{r}^\beta$. The mutually inverse relation of the operators $\int\mathrm{d}\mathbf{r}^\beta$ and $\nabla_{\mathbf{r}}^\beta$ is expressed by the identity

$$\nabla_{\mathbf{r}}^\beta\int_{F_{\mathbf{r}}}\varphi(t,\mathbf{r})\,\mathrm{d}\mathbf{r}^\beta \equiv \varphi(t,\mathbf{r}) \quad (4.7)$$

for any internal domain $F_{\mathbf{r}} \subseteq F$ of radius $\mathbf{r}$ in F and an arbitrary β-integrable function $\varphi(t,\mathbf{r})$. The mean-square particle displacement $\langle\mathbf{r}^2(t)\rangle$ is

$$\langle\mathbf{r}^2(t)\rangle \equiv \int_F \mathbf{r}^2\psi(t,\mathbf{r})\,\mathrm{d}\mathbf{r}^\beta\,. \quad (4.8)$$

In d_s dimensions, the radial part of the Riesz–Weyl operator can be represented as

$$\nabla_r^{2\beta} = \frac{1}{r^{d_s-1}} \frac{\partial^\beta}{\partial r^\beta} \left(r^{d_s-1} \frac{\partial^\beta}{\partial r^\beta} \right), \tag{4.9}$$

where the radial derivative $\partial^\beta/\partial r^\beta$ must be defined (in accordance with the meaning of $r \geqslant 0$) through the fractional Riemann–Liouville operator

$$\frac{\partial^\beta}{\partial r^\beta} \psi(t,r) = \frac{1}{\Gamma(1-\beta)} \frac{\partial}{\partial r} \int_0^r \frac{dr'}{(r-r')^\beta} \psi(t,r') . \tag{4.10}$$

Equation (4.10) is quite similar to Eqn (4.2). Equations (4.9) and (4.10) reproduce the radial part

$$\Delta_r = \frac{1}{r^{n-1}} \frac{\partial}{\partial r} \left(r^{n-1} \frac{\partial}{\partial r} \right) \tag{4.11}$$

of the standard Laplacian $\Delta_{\mathbf{r}} \equiv \partial^2/\partial \mathbf{r}^2$ in the limit as $\beta \to 1$ and $d_s \to n$. Expressions (4.1) and (4.2) together with Eqns (4.9) and (4.10) represent the fractional kinetic equation for strange transport processes in a percolating set F in the full integro-differential form. We emphasize that in this case, we are interested in isotropic processes on self-similar fractal structures; the angular part [98] of the Riesz–Weyl operator is not discussed. For isotropic processes, integration over $\mathbf{r}$ in Eqns (4.6)–(4.8) reduces to integration over the radial variable $r \equiv |\mathbf{r}|$, $r^2 \equiv \mathbf{r}^2$, in accordance with

$$d\mathbf{r}^\beta \equiv \Omega_{d_s} r^{d_s-1} dr^\beta , \tag{4.12}$$

where the solid angle Ω_{d_s} is defined by formula (2.14).

4.5 Mean-square particle displacement

A general solution of fractional kinetic equation (4.1) for arbitrary initial conditions can be expressed through the Fox function [100]. But the dependence of the mean-square particle displacement $\langle r^2(t) \rangle$ on time t can also be evaluated without applying such a sophisticated formalism. We first multiply both parts of fractional kinetic equation (4.1) by $r^{2\beta}$, where $1 \leqslant 2\beta < 2$ takes Levy processes into account. We then apply the fractional integration operator $\int d\mathbf{r}^\beta \equiv \partial^{-\beta}/\partial \mathbf{r}^{-\beta}$ satisfying identity (4.7). The integration is performed over the entire volume of the percolating set F with representation (4.12) taken into account; correspondingly, the radial scale r changes from zero to infinity, $0 \leqslant r \leqslant \infty$. We pull the differentiation with respect to time from the integrand on the left-hand side of Eqn (4.1) and replace the partial derivative $\partial^\alpha/\partial t^\alpha$ with the total fractional derivative d^α/dt^α. The remaining fractional integral over r is the ensemble average $\langle r^{2\beta}(t) \rangle$. At long times $t \to \infty$, we have $\langle r^{2\beta}(t) \rangle \sim \langle r^2(t) \rangle^\beta$, where $\langle r^2(t) \rangle$ is defined by expression (4.8). On the right-hand side of Eqn (4.1), performing the fractional integration by parts twice and recalling normalization condition (4.6), we obtain the constant $\Lambda\mathcal{B}$, where

$$\Lambda = \frac{\Gamma(1+2\beta)}{\Gamma(1+\beta)} \frac{\Gamma(d_s+\beta)}{\Gamma(d_s)} . \tag{4.13}$$

Therefore,

$$\frac{d^\alpha}{dt^\alpha} \langle r^2(t) \rangle^\beta = \Lambda\mathcal{B} . \tag{4.14}$$

From differential equation (4.14), we find

$$\langle r^2(t) \rangle = \left[\frac{\Lambda\mathcal{B}}{\Gamma(1+\alpha)} \right]^{1/\beta} \times t^\mu \quad (t \to \infty) , \tag{4.15}$$

where

$$\mu = \frac{\alpha}{\beta} . \tag{4.16}$$

The convergence of the mean-square displacement given by (4.8) and (4.15) is provided by fractional normalization condition (4.6) containing the nonlocal integration operator $\int d\mathbf{r}^\beta \equiv \partial^{-\beta}/\partial \mathbf{r}^{-\beta}$. Setting

$$\frac{\Lambda\mathcal{B}}{\Gamma(1+\alpha)} \equiv (2\mathcal{D})^\beta \tag{4.17}$$

in Eqn (4.15), we recover dependence (3.5) for strange transport processes near the NESS. Expression (4.17) relates the parameters $\mathcal{D}$ and $\mathcal{B}$ for arbitrary values of the exponents $0 \leqslant \alpha \leqslant 2$ and $1 \leqslant 2\beta < 2$. In the Gaussian limit $\alpha \to 1$, $\beta \to 1$, $d_s \to n$, Eqn (4.17) straightforwardly implies that $\mathcal{B} \to \mathcal{D}/n$, in agreement with Eqn (3.14).

Expression (4.16) implies that the exponent μ for strange transport processes is determined by competition between FTRWs (α) and Levy processes (β). Correspondingly, Eqn (3.6) yields the 'proportionality relation' for kinetic equation (4.1):

$$\frac{\alpha}{\beta} = \frac{d_s}{d_f} \equiv \frac{2}{2+\theta} . \tag{4.18}$$

In the critical regime ($d_s = \mathcal{C}$), with Eqn (2.10) taken into account, we have

$$\frac{\alpha}{\beta} = \frac{\mathcal{C}}{d_f} . \tag{4.19}$$

Recalling Eqn (3.8), we arrive at the proportionality relation written for the exponent H:

$$H = \frac{\alpha}{2\beta} = \frac{\mathcal{C}}{2d_f} . \tag{4.20}$$

Equations (4.19) and (4.20) relate the indices (α, β) in fractional kinetic equation (4.1) to the Hausdorff dimension d_f of the fractal set F at the percolation threshold. For $\alpha = \beta$, we arrive at a diffusion process: $H = 1/2$. If $\alpha = \beta \neq 1$, the diffusion is strange in the broad sense (see Section 3). The values $\alpha = \beta = 1$ correspond to the Gaussian (nonstrange) diffusion. In the last case, all derivatives in kinetic equation (4.1) are integers. We stress that the condition $\alpha = \beta$ itself guarantees only a linear increase of the mean-square particle displacement with time, but by no means the Gaussian character of the transport processes [84]. To pass to the Gaussian limit, stronger conditions $d_f \to d_s \to n$ must be satisfied.

At the macroscopic level, the 'opposition' of fractal time random walks (α) and Levy flights (β) leads to an extremely complicated space–time structure of motion of individual particles, which sporadically prefer one process to the other. For $\alpha < 1$, particles either 'mark time' (FTRW) or demonstrate bursts of 'activity' by rapidly leaking through the turbulent region (Levy). This type of motion is called

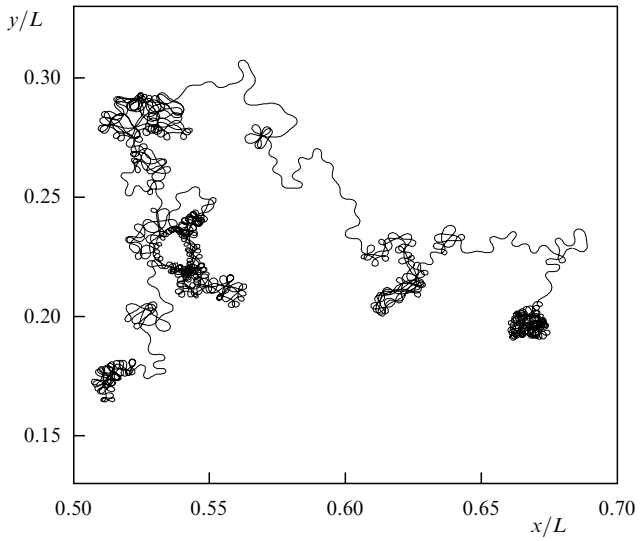

Figure 6. The trajectory of a charged particle (ion) near the separatrice of a fractal Brownian surface simulating a multi-scale perturbation of a constant homogeneous magnetic field. The trajectory is obtained by numerical integration of microscopic equations of motion by the fifth-order Runge – Kutta method. The factor determining the particle behavior is the phase break of the Larmor rotation under the action of the perturbation. (Courtesy of G Zimbardo, University of Calabria, Italy.)

intermittent; its onset is facilitated by chaotic transitions between the competing regimes. Figure 6 illustrates the trajectory of a charged particle near the separatrice of the fractal Brownian surface simulating perturbation of a homogeneous magnetic field directed perpendicularly to the xy plane [64]. We draw attention to the irregular character of the dynamical process balancing between periods of a long 'stagnation' (balls of 'entangled' trajectories) and rapid 'passages' of particles across the field (disentangled 'filaments').

5. The phenomenon of self-organized criticality

The relation between topology and kinetics is provided by the concept of the nonequilibrium (quasi)-stationary state (NESS) of a turbulent system. Transition to the NESS occurs due to multi-scale space and time correlations under the necessary condition of exchange of energy and entropy with the external medium. Spatial correlations are manifested by remarkable structural characteristics of the NESS whose topology is that of a percolating (infinitely path-connected) fractal set lying 'at the percolation threshold' (i.e., at a critical point below which kinetic processes in the medium are restricted to a finite domain of the phase space). The critical regimes are 'preferred' because they are relatively favorable thermodynamically: the free energy of a turbulent ensemble decreases when threshold distributions corresponding to the percolation transition in the system are formed. The universal percolation constant $\mathcal{C} \approx 1.327\ldots$ introduced in Section 2 is related to the existence of the threshold. This constant determines (in accordance with its physical meaning) the minimal fractional number of the degrees of freedom that a particle must have in order to pass through the turbulence region in the course of random scatterings on the field clots.

In contrast to spatial correlations, time correlations tend to 'revive' the fractal geometry of the system rather than to stabilize the turbulent ensemble near the NESS, by allowing the system to 'stir' within the limitations of the percolation geometry'. In no respect being inferior to their space cousins, who inherited the percolation constant $\mathcal{C} \approx 1.327\ldots$ from the universal value theorem, time correlations seize their own universality 'feuds' in the opulent realm of strong turbulence. The tendency to self-organized criticality (SOC) is one such feud. It is a singular nonequilibrium (quasi)-stationary state [112, 113], reaching which requires all external (forcing) actions on the system to be as slow as possible [114, 115]. At slow forcing, the system acquires a certain 'organization freedom', and the tendency to SOC becomes a universal phenomenon independent of system specifics. The self-organized criticality concept determines the preferential state of a dynamic system far from the thermal equilibrium, which has certain 'advantages' compared to 'nonsingular' NESS's. The most important physical applications are discussed in monographs [28, 116, 117]. We also note original papers [84, 118 – 124].

The universal character of SOC can be understood in the context of fundamental physical principles (such as the minimum-action principle) governing the most general behavior of dynamical systems [70]. Indeed, the 'preferences' given to one or another NESS can be expressed through some functional that has the meaning of an action for the NESS as a whole. As the corresponding 'generalized coordinate', it is convenient to take a parameter 'distinguishing' different NESS's by their characteristic statistical signatures. The problem is to obtain SOC from the minimum-action principle in the 'nonequilibrium stationary state space'. This approach can be considered a realization of the minimum-action principle in application to NESS. Under an infinitely slow external forcing, a self-consistent dynamical system chooses the state with the minimal action among all possible NESS's. We pass to the quantitative description of the problem.

5.1 Restriction on the Kubo number

We assume that the NESS geometry is a fractal F embedded into a Euclidean space E^n of dimension $n \geqslant 2$. The fractal set F can be 'visualized' by taking a snapshot of the NESS with a short exposure time $t = \tau$. With increasing τ, the pictures become more and more smeared due to the internal NESS dynamics. For an external observer, the set F appears to slowly 'stir', i.e., to change its location in the space E^n as a result of continuous 'self-pouring' (Fig. 7). The Hausdorff dimension $d_f = d_f[F]$ and the connectivity index $\theta = \theta[F]$ are then conserved in time. Generally, the 'self-pouring' can be treated as a set of (nonlinear) long-wavelength excitations on F; in the absence of excitations, the set F 'freezes' (stops 'stirring').

We assume that the picture of the NESS is fully smeared at exposures exceeding some characteristic time τ_*:

$$\tau \gtrsim \tau_* . \tag{5.1}$$

The existence of a finite time τ_* is the most important (and unique) assumption about the internal NESS dynamics that we make in the present review. This assumption allows us to say that in the (long) time (5.1), the branches of the fractal set F touch all or almost all points of the embedding space E^n. In other words, there are no forbidden areas in E^n that 'do not participate in the life' of the NESS (see Fig. 7). By the order of magnitude,

$$\tau_* \sim \frac{\xi}{V} , \tag{5.2}$$

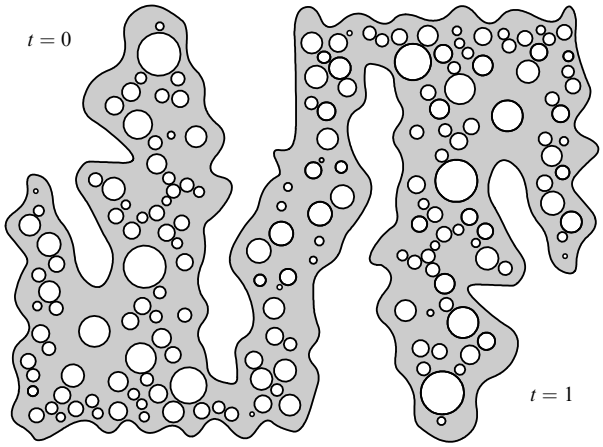

Figure 7. 'Self-pouring' of a fractal set due to inherent dynamical nonlinear degrees of freedom.

where ξ is the minimal excitation wavelength and the parameter V determines the group velocity of 'self-pouring'. The group velocity V must be small compared to the velocities of particles percolating through the turbulent domain,

$$V \ll w\,. \tag{5.3}$$

Condition (5.3) means that (strange) transport processes near the NESS have enough time to 'adjust' to the inherent dynamics of the fractal set F: the consistency of transport processes with the NESS fractal geometry ensures the conservation of the parameters $d_{\rm f}[F]$ and $d_{\rm f}[F]$ in time. From conditions (5.2) and (5.3), we find

$$\mathcal{Q}_* \equiv \frac{w\tau_*}{\xi} \gg 1\,. \tag{5.4}$$

The parameter $\mathcal{Q}_*$ is usually called the Kubo number. Expressions (5.1) and (5.4) can be conveniently rewritten through the characteristic frequencies $f \sim 1/t$:

$$f \lesssim f_* \sim \frac{V}{\xi}\,, \tag{5.5}$$

$$\mathcal{Q}_* \equiv \frac{w}{\xi f_*} \gg 1\,. \tag{5.6}$$

Relations (5.1), (5.5) and (5.4), (5.6) indicate that the inherent NESS dynamics is a slow process compared to the particle walk over the set F, which is responsible for the mass and charge transfer in the turbulent domain. The criterion of slowness is a large value of the Kubo number, $\mathcal{Q}_* \gg 1$. We stress that range (5.5) is given in the NESS reference frame. If the turbulent ensemble moves with a velocity u relative to the observer, the Doppler correction must be taken into account in Eqn (5.5.):

$$f \lesssim f_* \sim \frac{|V-u|}{\xi}\,. \tag{5.7}$$

We return to expression (5.7) when we consider fluctuation spectra in the solar wind and the earth's magnetotail.

5.2 Statistics of dynamical fluctuations

Under conditions (5.1), (5.5) and (5.4), (5.6), the internal NESS dynamics can be written in the form of a self-affine time series $\mathcal{I}_S(t)$, $t \gg \tau_*$, whose Hausdorff dimension

$$\delta_{\rm f} \equiv d_{\rm f}[\mathcal{I}_S] = 1 + S \quad (1 \leqslant \delta_{\rm f} \leqslant 2) \tag{5.8}$$

is independent of the location in the space E^n. The observer in the NESS reference frame interprets the series $\mathcal{I}_S(t)$ as dynamical fluctuations in the turbulent medium due to the internal NESS variability. Expression (5.8) follows from Eqn (2.2). The Hausdorff dimension $\delta_{\rm f}$ determines the topological entropy $\Xi_{\rm f}$ of the curve $\mathcal{I}_S(t)$ according to [27]:

$$\Xi_{\rm f}[\mathcal{I}_S] = 1 - \frac{1}{\delta_{\rm f}}\,. \tag{5.9}$$

The topological entropy $0 \leqslant \Xi_{\rm f} \leqslant 1/2$ characterizes the degree of 'crumpling' of the series $\mathcal{I}_S(t)$. For smooth curves ($S = 0$, $\delta_{\rm f} = 1$), the entropy $\Xi_{\rm f}[\mathcal{I}_0] = 0$.

For self-affine time series $\mathcal{I}_S(t)$, the dispersion of increments at any time t is given by [9]

$$\left\langle \left|\mathcal{I}_S(t+\Delta t) - \mathcal{I}_S(t)\right|^2 \right\rangle = \Lambda_J \times |\,\Delta t\,|^{2J}\,, \tag{5.10}$$

where Λ_J is the normalization constant, the averaging operation $\langle \ldots \rangle$ is defined as

$$\langle \ldots \rangle \equiv \frac{1}{t}\int_0^t [\ldots]\,{\rm d}t\,, \tag{5.11}$$

and the parameter J is related to S and $\delta_{\rm f}$ by

$$J = 1 - S = 2 - \delta_{\rm f} \quad (0 \leqslant J \leqslant 1)\,. \tag{5.12}$$

For $J = S = 1/2$, variance (5.10) corresponds to random fluctuations in the system,

$$\left\langle \left|\mathcal{I}_{1/2}(t+\Delta t) - \mathcal{I}_{1/2}(t)\right|^2 \right\rangle = \Lambda_{1/2} \times |\,\Delta t\,|\,, \tag{5.13}$$

with the Gaussian probability distribution. We note that the Gaussian property follows from Eqn (5.13) because at large $t \gtrsim \tau_*$, fluctuations fill the entire embedding Euclidean space E^n. [The situation is quite analogous to process (3.12) in E^n.] The Hausdorff dimension $\delta_{\rm f}$ for the Gaussian time series $\mathcal{I}_{1/2}(t)$ is $\delta_{\rm f} = 2 - 1/2 = 3/2$ [36].

By contrast, for $J = 1 - S \neq 1/2$, the statistics of dynamical fluctuations is essentially non-Gaussian: 'outbursts' and 'drops' in the curve $\mathcal{I}_S(t)$ occur not randomly, as in Gaussian limit (5.13), but in accordance with certain tendencies [9] controlled by the value of the parameter $J = 1 - S$. Indeed, we consider the correlator $\mathcal{O}_J(t)$ of the past and future increments of a self-affine time series $\mathcal{I}_S(t)$ [9]:

$$\mathcal{O}_J(t) = -\frac{\left\langle \mathcal{I}_S(-t)\mathcal{I}_S(t)\right\rangle}{\left\langle \mathcal{I}_S^2(t)\right\rangle}\,. \tag{5.14}$$

Setting $\mathcal{I}_S(0) = 0$, we obtain from Eqn (5.14) that

$$\mathcal{O}_J(t) = 2^{2J-1} - 1 = {\rm const}(t)\,. \tag{5.15}$$

We have already dealt with correlators like (5.15) in describing FTRWs. The parameter $2J$ in Eqn (5.15) is analogous to the active-time fractal dimension α in Eqn (4.4). As can be seen from Eqn (5.15), the value $0 \leqslant J \leqslant 1$ determines the statistics of fluctuations related to the internal 'life' of NESS's. For Gaussian fluctuations ($J = 1/2$), the

correlator $\mathcal{O}_J(t) \equiv 0$ for all $t \gtrsim \tau_*$ — outbursts and drops of the series $\mathcal{I}_S(t)$ are absolutely random. For $0 \leqslant J < 1/2$, the correlator $\mathcal{O}_J(t) < 0$ — an 'outburst' in the past rather means a drop soon in the future. Conversely, for $\mathcal{I}_S(t)$, the correlator $1/2 < J \leqslant 1$ — an outburst in the past means an increase in the future. We note that the correlator $\mathcal{O}_J(t)$ takes a constant (time-independent) value (5.15) for all $t \gtrsim \tau_*$. This feature allows us to speak of the conservation of tendencies in the behavior of the series $\mathcal{I}_S(t)$, also known as persistency [9]. For $1/2 < J \leqslant 1$, we speak of persistent time series $\mathcal{I}_S(t)$ and for $0 \leqslant J < 1/2$, of antipersistent.

5.3 Self-affine series spectra

We consider the Fourier transformation

$$P[\mathcal{I}_S](f) = \frac{1}{2\pi}\int_{-\infty}^{+\infty} |\mathcal{I}_S(t)|^2 \exp(\mathrm{i}ft)\,\mathrm{d}t \tag{5.16}$$

of a statistically self-affine time series $\mathcal{I}_S(t)$. Because the series $\mathcal{I}_S(t)$ is similar to $\mathcal{I}_S(ft)$ with the coefficient f^{S-1}, the power spectrum f in Eqn (5.16) has a power-law dependence on frequency,

$$P[\mathcal{I}_S](f) \sim f^{-\varpi} \tag{5.17}$$

with the exponent

$$\varpi = 3 - 2S = 2J + 1\,. \tag{5.18}$$

The frequency f in Eqn (5.17) satisfies condition (5.5). Because $0 \leqslant J \leqslant 1$, the value of ϖ changes within the limits

$$1 \leqslant \varpi \leqslant 3\,. \tag{5.19}$$

In particular, for the Gaussian time series $\mathcal{I}_{1/2}(t)$, the power-law exponent ϖ is equal to two. We note that the spectrum $P[\mathcal{I}_{1/2}] \sim f^{-2}$ (reflecting the Gaussian Brownian motion of particles in E^n) is sometimes called the brown noise [28]. Combining Eqns (5.12) and (5.18), we arrive at the Berry formula [125]

$$\varpi = 5 - 2\delta_\mathrm{f}\,. \tag{5.20}$$

Equations (5.18) and (5.20) have been directly applied in studies of fractal time series $\mathcal{I}_S(t)$ describing dynamical fluctuations in solar wind [54, 68, 69], the terrestrial magnetotail [47, 51, 126], and the active regions of the solar photosphere [117]. General statistical methods pertaining to the fractal analysis of signals can be found in monographs [9, 127].

5.4 Action for dynamical fluctuations

We now define the action for dynamical fluctuations (5.10), (5.11) as

$$\mathcal{A}_J = -\frac{1}{4\pi}\int \mathrm{d}\mathbf{r}\int_0^t \left\langle \mathcal{I}_S(-t)\,\mathcal{I}_S(t)\right\rangle \mathrm{d}t\,, \tag{5.21}$$

where $t \gg \tau_*$. The variance $\left\langle \mathcal{I}_S^2(t)\right\rangle/8\pi$ characterizing the behavior of the integrand (the 'Lagrangian density') by means of correlator (5.14) is the energy density of fluctuations in E^n. The parameter $J = 1 - S$ has the meaning of a generalized coordinate fixing the system position in the functional space of nonequilibrium (quasi)-stationary states. All possible NESS's with different indices J, $0 \leqslant J \leqslant 1$, are elements of this space. We note that terms with generalized momenta $\partial J/\partial t$ are omitted in Eqn (5.21). This is related to the assumed slowness of external forcing perturbations that govern the location of the turbulent ensemble in the interval $0 \leqslant J \leqslant 1$. We also note that the integrand in Eqn (5.21) is invariant under time reversal $t \to -t$. The symmetry $t \to -t$ is related to the absence of large-scale evolutionary phenomena in the system near the NESS. From Eqns (5.10), (5.11), (5.15), and (5.21), we derive

$$\mathcal{A}_J = \frac{1}{4\pi}\int \mathrm{d}\mathbf{r}\left(\frac{2^{2J-1}-1}{2J+1}\right)\Lambda_J \times t^{2J+1}\,. \tag{5.22}$$

Action (5.22) increases with time t as t^{2J+1}. For any given $t \gg \tau_*$, action (5.22) is minimal in the limit

$$J \to 0\,. \tag{5.23}$$

Under condition (5.23), variance (5.10) is independent of the time interval Δt. The value of the parameter S that follows from Eqn (5.23) is

$$S \to 1\,. \tag{5.24}$$

Correspondingly, the Hausdorff dimension δ_f of the time series $\mathcal{I}_S(t)$ tends to its minimal value

$$\delta_\mathrm{f} = 1 + S \to 2\,. \tag{5.25}$$

The topological entropy $\Xi_\mathrm{f}[\mathcal{I}_S]$ is maximal in the limit as (5.25),

$$\Xi_\mathrm{f}[\mathcal{I}_S] \to \frac{1}{2}\,. \tag{5.26}$$

Under condition (5.26), the time series $\mathcal{I}_S(t)$ reveals the most complete 'collection' of irregularities that a continuous (!) self-affine curve on the plane can have. According to Eqns (5.17) and (5.18), the Fourier spectrum of such a curve is given by

$$P[\mathcal{I}_S](f) \sim f^{-1}\,, \tag{5.27}$$

which corresponds to the lower limit

$$\varpi \to 1 \tag{5.28}$$

of the exponent $1 \leqslant \varpi \leqslant 3$. Spectrum (5.27) is usually called the rose noise or the flicker noise [28]. The ubiquity of the rose noise [28] inspired Bak, Tang, and Wiesenfeld [112, 113] to introduce the concept of SOC, which explains the tendency of complex dynamical systems [116] toward singular regime (5.27) at low frequencies. The limit in Eqn (5.23) leads to a deep understanding of SOC as a nonequilibrium (quasi)-stationary state subjected to the minimum-action principle stated in (5.21) and (5.22). We have thus established the correspondence of the SOC concept to the fundamental physical principles underlying the modern theory of dynamical systems. Frequency restrictions follow from conditions (5.5) and (5.6).

5.5 The sand-pile model

Classical SOC models [116] are based on the notion of a sand pile whose slope (produced by pouring the sand) is formed by

releasing the excess mass in avalanches. By rotational symmetry, the process looks the same in any vertical cross section of the hill passing through its top. If we lived in a two-dimensional world, then by pouring two-dimensional sand hills we would obtain all the useful information on SOC kinetics. The avalanche trajectories in such a world look like one-dimensional structures covering the hill from the outside. The sand hill model can be considered an alternative to the dynamical model based on the statistics of the self-affine time series $\mathcal{I}_S(t)$. One-dimensional long-wavelength excitations in this case serve as analogs of avalanches. These excitations modulate the fractal distribution F at large scales. Long-wave tearing modes in turbulent current sheets [49] provide an example.

An important point is that the statistics of dynamical fluctuations $\mathcal{I}_S(t)$ directly mirrors the system organization in the configuration space; in particular, the fractal dimension δ_f determining the Fourier spectrum of the series $\mathcal{I}_S(t)$ is related to the Hausdorff dimension characterizing the capacity of turbulent structures in E^n. At scales smaller than the excitation length in the system, the Hausdorff dimension d_f is determined by the specifics of interactions involved in the NESS formation. With increasing scale, the modulation effects (i.e., energy drops to the avalanches) lead to the situation where d_f 'forgets' specific properties of the turbulent ensemble and takes the universal limiting value [49]

$$d_f \to 1\,. \tag{5.29}$$

Transition (5.29) should be considered a spatial variant of condition (5.25). Expressions (5.25) and (5.29) establish the correspondence between the sand-pile model ($d_f \to 1$) and the dynamical SOC model ($\delta_f \to 2$). Moreover, a general relation between the parameters d_f and δ_f can be found that goes beyond the classical SOC model framework [47]. We assume that a fractal set F is mapped to a self-affine time series $\mathcal{I}_S(t)$ via some dynamical process. A stationary convection (parallel transfer) of a fractal distribution near a rest-frame observer provides an example. For the observer, the motion of F appears as the field variation in time [128]. In the two-dimensional world ($n = 2$), the relation between d_f and δ_f is [129]

$$\delta_f + d_f = 3\,. \tag{5.30}$$

The generalization of Eqn (5.30) to an arbitrary dimension $n \geqslant 2$ [130] can be obtained by induction, with the system geometry in its cross sections by the plane E^2 taken into account. Letting $d_f \to 1$ in Eqn (5.30), we recover condition (5.25). Formula (5.30) expresses the mutual dependence of dynamical (δ_f) and structural (d_f) properties of a turbulent ensemble with fractal space–time organization. Combining Eqns (5.20) and (5.30), it is straightforward to obtain [47, 49]

$$\varpi = 2d_f - 1\,. \tag{5.31}$$

Equation (5.31) reproduces the rose noise in the limit as $d_f \to 1$.

5.6 Superdiffusion near SOC

Combining proportionality relation (4.20) with condition (5.29), we obtain the upper limit $H = H_{\max} = \mathcal{C}/2 \sim 2/3$ for the exponent H that characterizes strange transport processes in turbulent media. The value $H = H_{\max}$ coincides with Eqn (3.19) and corresponds to the maximum intense superdiffusion in the system. Thus, superdiffusion processes reach their 'apogee' in the SOC regime. The equality $H = H_{\max}$ assumes the dominant role of persistent FTRWs and Levy processes in the turbulent region [84]. The value $H = \mathcal{C}/2 \sim 2/3$ corresponds well with the experimental result $H \sim 0.6 - 0.75$ [63, 73, 74] for turbulent electric currents in tokamaks as the nonequilibrium magnetic field and plasma system approaches SOC. Remarkably, the regime $H \sim 0.6 - 0.75$ is always accompanied by the rose noise $P(f) \sim f^{-1}$ in the turbulent region [73, 74]. These results reveal the presence of an inherent relation between the turbulent transport kinetics and the color of noise in a dynamical system [84].

6. Fluctuation spectra in the magnetotail

We illustrate the spectral properties of dynamical systems near the NESS with the example of turbulent current sheets in the earth's magnetotail (Fig. 8, right of the X-line). The magnetotail is a unique laboratory in which nature itself performs the experiment on self-regulation of fields and currents, which has been tuned over billions of years. Under the merciless pressure of the solar wind, these fields and currents form a fragile dynamic organism that lives by its own laws but constantly has to adjust to ever-changing external conditions determined by interplanetary plasma fluctuations. The challenge of the turbulent current sheet problem is closely related to the explanation of the structural stability of the earth's magnetotail in the regions with a negligibly small regular component of the magnetic field normal to the neutral plane [50]. Formally [51],

$$B_n \lesssim 10^{-2} B_0\,, \tag{6.1}$$

where B_n is the normal field component and B_0 denotes the characteristic magnetic field in the northern and southern lobes forming an extended magnetic train of anti-parallel field lines enveloping the current system of the tail as it interacts with interplanetary plasma. Condition (6.1) is satisfied in the distant magnetotail ($R \gtrsim (50 - 100) R_E$) and in the domain of the magnetosphere substorm development ($R \sim (10 - 20) R_E$) at the stage where the magnetic configuration of the current sheet is locally thinning and elongating.

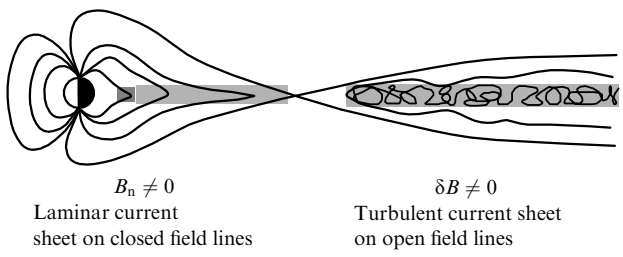

Figure 8. Current sheets in the magnetotail. Laminar regimes are observed in the near-tail domains with a nonzero normal component of the field providing the required magnetic viscosity of the medium. A laminar current sheet can be considered as a smooth deformation of the earth's dipole field. The transition to turbulence is connected with a sizeable local thinning and elongating of the dipole magnetic configuration that loses stability at small viscosities. Examples are the distant magnetotail on open field lines and the domain of the near-earth tail before the substorm.

(The geocentric distance R is measured in units of the earth's radius $R_E \sim 6.4 \times 10^3$ km.) To avoid misunderstanding, we emphasize here that we are not considering well-known laminar regimes related to objects in the tail that look like a 'squeezed' dipole (left of the X-line in Fig. 8). In the laminar regime, the cross-tail current, which maintains the lobe component of the magnetic field, appears due to the nonadiabaticity of ions in Spicer orbits [131]. The large-scale electric field advected into the magnetosphere due to the solar wind flowing round produces positive work in acting on the cross-tail current. It is partly spent to heating the 'cold' interplanetary plasma that somehow penetrates the current sheet and brings charged particles there. When the normal field component B_n drops below some critical threshold (of the order of $10^{-2}B_0$), the laminar configuration of the tail loses stability due to multi-scale penetration of turbulent fluxes. The transition to turbulence is due to the development of certain instabilities, for example stream ones [132, 133]. A strong multi-flux turbulence is a hierarchic network of current streams chaotically dispersed over the neutral plane of the tail (Fig. 9). Bending and branching of streams lead to the appearance of complex mosaics of turbulent magnetic field clots 'captured' by the current networks [47, 50]. The hierarchies of currents and fields near the ground NESS of a turbulent system form electrodynamically consistent fractal configurations. In the kinetic description, the turbulent magnetic field clots can be considered as scattering centers that prevent charged particles from rapidly passing through the current sheet under the action of the magnetosphere electric field. The particle scattering on the clots restricts the amplitude of the cross-tail electric current. Thus, a turbulent stable state is achieved, which stabilizes the electrodynamical ensemble near the NESS [50]. We stress that the turbulent field clots are formed from particles scattered over magnetic inhomogeneities. Current fluctuations due to the scattering process are the sources of the turbulent field that scatters the particles [49].

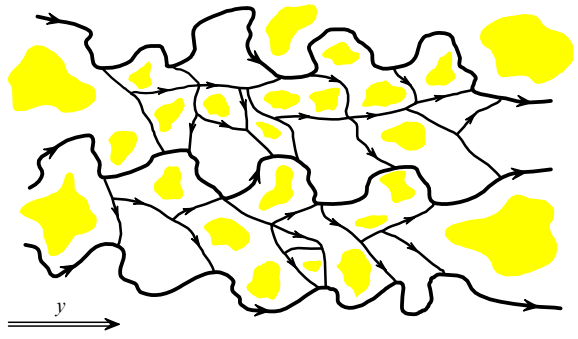

Figure 9. The structure of a turbulent current sheet near the NESS. Magnetic field clots correspond to irregular blobs surrounded by stream lines.

6.1 Rose noise in the magnetotail

We first return to expression (5.7) for the interval of frequencies f where internal dynamical effects of the turbulent ensemble are important. In this case, the Doppler shift is caused by plasma convection along the tail with the velocity of the solar wind decelerated at the collisionless bow-shock behind the earth's dayside magnetopause. In the distant magnetotail (at geocentric distances R of the order of $100R_E$ and beyond), convection occurs much more slowly, $u \sim 50$ km s^{-1} [135]. For typical parameters of the turbulent current sheet, the characteristic clot velocity V is much less than u [130]. Correspondingly, condition (5.7) takes the form [47]

$$f \lesssim f_* \sim \frac{u}{\xi}\,. \tag{6.2}$$

To estimate the correlation length ξ, we take into account that the magnetoplasmic structures in the earth's magnetotail are modulated by periodic long-wave perturbations due to the tearing instability of the current sheet [136]. The minimal wavelength of the tearing modes is of the order of $\lambda_* \sim 2\pi L$ [137], where L is the characteristic thickness of the sheet. Therefore,

$$\xi \sim \lambda_* \sim 2\pi L\,. \tag{6.3}$$

The value L for the distant tail is $L \sim 4 \times 10^3$ km [138] and, hence, the correlation length $\xi \sim 2.5 \times 10^4$ km. A realistic value L for a thin elongated tail in the magnetosphere substorm domain is $L \sim 1 \times 10^3$ km [135], and the correlation length is $\xi \sim 6.5 \times 10^3$ km. In both cases, we find from condition (6.2) that

$$f \lesssim f_* \sim 1 \times 10^{-2}\ \text{Hz}\,. \tag{6.4}$$

Rose noise (5.27) corresponds to frequency interval (6.2), (6.4) and appears due to energy pumping into the tearing modes. Low-frequency noises with properties similar to those of the rose noise, $P(f) \sim f^{-1}$, have indeed been discovered in the magnetotail (both distant and near) at $f \lesssim 1 \times 10^{-2}$ Hz in the course of independent megnetoplasmic experiments [126, 138 – 140]. A detailed discussion of these results can be found in [47, 51, 130].

6.2 Power-law spectra at intermediate frequencies

The role of convection is far from restricted by Doppler correction (5.7) to the frequency f_*. Important events occur at the intermediate frequencies

$$f_* \lesssim f \lesssim f_{**}\,, \tag{6.5}$$

$$f_* \sim \frac{|V-u|}{\xi}\,, \quad f_{**} \sim \frac{|V \pm u|}{a}\,, \tag{6.6}$$

where $a \ll \xi$ characterizes the minimal linear scale of turbulent magnetic field clots. A self-consistent estimate of a is obtained in Section 7. The frequency interval in (6.5) and (6.6) describes the field variations due to the (bulk) motion of the fractal structure relative to a rest-frame observer. The inhomogeneities corresponding to the wave vector $1/\xi \lesssim k \lesssim 1/a$ are then related to the field variations with the frequency $f \sim ku$. According to Eqn (5.1), the picture of the field taken with exposure time $\tau \ll \tau_* \sim 1/f_*$ resolves the fractal structure of the ensemble at scales within the interval $[\sim a, \sim \xi]$. Let the Hausdorff dimension of the turbulent set be d_f, as above. In the rest frame of the observer, the stationary convection of the fractal distribution is interpreted as field variations in time with the statistics of a self-affine time series $\mathcal{I}_S(t)$. The Hausdorff dimension δ_f of the series $\mathcal{I}_S(t)$ is related to the parameter d_f through Eqn (5.30).

6.3 Dark-brown noise in the magnetotail

If the diverse 'zoo' of magnetoplasmic instabilities developing in the magnetotail as it approaches the NESS had not obeyed the strict rules of collective behavior (see Fig. 1), the

fine structure of the turbulent current sheet would have evolved in a chaotic pile of magnetic fluctuations reminiscent of a random Brownian landscape [9], a geometric image of unpredictability. The cross section of the Brownian landscape by the current sheet plane would then be a fractal distribution with the Hausdorff dimension $d_f = 3 - \delta_f = 2 - S = 3/2$, where $S = 1/2$ is the similarity exponent of the random process [see Eqns (5.12) and (5.30)]. Convection of such a distribution along the tail segments would give rise to brown noise [28]

$$P(f) \sim f^{-2}\,, \tag{6.7}$$

where the frequency is $f_* \lesssim f \lesssim f_{**}$ and the power-law spectral exponent is $\varpi = 2d_f - 1 = 3 - 2S = 2$ in accordance with Eqns (5.18) and (5.31).

Due to multi-scale correlations, which 'synchronize' different partial instabilities (near the marginal NESS) into a single universal 'mode' (see Fig. 1), the observed value of the parameter ϖ can differ from two. (We always imply *magnetic* field fluctuations when considering turbulence spectra. Spectral properties of the velocity field can have somewhat different characteristics [47, 143].) In Section 7, we consider a self-consistent fractal model of a turbulent current sheet taking long-range correlation effects into account. According to the model, the value of the exponent ϖ at intermediate frequencies $f_* \lesssim f \lesssim f_{**}$ is close to 7/3, which adds black color to brown noise (6.7). However, dark tones correspond quite adequately to the reality: according to different cosmic experiments [126, 138–142], including magnetosphere studies in the framework of the Interball program (A Petrukovich, private communication), the value of ϖ at frequencies f from $f_* \sim 1 \times 10^{-2}$ Hz up to dozens of Hertz lies within the range from 2 to 2.5. Power spectra registered in turbulent current sheets are thus indeed 'painted' dark.

According to Eqns (6.5) and (6.6), when passing the frequency $f_* \sim 1 \times 10^{-2}$ Hz, the magnetotail noises change their color from rose to dark-brown as the frequency increases. The color change signals the presence of a characteristic 'kink' in the turbulence spectrum separating smoother ($\sim f^{-1}$) and steeper ($\sim f^{-7/3}$) components of the dependence $P(f)$ (Fig. 10). The kink at the frequency

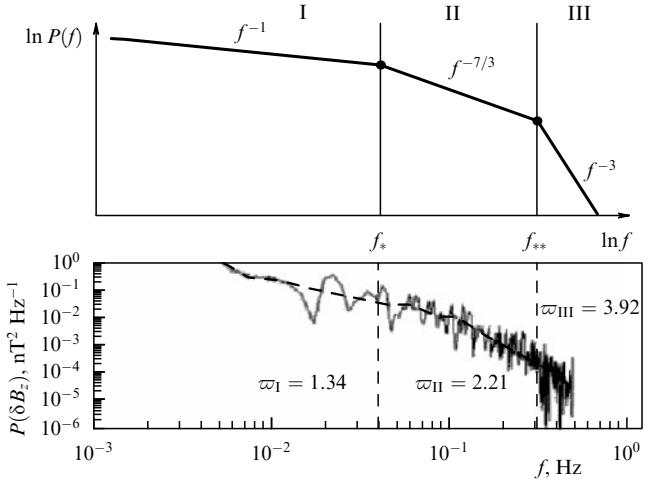

Figure 10. Color noises in the Earth's magnetotail. I — the low-frequency rose noise; II — the dark-brown noise at intermediate frequencies; III — blackening of the noises with frequency.

$f_* \sim 1 \times 10^{-2}$ Hz is a peculiar 'calling card' of the magnetoplasmic turbulence in the current sheet of the tail [126, 138–142]. As follows from the above considerations, the appearance of the kink can be explained by the convection of the fractal pattern on which slow collective motions are excited. The rose noise at low frequencies is then due to the tendency of dynamical excitations to obey the SOC conditions, while the dark-brown noise at intermediate frequencies is caused by rapid transport of fractal configurations (as a whole) relative to a rest-frame observer. In this connection, the rose noise in the magnetotail can be called dynamical, while the dark-brown noise structural. This standpoint is discussed in the original papers [47, 51, 130] in detail.

6.4 Black noise at high frequencies?

In conclusion, we address feasible spectral properties of magnetoplasmic turbulence in the earth's magnetotail at higher frequencies

$$f \gtrsim f_{**} \sim \frac{|V \pm u|}{a}\,. \tag{6.8}$$

Interval (6.8) corresponds to wave vectors $k \gtrsim 1/a$ characterizing a possible distribution of the magnetic field inside the clots. Treating clots as structureless, we assign them integer-valued Hausdorff dimension $d_f = 2$ coinciding with the topological dimension of the embedding space (in our case, the dimension of the neutral plane of the tail $n = 2$). As follows from Eqn (5.31), the exponent characterizing the spectrum at frequencies $f \gtrsim f_{**}$ is $\varpi = 2n - 1 = 3$. This value is associated with black noise [28],

$$P(f) \sim f^{-3}\,. \tag{6.9}$$

For the assumption about the fractal properties of mosaics to be meaningful, the size of turbulent magnetic field clots a near the marginal NESS of the system should be smaller than the correlation length ξ by at least an order of magnitude. Correspondingly, the black noise $P(f) \sim f^{-3}$ in the magnetotail could manifest itself at frequencies above

$$f_{**} \gtrsim 10 \times f_* \sim 1 \times 10^{-1}\ \text{Hz}\,. \tag{6.10}$$

Estimate (6.10) is made more precise in Section 7: $f_{**} \sim (2-3) \times 10^{-1}$ Hz. For comparison, the Nyqvist frequency, measured by the Geotail satellite that provided unique information on the fine structure of turbulence in the distant magnetotail of the earth, was exactly 0.17 Hz [17], close to the value of f_{**}. In this connection, crossover to the black noise at high frequencies $f \gtrsim (2-3) \times 10^{-1}$ Hz should be considered a theoretical prediction of the fractal model [47]. Some preliminary results obtained recently are evidence of such a crossover (G Consolini, private communication). The color change of the noise at frequencies $f \sim f_{**} \sim (2-3) \times 10^{-1}$ Hz signifies the formation of the second kink in the turbulence spectrum (see Fig. 10), in addition to the kink at frequencies near $f \sim f_* \sim 1 \times 10^{-2}$ Hz [47]. Similarly to dark-brown, black noise is structural (in the sense discussed in Section 6.3). The deviation of $P(f)$ from black noise at high frequencies (6.10) can indicate an instability of the electron component of the current and the appearance of magnetic inhomogeneities with wavelengths much shorter than a [47]. A thorough study of color noises in the earth's magnetotail could significantly extend the understanding of the superfine structure of current

sheets and of dynamical processes in nonequilibrium cosmic plasma.

7. A self-consistent fractal model of the turbulent current sheet

7.1 System of equations for the current sheet

We consider an electrodynamic system of the turbulent current sheet at long times such that residual relaxation effects accompanying its transition to the NESS can be disregarded. We introduce the coordinate frame (x, y, z) with the axes directed as follows: x along the fields, y across the sheet, and z along the normal to the neutral xy plane. (In geophysical literature, such a frame is usually referred to as GSM.) The total current $\mathbf{j}$ across the tail can be represented as a sum of a nonzero mean current along y and the fluctuating component $\delta\mathbf{j}$ lying in the xy plane:

$$\mathbf{j} = \langle \mathbf{j}_y \rangle + \delta\mathbf{j}\,, \tag{7.1}$$

$$\delta\mathbf{j} = \delta\mathbf{j}\,(x, y)\,, \tag{7.2}$$

$$\langle \mathbf{j}_x \rangle = \langle \mathbf{j}_z \rangle = 0\,. \tag{7.3}$$

Near the marginal NESS turbulent ensemble (i.e., the one with the lowest energy), the normal component of the current $\delta\mathbf{j}$ is assumed to be zero. In other words, the geometry of fields and currents stabilizing the electrodynamical system of the tail is close to a two-dimensional distribution. In the present review, we do not consider more complicated (three-dimensional) (quasi)-stationary configurations. Because the vector $\delta\mathbf{j}$ lies in the xy plane, only the normal component of the turbulent magnetic field $\delta\mathbf{B}$ is nonzero:

$$\delta\mathbf{B} = \delta\mathbf{B}_z\,(x, y)\,. \tag{7.4}$$

For the fields in lobes, we have

$$\mathbf{B} = \mathbf{B}_x\,(z)\,. \tag{7.5}$$

The Maxwell equations for the turbulent ensemble in the neutral plane of the current sheet become

$$\operatorname{rot}\mathbf{B}_x = \frac{4\pi}{c}\langle \mathbf{j}_y \rangle\,, \tag{7.6}$$

$$\operatorname{rot}\delta\mathbf{B}_z = \frac{4\pi}{c}\,\delta\mathbf{j}\,. \tag{7.7}$$

System of equations (7.6), (7.7) should be supplemented by the continuity equation

$$\operatorname{div}\mathbf{j} = 0\,, \tag{7.8}$$

where $\mathbf{j}$ is determined by Eqn (7.1).

7.2 Self-consistent estimate of the clot size

Our first goal is to study the fractal structure of a nonadiabatic turbulent current sheet in the self-consistent regime [47, 49]. We first estimate the parameter a determining the minimal size of turbulent magnetic field $\delta\mathbf{B}_z$ clots in the layer. We assume the field $\delta\mathbf{B}_z$ to be generated by particles participating in the nonadiabatic scattering process. *A priori*, the Larmor radius of such particles can be considered comparable to the clot size: $\ell_{\mathrm{L}} \sim a$. To be specific, we relate the nonadiabatic effects to ions, the heavier species of the plasma; electrons are then treated as a background providing the overall quasineutrality of the system. The current sheet conductivity is then limited by the scattering frequency of particles (ions) on the turbulent magnetic field clots $\delta\mathbf{B}_z$. We note that the value of ℓ_{L} in the nonadiabatic current sheet has the meaning of the curvature radius of the trajectory at the scattering point. Because the ions have no chance to complete a circle around the field $\delta\mathbf{B}_z$, the actual rotation covers an arc of the Larmor circle based on the angle $\chi \sim a/\ell_{\mathrm{L}}$. Maxwell equations (7.6), (7.7) imply that by an order of magnitude,

$$\langle j_y \rangle \sim \frac{c}{4\pi}\,\frac{B_0}{L}\,, \tag{7.9}$$

$$\delta j \sim \frac{c}{4\pi}\,\frac{\delta B_z}{a}\,, \tag{7.10}$$

where L is the characteristic thickness of the sheet and δB_z is the amplitude of the field $\delta\mathbf{B}_z$. It is easy to see that relative fluctuations in the current $\delta j/\langle j_y \rangle$ in the neutral plane of the sheet are of the order of the scattering angle χ:

$$\chi \sim \frac{a}{\ell_L} \sim \frac{\delta j}{\langle j_y \rangle}\,. \tag{7.11}$$

Eliminating currents from Eqns (7.9) and (7.10) via Eqn (7.11), we arrive at a self-consistent estimate of the parameter a,

$$a \sim \sqrt{bL\ell_{\mathrm{L}}}\,, \tag{7.12}$$

where $b \equiv \delta B_z/B_0$. We note that the quantity $\ell_0 \sim b\ell_{\mathrm{L}}$ is the Larmor radius of particles in the field B_0. According to Eqn (7.12), the clot size a is the geometric mean of the sheet thickness L and the Larmor radius ℓ_0:

$$a \sim \sqrt{L\ell_0}\,. \tag{7.13}$$

The scale a thus depends solely on external conditions characterizing the magnetic field properties in the lobes of the tail. Because $\ell_0 \sim wmc/eB_0$, Eqn (7.13) yields [49]

$$a \sim \sqrt{\frac{wmcL}{eB_0}}\,. \tag{7.14}$$

The parameters m and e determine the mass and charge of the current carriers. The quantity w can be considered as a 'thermal' particle (ion) velocity in the neutral plane of the tail: $w \sim \sqrt{2T/m}$; here, T should be treated as a generalized temperature that takes long-range correlations in the system into account [144]. The magnetic field in the magnetospheric lobes can be straightforwardly estimated from the pressure balance as $B_0 \sim \sqrt{8\pi\rho T/m}$, where ρ is the mean plasma density in the sheet. The last estimate holds if $b^2 \ll 1$. (One can show [51] that near the marginal NESS, relative fluctuations of the magnetic field in the sheet are of the order of $b \sim 0.3$.) From relation (7.14), we infer

$$a \sim \frac{\sqrt{mcL/e}}{\sqrt[4]{4\pi\rho}}\,. \tag{7.15}$$

For typical plasma densities ρ and sheet thickness L [134, 135, 138], the size of turbulent magnetic field clots is, according to

Eqn (7.15), $a \sim 8 \times 10^2$ km in the distant tail of the earth's magnetosphere ($R \gtrsim 10^2 R_E$) and $a \sim 4 \times 10^2$ km in the near-earth tail at the initial substorm growth phase ($R \sim 10 R_Z$). The ratio of the correlation length ξ to the clot size a is $\xi/a \sim 30$ and $\xi/a \sim 20$ in the distant and near-earth tail, respectively, before the substorm. Finally, a more precise estimate (6.10) of the frequency f_{**} determining the transition from the dark-brown to black noise is $f_{**} \sim 3 \times 10^{-1}$ Hz and $f_{**} \sim 2 \times 10^{-1}$ Hz in the distant and near-earth magnetotail, respectively. The discussion of these results in light of available experimental data can be found in [47, 51].

7.3 Estimate of the turbulent transport coefficient

To determine the turbulent transport coefficient $\mathcal{D}$ in a self-consistent current sheet, we return to Eqns (3.5) and (3.6) describing the kinetics of random processes in a fractal geometry. We rewrite Eqn (3.5) as

$$\left\langle \mathbf{r}^2(t) \right\rangle = 2\mathcal{D}\tau \left(\frac{t}{\tau} \right)^{2/(2+\theta)}, \tag{7.16}$$

where the elementary time step of the motion, $\tau \sim a/w$, is chosen. Taking into account that a particle moves over a distance of the order of the Larmor radius ℓ_L in a time of the order $t \sim \ell_L/w$, we have from Eqn (7.16) that

$$\ell_L^2 \sim 2\mathcal{D} \frac{a}{w} \left(\frac{\ell_L}{a} \right)^{2/(2+\theta)}, \tag{7.17}$$

and hence the turbulent transport coefficient is

$$\mathcal{D} \sim \ell_L^2 \frac{w}{2a} \left(\frac{a}{\ell_L} \right)^{2/(2+\theta)}. \tag{7.18}$$

The parameter θ is the connectivity index of the fractal mosaic in the current sheet neutral plane. In the Euclidean limit $\theta \to 0$, Eqn (7.18) yields $\mathcal{D} \sim \ell_L w/2$. We emphasize that in the general case, the coefficient $\mathcal{D}$ depends on the clot size a: $\mathcal{D} \propto a^{-\theta/(2+\theta)}$. Because the Larmor radius ℓ_L of a particle is inversely proportional to the field $b \equiv \delta B_z/B_0$, the turbulent transport coefficient $\mathcal{D}$ decreases in accordance with a power law with b,

$$\mathcal{D} \propto b^{-2(1+\theta)/(2+\theta)}. \tag{7.19}$$

To evaluate the effective conductivity Υ of the sheet, we use the well-known formula [145] $\Upsilon \sim [\rho e^2/m^2]\Theta$, where Θ is the characteristic collisional time. The parameter Θ can be expressed through the turbulent transport coefficient $\mathcal{D}$ as $\Theta \sim a^2/\mathcal{D}$, and hence

$$\Upsilon \sim \frac{\rho e^2 a^2}{m^2} \times \mathcal{D}^{-1}. \tag{7.20}$$

Combining Eqns (7.19) and (7.20), we obtain the conductivity of a turbulent current sheet behaving as the magnetic field b raised to the power $2(1+\theta)/(2+\theta)$,

$$\Upsilon \propto b^{2(1+\theta)/(2+\theta)}. \tag{7.21}$$

In the Euclidean limit $\theta \to 0$, we have

$$\Upsilon \sim \frac{2\rho e^2 a^2}{w \ell_L m^2} \propto b.$$

7.4 Consistency condition

Anomalous behavior of the conductivity Υ with the magnetic field $b \equiv \delta B_z/B_0$, Eqn (7.21), must be made consistent with electrodynamic equations (7.6) and (7.7) describing fundamental structural properties of the magnetic field and plasma turbulence near the NESS. We now show that the consistency condition can be expressed as a relation between the Hausdorff dimension d_f of the mosaic and the connectivity index θ. Indeed, the mean current across the sheet $\langle j_y \rangle$ is proportional to the large-scale magnetospheric electric field E_y directed along the dawn–dusk line: $\langle j_y \rangle \sim \Upsilon E_y$. (This relation is Ohm's law for the mean current.) Because E_y is an external parameter (with respect to the electrodynamic system of the tail), the dependence of $\langle j_y \rangle$ on the turbulent magnetic field amplitude $\delta \mathbf{B}_z$ coincides with Eqn (7.21):

$$\langle j_y \rangle \propto b^{2(1+\theta)/(2+\theta)}. \tag{7.22}$$

According to Eqn (7.11), relative fluctuations of the current $\delta j/\langle j_y \rangle$ in the neutral plane of the tail are of the same order as the scattering angle $\chi \sim a/\ell_L$. Because $\ell_L \propto b^{-1}$, the turbulent component δj is

$$\delta j \propto b \times b^{2(1+\theta)/(2+\theta)}. \tag{7.23}$$

The turbulent magnetic field amplitude is treated as a function of the radial scale r in the xy plane,

$$b = b(r). \tag{7.24}$$

Below, we are interested in the interval $a \lesssim r \lesssim \xi$ corresponding to a self-similar distribution of the field clots in mosaics. The quantity $b(r)$ in Eqn (7.24) is understood as the mean (by absolute value) magnetic field on the scale r; $b^2(r)$ then has the meaning of the mean energy density $\varepsilon(r)$ for the fractal distribution:

$$\varepsilon(r) \propto b^2(r). \tag{7.25}$$

The function $\varepsilon(r)$ for fractal fields can be expressed through the density of structural elements $\Im(r)$ forming the fractal set; we recall that the function $\Im(r)$ is determined by Eqn (2.2). Correspondingly, for $n = 2$, we have

$$\varepsilon(r) \propto \Im(r) \propto r^{d_f - 2}, \tag{7.26}$$

where d_f is the Hausdorff dimension of the turbulent mosaic. From the last two equations, we find

$$b^2(r) \propto r^{d_f - 2}. \tag{7.27}$$

Returning to Eqn (7.23), we fix the dependence of the right-hand side of (7.7) on the magnetic field b:

$$\text{r.h.s.} \propto b \times b^{2(1+\theta)/(2+\theta)}. \tag{7.28}$$

On the left-hand side of (7.7), the rot operation, which has the natural representation in the standard basis of three orthonormal vectors, is applied to the field $\delta \mathbf{B}_z(x, y)$ with a low dimension $d_s = 2d_f/(2+\theta) \leqslant d_f < 2$. As a result, the vector product $\nabla_{\mathbf{r}} \times \delta \mathbf{B}_z$ is overdetermined, which leads to a power-law decay of the rot in the xy plane [50],

$$\text{rot} \propto r^{-\theta/(2+\theta)}. \tag{7.29}$$

The exponent in Eqn (7.29) depends solely on the connectivity index θ characterizing the deviation of the spectral dimension d_s from the Hausdorff dimension d_f. In the Euclidean limit ($\theta \to 0$), we have rot $\propto$ const (r), as should be the case. As a function of r, the left-hand side of Eqn (7.7) therefore takes the form

$$\text{l.h.s.} \propto b \times r^{-\theta/(2+\theta)} . \tag{7.30}$$

From Eqns (7.28) and (7.30), we derive

$$b^2(r) \propto r^{-\theta/(1+\theta)} . \tag{7.31}$$

Comparing Eqn (7.31) with Eqn (7.27), we obtain the desired consistency condition

$$d_f = 2 - \frac{\theta}{1+\theta} . \tag{7.32}$$

In the limit as $\theta \to 0$, we have $d_f \to 2$, i.e., fluctuations fill the xy plane if Euclidean connectedness is imposed.

7.5 The values of the Hausdorff dimension and the connectivity index

Consistency condition (7.32) is one of two equations needed to unambiguously determine the parameters d_f and θ near the marginal NESS of a turbulent system. Criticality condition (2.10) ensuing from the universal value theorem can be taken as the second equation. In terms of d_f and θ, condition (2.10) can be written as

$$\frac{2d_f}{2+\theta} = \mathcal{C} \approx 1.327\ldots \sim \frac{4}{3} , \tag{7.33}$$

where we use definition (2.7) for the spectral dimension d_s. Combining Eqns (7.32) and (7.33), we find the Hausdorff dimension d_f and connectivity index θ as [47]

$$d_f = \frac{2+\mathcal{C}}{2} \approx 1.66\ldots \sim \frac{5}{3} , \tag{7.34}$$

$$\theta = \frac{2-\mathcal{C}}{\mathcal{C}} \approx 0.51\ldots \sim \frac{1}{2} . \tag{7.35}$$

The values in (7.34) and (7.35) fully describe the fractal geometry of a turbulent current sheet near the marginal NESS. We stress that in the marginal state, turbulent mosaics fill in only a fractal subset of the neutral plane with the Hausdorff fractal dimension $d_f \sim 5/3 < 2$.

According to Eqns (3.5) and (7.16), the mean-square particle displacement $\langle \mathbf{r}^2(t) \rangle$ across the sheet increases with time t as t^{μ} with the exponent $\mu = 2/(2+\theta)$. From Eqn (7.35), we infer $\mu = 2\mathcal{C}/(2+\mathcal{C}) \sim 0.8$. Accordingly, the exponent $H = \mathcal{C}/(2+\mathcal{C}) \sim 0.4$. Because $H < 1/2$, a subdiffusive particle transport is realized. The estimate $H \sim 0.4$ is confirmed by numerical experiments [64] focusing nonadiabatic particle dynamics in turbulent current sheets. The 'characteristic' trajectory of a particle, an ion, in the neutral plane of the current sheet at $b \sim 0.3$ is shown in Fig. 6 [64].

7.6 Fluctuation spectrum at intermediate frequencies

We now fulfill the promise given in Section 6.3 about an accurate calculation of the Fourier exponent of energy density ϖ at intermediate frequencies. Substituting the Hausdorff dimension d_f from Eqn (7.34) in Eqn (5.31), we obtain [47, 51]

$$\varpi = \mathcal{C} + 1 \approx 2.33\ldots \sim \frac{7}{3} , \tag{7.36}$$

$$P(f) \sim f^{-7/3} , \tag{7.37}$$

in good agreement with observational data [126, 138 – 142]. The difference between spectrum (7.37) and brown noise is due to long-range correlation effects imposing a certain schedule on the behavior of turbulent system at the NESS. A detailed comparison of Eqn (7.37) with experiment is given in [47, 51].

7.7 The phenomenon of the magnetospheric substorm

We note in conclusion that the (quasi)-two-dimensional distributions in (7.6) and (7.7) corresponding to the marginal NESS of the turbulent current sheet turn out to be unstable when the cross-tail potential drop exceeds some critical value. Indeed, the potential drop is a fluctuating quantity depending on the 'weather conditions' in the vicinity of the magnetosphere. The worsening of space weather caused by perturbations on the sun can feed high voltage to the current sheet for a short time, thereby inducing a jump in the cross-tail electric current $\langle \mathbf{j}_y \rangle$. The increased cross-tail current short-circuits the conducting elements that form a ramified fractal network in the neutral plane; the current web coarsens and splits into separate filaments, while dense clumps of the turbulent magnetic field block the neutral plane and squeeze the current out. As a result, the magnetotail current system

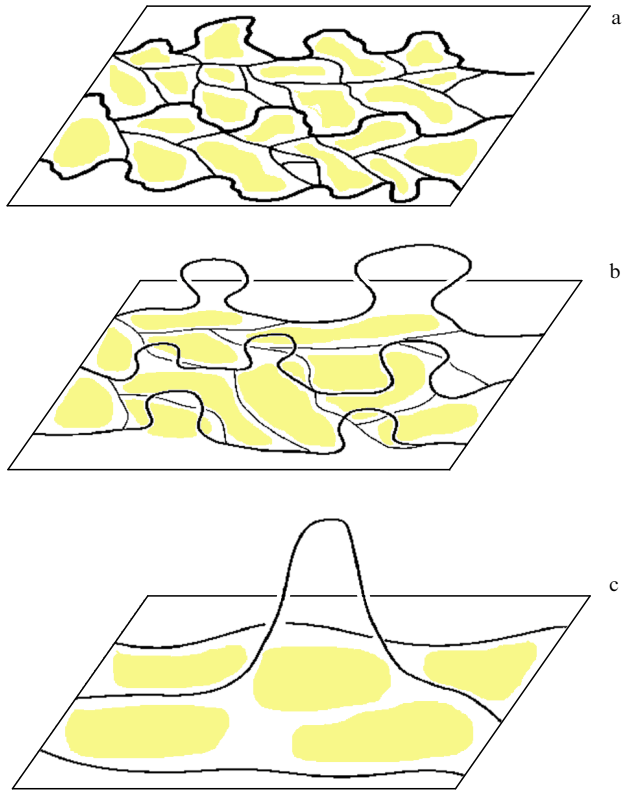

Figure 11. Coarsening of current web with potential difference increase across the tail. (a) Topology of fields and currents near the ground non-equilibrium (quasi)-stationary state. (b) The appearance of primary current fluctuations outside the neutral plane. (c) The formation of large-scale loops overhanging the current sheet.

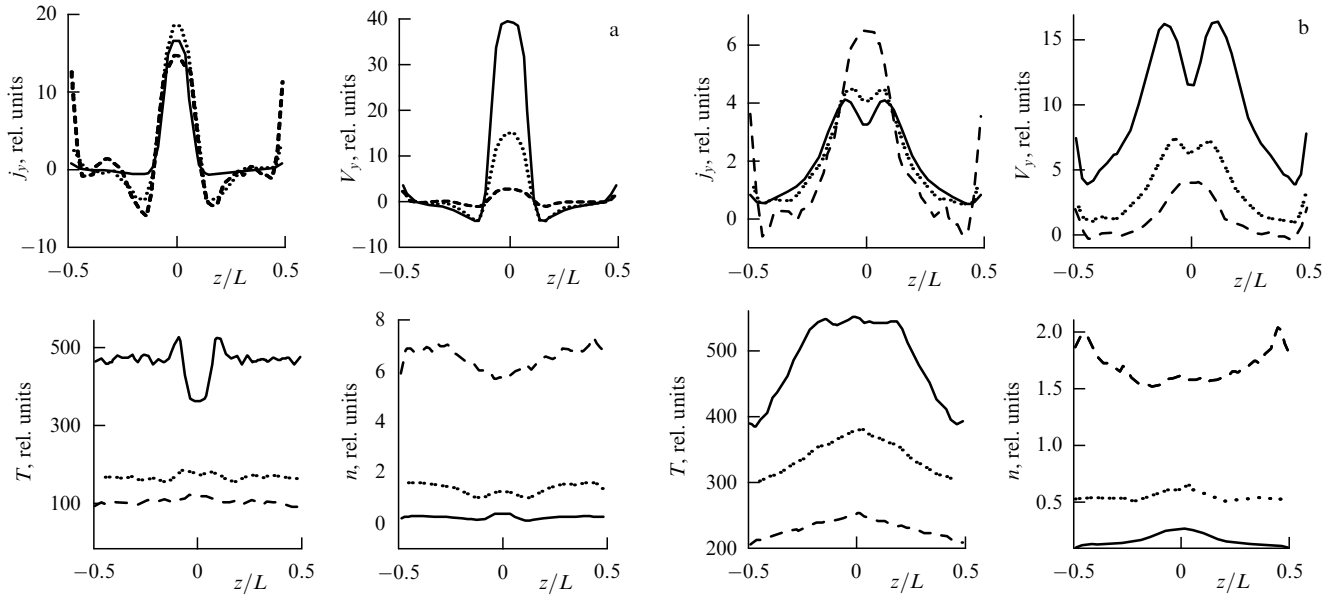

Figure 12. (a) The vertical profile of the current below the loop emergence threshold ($b \leqslant 0.3$). The distribution is characterized by a sharp maximum near the neutral plane $z = 0$. Also shown is the profile of the transverse particle velocity, V_y. The results are obtained by numerical simulation for three different particle densities n and plasma temperatures T at the current sheet boundaries. The dashed, long-dashed, and solid lines correspond to different boundary conditions. (b) The same as in Fig. 12a but above the loop emergence threshold ($b \geqslant 0.3$). The double-peaked profile of the current and velocity indicates that particles prefer 'overjumping' through the magnetic blobs instead of 'passing' through the field inhomogeneities staying all the way in the neutral plane. Once particles start 'jumping' intensively (for example when high voltage is applied to the sheet), the current system 'crawls away' to form loops.

evolves into loop-like segments overhanging the neutral layer. Magnetic field clumps located at the base of the loops do not allow particles to pass through the layer, constantly keeping them in the neutral plane [51]. The sequence of events is presented in Fig. 11.

The formation of loops upon increasing the magnetic field in clumps is confirmed by numerical simulation results [51]. In Fig. 12, as an illustration, we plot the vertical profile of the current $\langle \mathbf{j}_y \rangle$ as a function of z for two characteristic values of the turbulent field amplitude $b \equiv \delta B_z / B_0$ corresponding to the system state before (Fig. 12a) and after (Fig. 12b) the loops come out of the current sheet neutral plane [51]. In the first case ($b \lesssim 0.3$), the profile is single-peaked with a sharp maximum near the neutral plane $z = 0$; in the second case ($b \gtrsim 0.3$), the profile is double-peaked with two symmetric maxima above and below the neutral plane $z = 0$. As the turbulent sheet amplitude increases ($b \gtrsim 0.3$), the double-peaked structure becomes more pronounced: the maxima shift towards the lobes (i.e., the height of the loops increases) and the dip at $z = 0$ becomes progressively deeper [51]. The output threshold $b \sim 0.3$ (corresponding to some critical potential drop across the sheet) describes the limiting (quasi)-two-dimensional topology of the turbulent ensemble.

Above the threshold, the coarsening of the conducting web can be connected with the structural reorganization of the turbulent system. Indeed, we consider a loop of height z overhanging the neutral plane (Fig. 13). Stability analysis of such a loop reduces to calculating its free energy $\mathcal{F}$ as a function of z. As the loop floats up, two main effects occur: 1) tensions appear in the system that tend to return the loop to its original position; 2) the emerging loops are reoriented relative to the magnetic field in the lobes. As usual, a quadratic contribution to the free energy of the system is related to tensions, $\mathcal{F}_1 \sim pz^2$, where p is the elasticity of the conducting web. The web coarsening results in a gradual

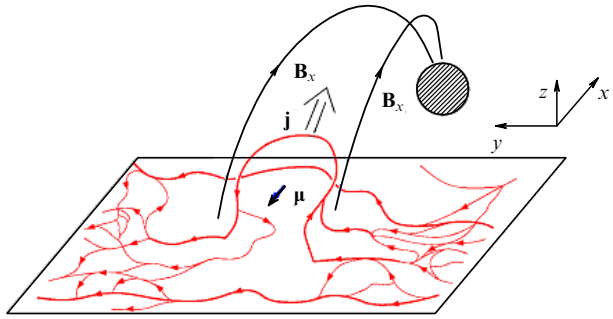

Figure 13. The interaction between current loops and the magnetic field in the lobes of the tail. When a loop emerges, the magnetic moment $\boldsymbol{\mu}$ is directed opposite to the field $\mathbf{B}_x$ and its absolute value is proportional to z.

decrease in p as the underlying conducting elements become short-circuited. Conversely, the reorientation is manifested in the tendency of the magnetic moment of the loop to lie along the magnetic field inside the lobes (when loops are emerging, their magnetic moment is directed against the field). The gain in the free energy at the 'right' position of the dipole is $-\mathcal{F}_2 \sim (q_0/B_0)\, zB_x(z)$. In contrast to the elasticity coefficient p, the quantity q_0 takes a constant value independently of how coarse the conducting web is. By its physical meaning, the parameter q_0 characterizes the interaction between the loops and the lobe field and is insensitive to the geometry of the current system in the neutral plane of the tail. The dependence of the mean magnetic field in the lobes on z can be estimated from the well-known Harris distribution [146] describing a self-consistent current sheet equilibrium in the direction normal to the neutral plane: $B_x(z) \sim B_0 \tanh z$. We note that z is measured in units of the current thickness L [146]. Hence, we have $-\mathcal{F}_2 \sim q_0 z \tanh z$. Combining con-

tributions (1) and (2), we obtain the total free energy of a loop

$$\mathcal{F}(z) \sim pz^2 - q_0 z \tanh z\,. \tag{7.38}$$

Expanding $\tanh z$ in a Taylor series at small z and retaining second-order terms, we find from Eqn (7.38) that [47, 51]

$$\mathcal{F}(z) \sim (p - q_0)\, z^2 + \left(\frac{q_0}{3}\right) z^4\,. \tag{7.39}$$

Expansion (7.39) coincides with the free energy expansion in the order parameter in the Landau theory of second-order phase transitions [147]. In this case, the loop height z may be considered a suitable order parameter. If $p > q_0$, the free energy $\mathcal{F}(z)$ reaches a minimum at $z = 0$. The stable state of the system corresponds to a (quasi-)two-dimensional configuration of fields and currents in Eqns (7.6) and (7.7) with large surface tension. Conversely, for $p < q_0$, (quasi)-two-dimensional fractal distributions become unstable. The surface tension is no longer capable of preventing loops from emerging out of the neutral plane of the current sheet. The decrease in the free energy in the system is caused by a phase transition to three-dimensional turbulent structures involving the magnetic fields in the lobes. Transition (7.39) is related to an increase in the embedding space topological dimension (from $n = 2$ to $n = 3$) and mirrors fundamental changes in the turbulent ensemble symmetry [47]. The characteristic size of the turbulent domain along z is (in units of L)

$$\Delta z \sim \sqrt{\frac{3(q_0 - p)}{q_0}}\,. \tag{7.40}$$

For $\Delta z \sim 1$, the loops may short-circuit through the earth's ionosphere. The electric currents to and from the earth then flow along the magnetic field in the lobes (see Fig. 13). This effect causes a dramatic reorganization of the entire current system of the tail; its structure is reminiscent of the magnetospheric substorm phenomenon [47, 51]. In view of Eqn (7.39), the onset of the magnetospheric substorm can be considered a second-order phase transition from a (quasi)-two-dimensional to three-dimensional configuration of turbulent fields and currents in the magnetotail [47, 51]. The kinetics of the transition obey the Landau theory [147]. The onset occurs at $p = q_0$, which corresponds to some critical value of the cross-tail current $\langle \mathbf{j}_y \rangle$. The critical current provides marginal coarsening of the web when the loop formation becomes thermodynamically profitable.

The coarsening of the current system as $p \to q_0 + 0$ leads to a gradual blackening of the spectrum $P(f)$ at intermediate frequencies, and the second kink in the spectrum straightens [47, 51]. At the onset of a magnetospheric substorm (i.e., when the currents short-circuit through the ionospere), the power spectrum of the turbulent magnetic field [47, 51] is

$$P(f) \to f^{-3} \tag{7.41}$$

in the wide frequency range $f \gtrsim f_*$. The spectrum blackening mirrors the energy redistribution to larger scales as the mean cross-tail current increases. This effect is confirmed by analyzing the data on the turbulent magnetic field behavior before the substorm onset [148].

8. Strange accelerations in turbulent media

Up to now, we have neglected the effect of the internal NESS dynamics on the particle velocity distribution by actually disregarding both the energy exchange between plasma particles walking in the fractal set labyrinths and the scattering of particles by electromagnetic field fluctuations. We thus deliberately postponed the discussion of some important phenomena that mirror the essentially nonequilibrium nature of the turbulent state until we were interested in plasma heating mechanisms in turbulent media.

In fact, dynamic relaxation processes, which play (along with medium self-organization effects) the key role in the formation of the NESS, assume an energy exchange between different subsystems comprising the turbulent ensemble. These subsystems usually include turbulent fields interacting both with themselves and with particles captured by them. We note that the currents generated by the particles can themselves be a source of the turbulent field. The system is reminiscent of a 'boiling soup' of particles and fields 'balancing' each other near the NESS. Such states are analyzed in original papers [47, 49, 51, 99].

The transition of a turbulent system to the NESS is in many cases related to the occurrence of a population of energetic particles with the power-law velocity (energy) distribution functions

$$\psi(w) \propto w^{-\varrho}\,, \tag{8.1}$$

$$\psi(\mathcal{E}) \propto \mathcal{E}^{-\varrho/2}\,. \tag{8.2}$$

The particle energy $\mathcal{E} \propto w^2$ in Eqn (8.2) is large compared to the characteristic 'temperature' of the ensemble T, i.e., $\mathcal{E} \gg T$. We note that the quantity T may not have the conventional meaning of the thermodynamical temperature [144]. Distributions like (8.1) and (8.2) are frequently referred to as a 'superthermal tail' [149], stressing the existence of an extended 'train' of high-energy states with exponentially small Maxwell – Boltzmann probabilities:

$$\psi(w) \propto \exp\left(-\frac{w^2}{2T}\right), \tag{8.3}$$

$$\psi(\mathcal{E}) \propto \exp\left(-\frac{\mathcal{E}}{T}\right). \tag{8.4}$$

Expression (8.4) is the Gibbs distribution [147]. Nonthermal tails like (8.2) and (8.3) are an essential feature of turbulent plasma. As an example, we mention the populations on the earth's plasma sheet [149] and cosmic-ray particles [150].

It can be assumed that the power exponent in distribution (8.1) is related to fundamental processes underlying the nonlinear dynamics of the NESS state. The description of such processes requires taking multi-scale correlations in space and time into account (see Section 4) and can be assigned to the realm of strange kinetics [99]. Following [47, 99, 130], we start presenting the corresponding approach, with the key feature being a nonlinear fractional kinetic equation for the plasma particle velocity distribution

To be specific, we restrict ourselves to turbulent magnetic field and plasma systems with a large value of the parameter β (i.e., the plasma-to-field density ratio), $\beta \gg 1$. This condition is satisfied, in particular, for NESS's in the earth's magnetotail.

At large β, the processes of self-organization in the system result in the turbulent magnetic field concentrating into clots, which then form fractal 'mosaics' in the system configuration space. Mosaics are dynamical structures participating in the process of 'self-pouring' (see Section 5). In the simplest case, 'self-pouring' can be identified with slow collective wandering

of clots in the configuration space driven by some correlation effects. As an example, we mention fractal-time random walks (see Section 4) applied to the clots as 'elementary' field carriers. (An alternative approach appeals to clots at rest with the magnetic field explicitly depending on time. We do not consider this case.)

8.1 Fermi acceleration

The interaction of particles with clots leads to a gradual heating of the plasma. The explanation is that for a chaotic velocity distribution of clots, head-on collisions of clots with a particle dominate, which on average increases the particle kinetic energy [151]. This mechanism was first proposed by Fermi [152] under the assumption that particle scattering on clots ('magnetic clouds') has a random (Gaussian) character. In a Gaussian scattering, the mean-square variation in the particle velocity is proportional to the time particles stay in the turbulent domain:

$$\left\langle \delta \mathbf{w}^2(t) \right\rangle \propto t \,. \tag{8.5}$$

The variable $\mathbf{w}$ in Eqn (8.5) is the running value of the particle velocity vector. Dependence (8.5) leads to the standard diffusion equation for the probability density $\psi = \psi(t, \mathbf{w})$ [151]:

$$\frac{\partial \psi}{\partial t} = \Delta_{\mathbf{w}} \psi \,. \tag{8.6}$$

Process (8.6), corresponding to the Gaussian diffusive acceleration, can be considered a random Brownian motion of a particle in the (three-dimensional) space of velocities $\{\mathbf{w}\}$. We note that Eqn (8.6) is analogous to Eqn (3.14). In Eqn (8.6), $\Delta_{\mathbf{w}}$ is the standard three-dimensional Laplacian. The particle velocity distribution $\psi = \psi(t, \mathbf{w})$ satisfies the natural normalization condition [cf. (3.15)]

$$\int \psi \, \mathrm{d}\mathbf{w} = 1 \,. \tag{8.7}$$

8.2 Inclusion of correlations

Diffusion equation (8.6) resulting from the general properties of Gaussian random processes does not account for multi-scale space–time correlations that play the key role in the dynamics of the NESS. An adequate analysis of correlation phenomena requires rejecting the simplest model (8.5), (8.6) based on the notion of random Brownian motion. Relevant generalizations are facilitated by the theory of strange transport phenomena in the velocity space $\mathbf{w}$ [99]. Following the general methods described in Section 4, we replace diffusion equation (8.6) with a transport equation in fractional derivatives with respect to both variables t and $\mathbf{w}$ [99],

$$\frac{\partial^{\alpha} \psi}{\partial t^{\alpha}} = \nabla_{\mathbf{w}}^{2\beta} \psi \,, \tag{8.8}$$

where $0 \leqslant \alpha \leqslant 2$ and $1 \leqslant 2\beta < 2$ are generalized orders of differentiation. Equation (8.8) relates the principles of fractional dynamics to processes occurring in the phase space of a turbulent system.

8.3 Fractional time derivative

The derivative $\partial^{\alpha}/\partial t^{\alpha}$ on the left-hand side of Eqn (8.8) is defined through Riemann–Liouville operator (4.2), with the order $0 \leqslant \alpha \leqslant 2$ having the meaning of the fractal dimension of the 'active' time. The replacement $\partial/\partial t \to \partial^{\alpha}/\partial t^{\alpha}$ in diffusion equation (8.6) means the transition from random Brownian motion in the velocity space $\{\mathbf{w}\}$ to FTRWs. FTRW statistics were discussed in detail in Section 4 in the context of strange transport processes in the configuration space $\{\mathbf{r}\}$. The results obtained in Section 4 remain valid up to a substitution of the variable $\mathbf{r}$ for $\mathbf{w}$.

FTRW-like phenomena in the velocity space $\{\mathbf{w}\}$ are accelerations in the fractal time. For a particle that is being accelerated in the fractal time of dimension α, the mean-square variation of its velocity (over the real time t) is

$$\left\langle \delta \mathbf{w}^2(t) \right\rangle \propto t^{\alpha} \,. \tag{8.9}$$

The correlator

$$\mathcal{O}(t) \equiv -\frac{\left\langle \delta \mathbf{w}(-t)\, \delta \mathbf{w}(t) \right\rangle}{\left\langle \delta \mathbf{w}^2(t) \right\rangle} = 2^{\alpha - 1} - 1 \tag{8.10}$$

of past and future variations of the velocity $\mathbf{w}$ is defined by Eqn (4.4). It is necessary to distinguish persistent and antipersistent accelerations depending on the sign of the correlator: $\mathcal{O}(t) > 0$ and $1 < \alpha \leqslant 2$ for persistent processes, and $\mathcal{O}(t) < 0$ and $0 \leqslant \alpha < 1$ for antipersistent ones. The intermediate regime $\mathcal{O}(t) = 0$, $\alpha = 1$ corresponds to an uncorrelated, diffusive acceleration. We stress that fractal time accelerations are non-Markovian processes: $\mathcal{O}(t) \neq 0$ for $\alpha \neq 1$.

8.4 Fractional phase-space derivative

The fractional derivative $\nabla_{\mathbf{w}}^{2\beta}$ with respect to velocity in the right-hand side of Eqn (8.8) is determined through the Riesz–Weyl operator (4.5) in which the variable $\mathbf{r}$ should be substituted by $\mathbf{w}$. The improper integration in the Riesz–Weyl operator accounts for high-energy particles with velocities that can be substantially higher than the corresponding 'thermal' values. Levy statistics based on the notion of instant jumps ('flights') of particles from one spatial point to another is related to the Riesz–Weyl operator. Levy processes in the velocity space $\{\mathbf{w}\}$ can be treated as 'severe' accelerations when a particle 'instantly' (i.e., with a negligibly small inertia) receives a finite portion of kinetic energy due to the interaction with the turbulent field. Most probably, severe accelerations dominate at the stage of violent relaxation when intense energy exchange occurs between different parts of the system. An example can be particle acceleration in strong turbulent flows with Reynolds numbers $\mathcal{R}_* \gtrsim 10^3$ [66]. We emphasize that the particles participating in the acceleration processes are considered an inherent part of the turbulent ensemble.

8.5 Notes on the terminology

Following the terminology used in fractional dynamics, we say that all processes satisfying generalized equation (8.8) are strange accelerations [99]. Strange accelerations thus include both fractal-time accelerations (FTRWs) and Levy processes in the velocity space. In Eqn (8.9), fractal-time accelerations are a natural generalization of diffusive Fermi process (8.5), which is a particular case of the FTRW with $\alpha = 1$. We say that fractal-time accelerations are strange Fermi processes [99].

8.6 Towards the NESS: an intermediate state

We suppose that the system has passed the initial stage of violent relaxation and is in some intermediate nonequilibrium state gradually evolving towards the NESS (Fig. 14).

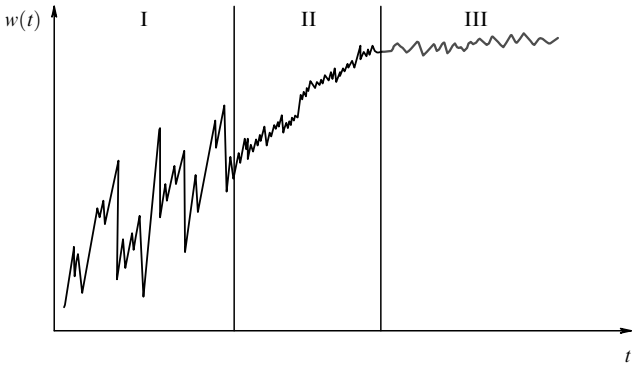

Figure 14. The consecutive stages of the transition of a dynamical system to a nonequilibrium (quasi)-stationary state. I — violent relaxation; II — intermediate state; III — the NESS limit.

Contrary to the violent relaxation, where the competition between particles for the position in the phase space occurs in the severe-acceleration duel, the intermediate state is characterized by a smoother energy redistribution due to the non-Markovian property and the dominance of multi-scale time correlations. In the intermediate state, however, turbulence does not yet represent an integral nonlinear ensemble that could be identified with the NESS concept, and the test-particle approximation suffices for the description of the acceleration dynamics. The corresponding kinetic equation for the function $\psi(t, \mathbf{w})$ is given by

$$\frac{\partial^\alpha \psi}{\partial t^\alpha} = \nabla_{\mathbf{w}}^2 \psi \,. \tag{8.11}$$

Equation (8.11) follows from Eqn (8.8) in the limit as $\beta \to 1$, implying that Levy processes in the medium can be disregarded. We note that Eqn (8.11) is nothing but the fractional diffusion equation in the velocity space, and strange Fermi accelerations are its physical realization.

To avoid unnecessary complications, we assume the turbulent medium isotropic. (Effects related to anisotropy can be caused, in particular, by an external large-scale magnetic field, for example, the intergalactic field if cosmic ray acceleration is considered). We have $\psi(t, \mathbf{w}) = \psi(t, w)$ and $\Delta_{\mathbf{w}} = \Delta_w$, where $w \equiv |\mathbf{w}|$. The radial part of the Laplacian Δ_w in the three-dimensional space $\{\mathbf{w}\} \sim E^3$ can be represented as

$$\Delta_w \psi \equiv \frac{1}{w^2} \frac{\partial}{\partial w} \left[w^2 \mathcal{D}_w \frac{\partial \psi}{\partial w} \right] . \tag{8.12}$$

The function $\mathcal{D}_w$ in Eqn (8.12) is to be considered a w-dependent turbulent transport coefficient in the velocity space.

8.7 Transport coefficient behavior

By its physical meaning, the coefficient $\mathcal{D}_w$ in Eqn (8.12) must satisfy the relations

$$\mathcal{D}_w = \frac{\langle \delta \mathbf{w}^2(t) \rangle}{t^\alpha} \sim \frac{[\delta \mathbf{w}(\tau)]^2}{\tau^\alpha} \,, \tag{8.13}$$

where $\tau \sim a/w$ is the elementary time step of the kinetic process; a defines the characteristic size of the turbulent field clots (for example, the diameter of magnetic clouds); $\delta \mathbf{w}(\tau) \sim g\tau$ is the variation of the particle velocity over time τ; and, finally, g describes the mean particle acceleration in the turbulent region. We note that the step τ enters Eqn (8.13) with the anomalous power α that coincides with the active-time fractal dimension [see Eqn (8.9)]; therefore, Eqn (8.13) is consistent with the fractional time derivative $\partial^\alpha / \partial t^\alpha$ on the left-hand side of Eqn (8.11). We also note that the variance $\langle \delta \mathbf{w}^2(t) \rangle \sim g^2 \tau^2 (t/\tau)^\alpha$ for $t \gg \tau$. Therefore,

$$\mathcal{D}_w \sim \frac{g^2 \tau^2}{\tau^\alpha} \sim \mathcal{K} w^{\alpha - 2} \,, \tag{8.14}$$

where the quantity $\mathcal{K} = \text{const}\,(w)$ is independent of w. In the Gaussian limit $\alpha \to 1$, the turbulent transport coefficient $\mathcal{D}_w$ is inversely proportional to the velocity w. This is because the time $\tau \sim a/w$ of the particle interaction with magnetic clouds continues to decrease as its kinetic energy $\mathcal{E} = w^2/2$ increases.

8.8 Generalized acceleration laws

Substituting turbulent transport coefficient (8.14) in fractional diffusion equation (8.11), we find the equation for the distribution function $\psi = \psi(t, w)$,

$$\frac{1}{\mathcal{K}} \frac{\partial^\alpha \psi}{\partial t^\alpha} = \frac{1}{w^2} \frac{\partial}{\partial w} \left[w^\alpha \frac{\partial \psi}{\partial w} \right] . \tag{8.15}$$

The general solution of Eqn (8.15) for arbitrary initial conditions can be expressed through Fox functions given in [100]. To study the acceleration dynamics, we use the method in Section 4. We first multiply both sides of Eqn (8.15) by $w^{4-\alpha}$ and integrate over the velocity space $\{\mathbf{w}\}$: $\int \mathrm{d}\mathbf{w} \equiv 4\pi \int_0^\infty w^2 \, \mathrm{d}w$. On the left-hand side of Eqn (8.15), we pull the integro-differentiation operation with respect to time outside the integrand and replace the partial derivative $\partial^\alpha / \partial t^\alpha$ by the total fractional time derivative $\mathrm{d}^\alpha / \mathrm{d}t^\alpha$. The integral over w that remains under the fractional differentiation then yields the ensemble average $\langle w^{4-\alpha} \rangle_\psi$. On the right-hand side of Eqn (8.15), we integrate by parts twice, taking normalization (8.7) into account; the result is given by the constant $3(4 - \alpha)$. We thus have

$$\frac{\mathrm{d}^\alpha}{\mathrm{d}t^\alpha} \langle w^{4-\alpha} \rangle_\psi = 3(4 - \alpha)\, \mathcal{K} \,. \tag{8.16}$$

Integrating Eqn (8.16), we find

$$\langle w^{4-\alpha} \rangle_\psi = \frac{3(4 - \alpha)}{\Gamma(\alpha + 1)} \, \mathcal{K} \times t^\alpha \,. \tag{8.17}$$

It is easy to see from Eqn (8.17) that the particle velocity increases on average as

$$\langle w \rangle_\psi \sim \text{const} \times t^\varsigma \quad (t \to \infty) \,, \tag{8.18}$$

$$\varsigma = \frac{\alpha}{4 - \alpha} \,. \tag{8.19}$$

Setting $\alpha = 1$ in Eqns (8.18) and (8.19), we arrive at the 'one-third law' for the ordinary Fermi acceleration [151]:

$$\langle w \rangle_\psi \sim \text{const} \times t^{1/3} \quad (t \to \infty) \,. \tag{8.20}$$

The 'one-third law' corresponds to Gaussian random process (8.6). Returning to Eqn (8.18), we obtain the particle kinetic energy ($\mathcal{E} \propto w^2$) as

$$\langle \mathcal{E} \rangle_\psi \sim \text{const} \times t^{2\varsigma} \quad (t \to \infty) \,. \tag{8.21}$$

Equation (8.19) implies that persistent processes ($1 < \alpha \leqslant 2$) correspond to $1/3 < \varsigma \leqslant 1$, while antipersistent ones ($0 \leqslant \alpha < 1$) to $0 \leqslant \varsigma < 1/3$. Persistent (antipersistent) acceleration processes occur more rapidly (slowly) compared to the standard Fermi process. In the limiting case where $\varsigma = 1$ ($\alpha = 2$), particles are accelerated along ballistic trajectories in the velocity space $\{\mathbf{w}\}$. The opposite limiting case $\varsigma = 0$ ($\alpha = 0$) corresponds to particles captured into isoenergetic orbits $w = \text{const}$. Strange Fermi processes ($0 \leqslant \varsigma \leqslant 1$) play an important role in the formation of the particle energy distribution in the earth's magnetotail plasma sheet [47, 99].

9. Nonlinear kinetic equation

9.1 Self-action of a turbulent field

We emphasize that the results obtained in Section 8 pertain to test particles and do not take account of the inverse effect of hot plasma on the turbulent field. The inverse effects, however, are inevitable as the system approaches the NESS and the ensemble of particles and fields evolves into an intimately interconnected 'community' (see Fig. 14). The effect can be treated as a self-interaction of the turbulent ensemble, which renders the system dynamics essentially nonlinear. The self-interaction is manifested in the magnetic field generation by charged particles participating in strange acceleration processes in the turbulent domain (Fig. 15). Because the field generation requires an energy feed, the self-interaction effects limit particle acceleration in the medium and somehow control the particle energy distribution.

To incorporate self-interaction effects, we add a sink term (s.t.) to the right-hand side of Eqn (8.8) to account for particles that lose their energy to field regeneration:

$$\frac{\partial^{\alpha}\psi}{\partial t^{\alpha}} = \nabla_{\mathbf{w}}^{2\beta}\psi + \text{s.t.} \tag{9.1}$$

In electrodynamical systems, the sink term is a quadratic functional of the currents induced in the medium,

$$\text{s.t.} = -\mathcal{G}_{\mu\nu} j^{\mu} j^{\nu} , \tag{9.2}$$

where j^{μ} ($\mu = 1, 2, 3$) are the covariant components of the current $\mathbf{j}$ depending on the velocity $\mathbf{w}$, and elements of $\mathcal{G}_{\mu\nu}$ are arranged into a nondegenerate symmetric 3×3 matrix such that the quadratic form s.t. is positive-definite. In Eqn (9.2), summation over repeated indices μ and ν is assumed. For isotropic systems, we have $\mathcal{G}_{\mu\nu} = 4\pi w^2 \mathcal{G} \delta_{\mu\nu}$, where the diagonal element $\mathcal{G}$ characterizes the intensity of self-action processes near the NESS, $4\pi w^2$ is the particle state density in three-dimensional velocity space $\{\mathbf{w}\}$, and $\delta_{\mu\nu}$ is the Kronecker symbol. Accordingly, formula (9.2) takes the form

$$\text{s.t.} = -4\pi w^2 \mathcal{G} j_{\mu} j^{\mu} . \tag{9.3}$$

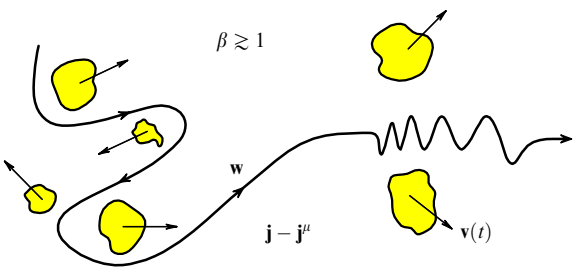

Figure 15. The self-action of a turbulent ensemble near the NESS. Particles participating in turbulent acceleration processes have to return a progressively large fraction of the gained energy in the form of 'taxes' for field reproduction.

Combining Eqns (9.1) and (9.3), we obtain the equation for the plasma particle velocity distribution $\psi = \psi(t, w)$

$$\frac{\partial^{\alpha}\psi}{\partial t^{\alpha}} = \nabla_{\mathbf{w}}^{2\beta}\psi - 4\pi w^2 \mathcal{G} j_{\mu} j^{\mu} . \tag{9.4}$$

We assume the system to be so close to the NESS that Levy flights in the velocity space (i.e., severe accelerations characteristic of the violent relaxation stage) can be neglected. Correspondingly, we set the order β of the phase-space differentiation in Eqn (9.4) equal to one. Next, by choosing an appropriate normalization of the interaction amplitude $\mathcal{G}$, we normalize the electric currents j_{μ} with respect to the motion of a single particle. Because the contraction $j_{\mu} j^{\mu}$ yields an invariant quantity, the scalar $\mathbf{j}^2$, we can use arbitrary curvilinear coordinates to calculate it. In particular, we can follow the acceleration of each particle along its trajectory and detect the instant when it gains a given velocity w (Fig. 15). We also assume that elementary accelerations (scatterings by clots) are so numerous that the vector $\mathbf{w}$ has time to 'scan' the entire space $\{\mathbf{w}\}$ before its length changes noticeably. By averaging over the directions of $\mathbf{w}$, we express the obtained current density $j = |\mathbf{j}|$ through the self-consistent distribution function $\psi = \psi(t, w)$ as

$$j(t, w) = 4\pi e \int_{V}^{w} u^3 \psi(t, u)\, \mathrm{d}u . \tag{9.5}$$

We note that the self-consistency effects become significant only after the violent relaxation period is over, when the system is 'tightly captured' by correlations. The integration in Eqn (9.5) is performed from $u_{\min} \sim V$ to $u_{\max} \sim w$, where $w \gg V$, and V has the meaning of the characteristic group velocity of turbulent magnetic field clots near the NESS. Because the variable u satisfies the condition $V \lesssim u \lesssim w$, Eqn (9.3) takes field generation processes into account until an initially cold ($u \sim V$) particle reaches a given velocity $w \gg V$ in the course of the turbulent acceleration.

9.2 Kinetic equation for systems with self-interaction

Combining Eqn (8.15) with (9.4) and (9.5), we find [99]

$$\frac{1}{\mathcal{K}} \frac{\partial^{\alpha}\psi}{\partial t^{\alpha}} = \frac{1}{w^2} \frac{\partial}{\partial w} \left[w^{\alpha} \frac{\partial \psi}{\partial w} \right] - \mathcal{J} w^2 \left[\int_{V}^{w} u^3 \psi \, \mathrm{d}u \right]^2 , \tag{9.6}$$

where $\mathcal{J} = 64\pi^3 e^2 \mathcal{G}/\mathcal{K} = \text{const}$. Together with Riemann–Liouville operator (4.2), Eqn (9.6) forms a complete self-consistent system of integro-differential kinetic equations for turbulent self-interacting electrodynamical systems near the NESS.

Equation (9.6) describes a broad range of strange dynamical processes in nonlinear systems with strong turbulence. We are mainly interested in the stationary solutions of kinetic equation (9.6) that do not explicitly depend on time: $\psi = \psi(w)$.

An important point is that fractional derivative (4.2) of the stationary distribution function $\psi = \psi(w)$ does not vanish

automatically. We have

$$\frac{\partial^{\alpha}\psi}{\partial t^{\alpha}} = \frac{\psi}{\Gamma(1-\alpha)} \times t^{-\alpha}. \tag{9.7}$$

Equation (9.7) corresponds to the so-called Mittag-Leffler relaxation characteristic of the behavior of nonequilibrium dynamical systems with multi-scale time correlations [153]. In the context of model (9.6), the Mittag-Leffler process is responsible for a gradual transition of the system from an intermediate nonequilibrium state to properly NESS (see Fig. 14). The sought stationary solution $\psi = \psi(w)$ can be considered as a limiting ($t \to \infty$) particle velocity distribution appearing on time scales so long that the residual relaxation phenomena in the system can be neglected. The stationary distribution function $\psi = \psi(w)$ with $\alpha > 0$ satisfies the integro-differential equation

$$\frac{1}{w^2}\,\frac{\partial}{\partial w}\left[w^{\alpha}\,\frac{\partial\psi}{\partial w}\right] = \mathcal{J} w^2 \left[\int_V^w u^3 \psi\,\mathrm{d}u\right]^2. \tag{9.8}$$

9.3 Self-similar distribution function

In a self-consistent regime, fractal-time accelerations produce a self-similar particle velocity distribution that is the scale-invariant under the phase variable transformations

$$\psi(w) \propto w^{-\varrho} \tag{9.9}$$

with the exponent $\varrho = \mathrm{const}\,(w)$ for $w \gg V$. Substituting distribution (9.9) in kinetic equation (9.8), we arrive at the relation between the parameter ϱ and the active-time fractal dimension $\alpha > 0$,

$$\varrho = 14 - \alpha. \tag{9.10}$$

Correspondingly, the particle energy distribution has the power-law form

$$\psi(\mathcal{E}) \propto \mathcal{E}^{-\eta}, \tag{9.11}$$

$$\eta = \frac{\varrho}{2} = 7 - \frac{\alpha}{2}. \tag{9.12}$$

Dependence (9.9) with exponent (9.10) describes the plasma particle velocity distribution in the marginal nonequilibrium (quasi)-stationary state of the turbulent ensemble ($t \to \infty$). Because the particle velocities $w \gg V$, solutions (9.9) and (9.11) correspond to high-energy nonthermal tails in Eqns (8.1) and (8.2).

9.4 Constraints on the parameter η

Equation (9.12) suggests that persistent processes ($1 < \alpha \leqslant 2$) correspond to values $6 \leqslant \eta < 6.5$, while antipersistent ones correspond to values $6.5 < \eta < 7$. The diffusion Fermi acceleration in (8.6) is recovered at $\eta = 6.5$. Therefore, the parameter η for turbulent systems near the NESS changes within the limits [99, 130]

$$6 \leqslant \eta < 7, \tag{9.13}$$

where the restriction $\alpha > 0$ on the active-time fractal dimension has been used. Nonthermal distribution (9.11) contains considerable excess energy compared to the Gibbs distribution in (8.4). The excess energy is due to (strange) acceleration processes accompanying the system relaxation to the NESS. Because the particle acceleration is ultimately governed by the inherent dynamics of the turbulent ensemble, formation of superthermal distributions (9.11) must be accompanied by low-frequency ($f \lesssim V/\xi$) noises with characteristic power-law energy density spectra (5.17). The closer the system is to the NESS, the lighter the noise is at low frequencies. The dominance of rose colors indicates the system stabilization in the limiting NESS corresponding to self-organized criticality (5.27). The noise color at low frequencies can therefore be considered an indicator of how close the system is to SOC, or of how singular it is [130].

Most probably, the dynamical processes described above (see Sections 8 and 9) underlie the heating of the cool plasma entering the earth's magnetotail plasma layer from the solar wind [47, 130]. Indeed, the characteristic ion temperatures in the plasma layer $T_{\mathrm{PL}} \sim 1-5$ keV and in the solar wind after deceleration and initial heating at the near-earth bow-shock $T_{\mathrm{SW}} \sim 10^2$ keV differ by a factor of 10 – 50. Such a big difference can be explained only by the 'inherent' acceleration mechanisms operating directly inside the plasma sheet. The cool plasma entering the magnetosphere turns out to be in a sort of microwave oven that 'prepares' a self-consistent turbulent 'cake'.

9.5 Kappa-distributions

Nonthermal distributions $\psi = \psi(\mathcal{E})$ with power-law tails (8.2) and (9.11) at high energies $\mathcal{E} \gg T$ can in many cases be approximated by the so-called kappa-functions [149]. Typically, kappa-functions encompass distributions of the form

$$\psi(\mathcal{E}) \sim A\left[1 + \frac{\mathcal{E}/T}{\varkappa + 1}\right]^{-(\varkappa+1)}, \tag{9.14}$$

where $\varkappa \geqslant 0$ is a real-valued nonnegative parameter and A has the meaning of a normalization constant. Kappa-functions are a convenient analytic interpolation from Gibbs distribution (8.4) at low energies $\mathcal{E} \lesssim T$ to nonthermal power-law distributions (8.2) and (9.11) for $\mathcal{E} \gg T$. In the limit as $\varkappa \to \infty$, kappa-functions reduce to the Gibbs distribution.

Kappa-distributions were obtained in studies of nonequilibrium plasma interacting with a nonthermal background radiation [154]. Kappa-distributions may also arise in particle scattering on plasma oscillations, for example, on whistlers [155]. Kappa-functions are related to a number of symmetries of the Maxwell – Vlasov system of equations [156]. The existence of such symmetries follows from the results of Lie group classification [156]. Applications of kappa-functions to space plasma turbulence were discussed in [149, 157 – 159]. It can be shown [144] that kappa-functions are canonical distributions in the generalized Darozi – Tsallis statistics (in the same way that the Gibbs distribution is canonical in the Boltzmann statistics).

Comparing Eqn (9.14) with Eqns (8.2) and (9.11) in the nonthermal region $\mathcal{E} \gg T$, we obtain a relation between the parameters η, ϱ, and $\varkappa$,

$$\eta = \frac{\varrho}{2} = \varkappa + 1. \tag{9.15}$$

Combining Eqns (9.13) and (9.15), we find the typical values of the parameter $\varkappa$ for turbulent magnetoplasmic systems near the NESS,

$$5 \leqslant \varkappa < 6. \tag{9.16}$$

9.6 Energetic particle populations in the earth's magnetosphere

In cosmic electrodynamics, kappa-functions emerge, in particular, in describing particles 'populating' the earth's magnetotail plasma sheet [149]. The parameters of the corresponding kappa-distribution were first obtained in magnetic field and plasma experiments with the ISEE-3 satellite [149]. As noted in [149, p. 13409], "for both ions and electrons, $\varkappa$ is typically in the range 4–8, with a most probable value between 5 and 6." Observational data thus fully confirm inequality (9.16) inferred from Eqn (9.6). Therefore, the results in [149], which are well known in the geophysical literature, mirror the fundamental properties of turbulent fields and plasma forming a self-consistent nonlinear thermodynamic system far from the thermal equilibrium. We emphasize that the earth's magnetosphere represents a unique natural laboratory offering broad perspective for thorough studies of strange kinetic processes in turbulent media.

9.7 Violent relaxation and cosmic ray spectra

It is interesting to compare the value of the exponent η from interval (9.13) with the slope of the plasma particle energy distribution function at the violent relaxation stage, when the energy spectrum $\psi(\mathcal{E})$ is mainly formed by severe accelerations corresponding to Levy processes in the turbulent domain. The acceleration dynamics obey kinetic equation (8.8) with the integer ($\alpha \to 1$) time derivative $\partial\psi/\partial t$ on the left-hand side; on the right-hand side, the Riesz–Weyl operator $\nabla_{\mathbf{w}}^{2\beta}$ contains an integro-differentiation operation of a fractional order $1 \leqslant 2\beta < 2$. The turbulent transport coefficient $\mathcal{D}_w$ at the violent relaxation stage is different from Eqn (8.13) by a fractional power of $\delta\mathbf{w}$ and an integer power of t:

$$\mathcal{D}_w = \frac{\langle \delta\mathbf{w}^{2\beta}(t)\rangle}{t} \sim \frac{[\delta\mathbf{w}(\tau)]^{2\beta}}{\tau}\,. \tag{9.17}$$

Neglecting FTRW-like processes ($\alpha \to 1$) compared to severe accelerations ($1 \leqslant 2\beta < 2$) runs counter to the conditions formulated in Section 8 for the intermediate state: $\beta \to 1$ and $0 < \alpha \leqslant 2$. However, in both cases, we can consider only test particles. Taking the relations $\tau \sim a/w$ and $\delta\mathbf{w}(\tau) \sim g\tau$ for elementary acceleration processes into account, instead of (8.14), we obtain

$$\mathcal{D}_w \sim \frac{g^{2\beta}\tau^{2\beta}}{\tau} \sim \mathcal{K} w^{1-2\beta}\,. \tag{9.18}$$

Correspondingly, the radial part $\nabla_w^{2\beta}$ of the Riesz–Weyl operator $\nabla_{\mathbf{w}}^{2\beta}$ in three-dimensional ($\mathrm{d}\mathbf{w} = 4\pi w^2\,\mathrm{d}w$) velocity space $\{\mathbf{w}\} \sim E^3$ takes the form

$$\nabla_w^{2\beta} = \frac{1}{w^2}\,\frac{\partial^\beta}{\partial w^\beta}\left[w^2\mathcal{D}_w\frac{\partial^\beta}{\partial w^\beta}\right] = \frac{\mathcal{K}}{w^2}\,\frac{\partial^\beta}{\partial w^\beta}\left[w^{3-2\beta}\,\frac{\partial^\beta}{\partial w^\beta}\right]. \tag{9.19}$$

Representation (9.17) is analogous to Eqn (4.9) up to the changes $r \to w$ and $d_s \to n = 3$ and absorption of the transport coefficient into the operator $\nabla_w^{2\beta}$. Assuming the order of differentiation $\beta \to 1$ in (9.17), we recover Laplacian (8.12). The derivation of the distribution $\psi(t, w)$ from kinetic equation (8.8) with fractional Laplacian (9.17) is quite similar to the well-known methods used in Levy statistics [92]. As $\alpha \to 1$, in the limit of large velocities $w \gg V$, it follows from equations (8.8) and (9.17) that

$$\psi(t, w) \propto \mathcal{K}t \times w^{-\varrho}\,, \tag{9.20}$$

$$\varrho = 2 + 4\beta\,, \tag{9.21}$$

where natural normalization condition (8.7) and definition (4.10) of the radial derivative $\partial^\beta/\partial w^\beta$ in the Riemann–Liouville sense are taken into account. The fact that the probability density $\psi(t, w)$ in Eqn (9.18) explicitly depends on time is due to the essentially nonequilibrium character of dynamical processes occurring at the violent relaxation stage. As follows from Eqns (9.18) and (9.19), the energy spectrum of the system follows Eqn (9.11), while the exponent

$$\eta = 1 + 2\beta \tag{9.22}$$

then changes from two (at $2\beta = 1$) to three (at $2\beta \to 2$) with a 'characteristic' value $\eta \sim 2.5$. The interval $2 \leqslant \eta < 3$ encompasses the observed cosmic ray spectra in a wide energy range [150]. The value $\eta \sim 2.5$ was derived earlier from the shock particle acceleration model [150]. Some alternative models (including diffusive acceleration) are addressed in [160]. Relation (9.20) for the power-law exponent, which follows from kinetic equation (8.8), can be considered a natural generalization of the partial acceleration mechanisms [150, 160] in the light of fundamental physical processes inherent in nonequilibrium dynamical systems with strong turbulence.

10. Fractal aggregates and growth phenomena

Until now, in studying the walks of clots in the configuration space, we have avoided considering their interaction in direct collisions. In dissipative systems, collisions of clots of the same polarity can result in their conglomeration. If the collision frequency exceeds the inverse dissipation time, the primary (seed) conglomerates have time to grow into large-scale clusters with a large number of elements [79, 161]. The formation and growth of clusters is due to the aggregation of clots from a turbulent 'colloid' of particles and fields. This process can occur under various conditions, which to some degree affect the aggregate fine-scale structure [79]. The characteristic feature of clusters appearing during aggregation and growth is their low (fractal) dimension depending on both the geometry of walking and the interaction details [9, 79, 162, 163]. The physics of fractal aggregates was discussed in detail in reviews [24, 162] and monographs [7–9, 163].

It is plausible that aggregation and growth phenomena underlie the formation of large-scale magnetic fields in space plasma [79]. Examples include the formation of sun spots [161] and groups of spots [164] in the solar photosphere, as well as inelastic interaction of magnetic clouds in the solar wind [128] and development of a large-scale fractal structure in the interplanetary magnetic field [165]. Cosmological applications (which go far beyond the scope of the present review), in particular, include the model of the intergalactic magnetic field origin due to spontaneous polymerization of low-frequency thermal fluctuations at the time before the recombination epoch in the universe [166–169].

10.1 Fractal clusters in the solar photosphere

Sun spot formation in the solar photosphere is due to aggregation of a large number of intense flux tubes with one

polarity on seed concentrations of the magnetic flux — the so-called pores, appearing at the supergranulation cell junction under the action of small-scale convective flows that pushes one-sign poles toward each other [170, 171]. The central parts of a spot, which form its umbra, are dense clusters of tubes compressed from all sides by forces of mutual attraction (more precisely, by the attraction forces between longitudinal currents that form the spot poloidal magnetic field). The attraction between longitudinal currents is counterbalanced by the magnetic field elasticity in tubes, which prevents the electromagnetic collapse of the system. The magnetic field strength at the spot center reaches values of the order $(3-4)\times 10^3$ E. The umbra of a developed spot is surrounded by the so-called penumbra, also consisting of the same halo tubes and looking like a huge actinia with open tentacles. The sun spot structure is schematically shown in Fig. 16.

The complex geometry of the halo geometry can be understood in the context of the fractal sun spot model [161] assuming the balance of the aggregate bulk energy stored in the condensed flux tubes (due to longitudinal currents) and the surface energy of the fractal boundary, which has a positive tension (due to the poloidal field effect) and whose contribution to the free energy of the system is comparable to the bulk contribution. The extremum (minimum) of the free energy corresponds to the Hausdorff dimension of the halo [79]

$$d_{\rm f}=\frac{4}{3}+\frac{1}{3}\,\frac{\ln\left(3/8\pi\Delta^2\ln 2\right)}{\ln(\xi/a)}\,, \tag{10.1}$$

where a is the force tube cross-size at the photosphere level ($\sim 10^2$ km), ξ is the radial size of the spot ($\sim 3\times 10^4$ km), and the quantity Δ depends on the parameters of the plasma distribution function. Hausdorff dimension (10.1) describes the distribution of intense force tubes across the spot disk in the penumbra. We note that for developed spots ($\ln(\xi/a)\gg 1$), the Hausdorff dimension $d_{\rm f}$ is close to 4/3:

$$d_{\rm f}\approx\frac{4}{3}\,. \tag{10.2}$$

The fractal model is appealing because it leads to realistic times for spot formation (~ 10 days) and life span ($\sim 2-3$ months) [172]. Interestingly, the decay of a spot can be interpreted as a second-order phase transition reminiscent of the transition through the Curie point in ferromagnets [164]. Experimental studies of fractal structures in the solar photosphere are discussed in monograph [117].

10.2 Color noises in the solar wind

The solar wind — a permanent plasma flow of solar origin that fills the solar system up to heliocentric distances $R\sim 10^2$ a.u. — is formed in the supersonic expansion of the solar corona into interplanetary space [170, 173]. With a temperature of millions degrees, the dynamical pressure of the corona gas is so high that it leads to acceleration of upper layers up to velocities of the order of $u\sim 300-700$ km s^{-1} outwards from the sun [170]. The expansion dynamics depend on a number of factors including, for example, the magnetic field topology in the corona. The solar wind coming from regions with predominantly radial magnetic field components is accelerated more uniformly and quietly, reaching velocities about $u\sim 600-700$ km s^{-1}. In contrast, the wind that touches the tangential magnetic field is more irregular and its velocities do not exceed $u\sim 350$ km s^{-1}.

As a rule, the fast solar wind is formed over the coronal holes, while the slow one is formed above the regions with complex field configurations, including coronal loops. Large-scale variations of the solar wind cased by inhomogeneous corona expansion along fast and slow streams are considered by a rest-frame observer as turbulence with parameters depending on the heliocentric distance R.

One of the most important properties of solar wind turbulence is the presence of color noises with power-law spectra like (5.17). The color of the noise, as a rule, depends not only on the frequency range f but also on the heliocentric distance R. Indeed, according to data from satellites IMP-8 and ISEE-3, the spectrum of large-scale variations of the interplanetary magnetic field $B(t)$ near the earth's orbit (i.e., at $R\sim 1$ a.u.) has the form $P(f)\sim f^{-\varpi}$ at $f\gtrsim 3\times 10^{-6}$ Hz, with the exponent ϖ changing upon passing the frequency $f_*\sim 3\times 10^{-5}$ Hz (Fig. 17). At the lowest frequencies $f\lesssim f_*$, the exponent is $\varpi=1.92\pm 0.06$ [174], which corresponds to brown noise (6.7). In contrast, at high frequencies $f\gtrsim f_*$, the value of ϖ is much less than two and is close to $\varpi\approx 5/3$ [174, 175]. Power-like spectra with $\varpi\approx 5/3$ are intermediate between the rose and brown noises and their appearance is in many cases associated (sometimes, inappropriately) with a

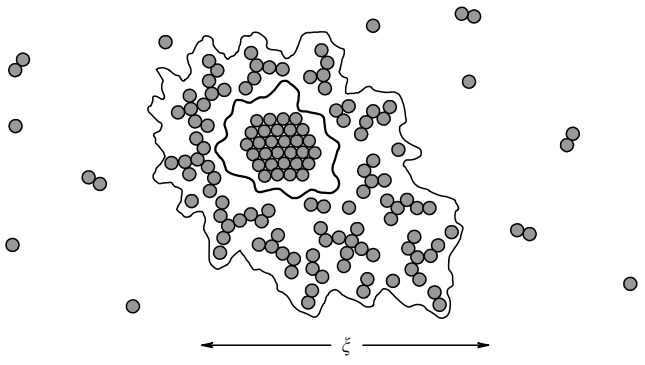

Figure 16. The structure of a sun spot. The umbra, which is the dense conglomeration of intense flux tubes with the same polarity, and the penumbra forming an extended fractal halo around the central magnetic 'core', are shown schematically. Sun spot growth is due to aggregation of intense force tubes precipitating on the outer boundary of the halo.

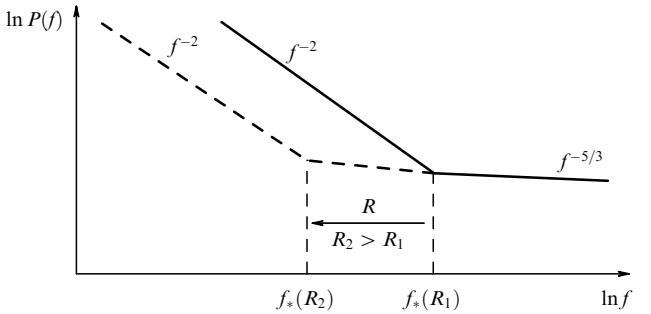

Figure 17. Color noises in the solar wind. The brown noise reminiscent of the Gaussian time series spectrum $\mathcal{I}_{1/2}(t)$ dominates at low frequencies. The lightening of noises at higher frequencies is due to self-organization processes encompassing progressively growing space – time scales as turbulent magnetic field clots move away from the sun. Correspondingly, the kink in the turbulence spectrum undergoes a 'brown shift', i.e., moves from 'light' to 'dark' frequencies as the heliocentric distance R increases.

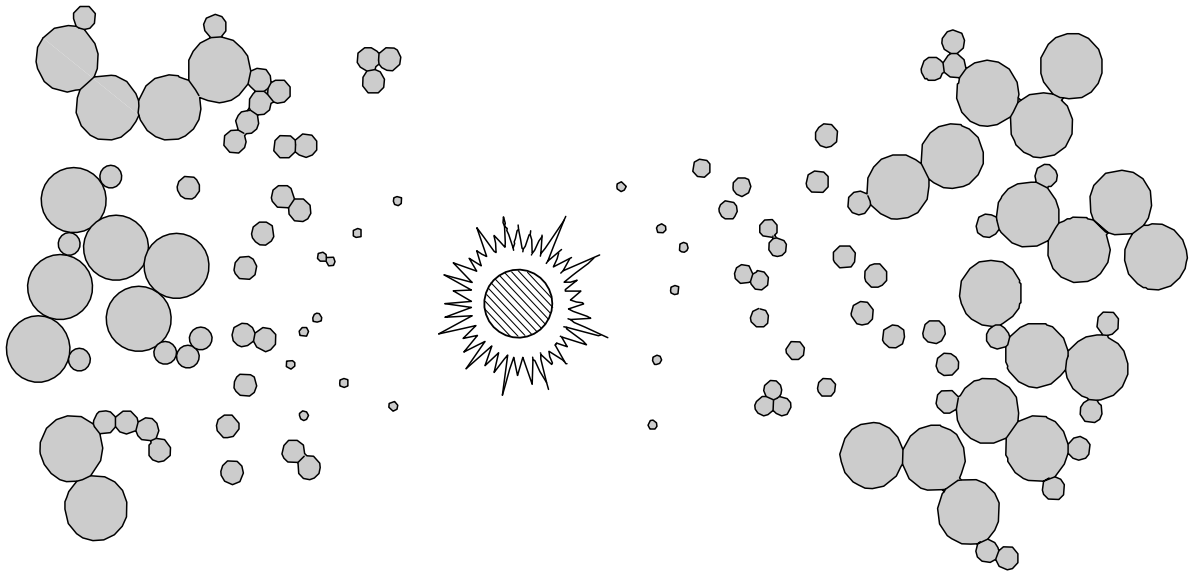

Figure 18. The aggregation of intense flux tubes of the interplanetary magnetic field. The inflation of tubes is due to the dynamic pressure drop in the solar wind outflowing from the corona.

developed hydrodynamic turbulence in the Kolmogorov theory K41 [18]. As R increases, the break near $f \sim f_*$ shifts towards low frequencies and the 'Kolmogorov' spectrum $P(f) \sim f^{-5/3}$ holds over a wider frequency range (see Fig. 17). According to data obtained by Voyager-2 at heliocentric distances $R \sim 8.5$ a.u., the power-law exponent ϖ of the interplanetary magnetic field fluctuations is $\varpi \approx 5/3$ in a much wider frequency range $3 \times 10^{-6} \lesssim f \lesssim 5 \times 10^{-2}$ Hz [69]. It is essential that the time series representing direct measurements of turbulent fields and plasma in the solar wind have the property of being statistically self-affine at the same frequencies where color noises are found [68, 69, 174, 176–178]. The statistical self-affinity property for interplanetary magnetic field fluctuations $B(t)$ near the earth ($R \sim 1$ a.u.) can be illustrated by the time series [54] shown in Fig. 2b.

The self-affine character of large-scale variations in the solar wind, which determines the color of the noise at the corresponding frequencies, can be understood in the context of the structural model suggested in [128, 129, 165]. According to this model, the interplanetary magnetic field is organized into elementary clots, intense force tubes, which are frozen into hot coronal plasma flows (Fig. 18). With increasing distance from the sun, the clots inflate and concentrate in clusters. The inflation is due to a decrease in the dynamic pressure in the solar wind at the spherically symmetric expansion of the corona. The clusters result from aggregation processes at the stage where tubes expand until they touch each other. For the initial and boundary conditions in the corona, the cluster formation occurs at heliocentric distances from ~ 0.05 to ~ 90 a.u. In the expanding reference frame frozen into solar wind streams, field clusterization is similar to sun spot formation in the solar photosphere. By analogy with the halo model, we can say that interplanetary magnetic field clusters have a fractal structure and their Hausdorff dimension d_f is determined by Eqn (10.1), where the ratio ξ/a depends on the heliocentric distance R in general. Due to aggregation of the growing number of tubes, the correlation length ξ continuously increases with R. The second term on the right-hand side of Eqn (10.1) then tends to zero and the fractal geometry of clusters evolves towards universal distribution with the Hausdorff dimension $d_f \approx 4/3$ in agreement with Eqn (10.2). The convection of the fractal distribution with solar wind fluxes is seen by the observer at rest as large-scale variations of the interplanetary magnetic field; the spectrum of variations is the power-law $P(f) \sim f^{-\varpi}$ with the exponent $\varpi = 2d_f - 1$. The situation is quite analogous to the appearance of color noises in the earth's magnetotail due to the convection of plasma and fields along the lobes (see Section 6). From Eqns (5.31) and (10.2), we find

$$\varpi = 2d_f - 1 \approx \frac{5}{3}\,, \tag{10.3}$$

$$P(f) \sim f^{-5/3}\,. \tag{10.4}$$

By its form, spectrum (10.4) coincides with the K41 spectrum of the homogeneous isotropic hydrodynamic turbulence in the Kolmogorov theory [18]. However, this spectrum has a qualitatively different nature: turbulent structures fill not the entire embedding space (as in the K41 theory) but only a low-dimensional subspace subjected to a stationary convection. The frequency f in Eqn (10.4) is limited from below by the inverse time of the cluster flight past the (terrestrial) rest-frame observer,

$$f \gtrsim f_* \sim \frac{u}{\xi}\,, \tag{10.5}$$

where u is the radial solar wind velocity and $\xi = \xi(R)$ represents the linear size of the cluster depending on the heliocentric distance. Near the earth's orbit ($R \sim 1$ a.u.), $\xi \sim 1 \times 10^7$ km, and hence $f_* \sim 3 \times 10^{-5}$ Hz for the slow wind [165].

At lower frequencies $f \lesssim f_*$, the spectrum of large-scale fluctuations $P(f)$ is determined by the spatial cluster distribution in the solar wind streams; this distribution is not distorted by aggregation effects and bears imprint of processes occurring in the lower atmosphere of the Sun. In the first approximation, the spatial distribution of clusters in the solar wind can be related to the fractal structure (confirmed by high-resolution magnetograms [179]) of convective flows in the solar photosphere that 'shuffle' the roots of the tubes in a random manner (Fig. 19). The hydrodynamic description of

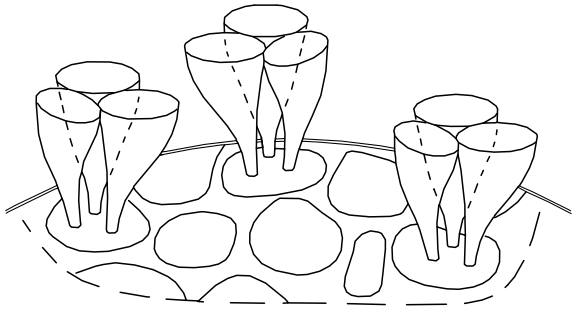

Figure 19. The roots of intense flux tubes are continuously shuffled by multi-scale convective flows forming hierarchical fractal structures in the solar photosphere.

turbulent convection can be done in the context of so-called 'β-models' [18]. Applying these processes to the solar photosphere results in the following estimate of the Hausdorff dimension of the spatial distribution of clusters across the wind [129]:

$$d_{\mathrm{f}} \approx \frac{3}{2}\,. \tag{10.6}$$

As follows from Eqn (5.31), convection of β-distribution (10.6) gives rise to the brown noise $P(f) \sim f^{-2}$ at frequencies $f \lesssim f_*$.

Summarizing the results in (10.2) and (10.6), we note that a large-scale structure of the interplanetary magnetic field is bifractal. Bifractal means a fractal distribution with the elements being fractal sets themselves. We note that the dimension of elements and their support are different in the general case. The bifractal structure of the interplanetary magnetic field is schematically shown in Fig. 20. A detailed comparison of the bifractal model with observations can be found in original papers [54, 128, 129, 165]. Direct experimental evidences for the existence of hierarchies from magnetic field tubes in the heliospheric plasma layer are obtained in [180, 181].

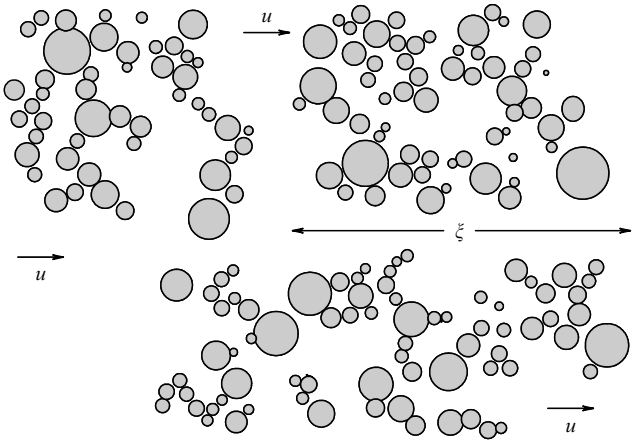

Figure 20. The bifractal structure of solar wind. The interplanetary magnetic field concentrates in clusters with the Hausdorff dimension close to $d_{\mathrm{f}} \approx 4/3$. This value can be explained by the aggregation of a large number of intense flux tubes. Clusters separated by a distance not less than ξ (for a given R) do not take part in the aggregation and their space distribution bears imprint of processes occurring in the lower layers of the solar atmosphere. The corresponding Hausdorff dimension d_{f} can be calculated using 'β-models': $d_{\mathrm{f}} \approx 3/2$.

11. Fracton excitations and the fractional parabolic equation

11.1 Fracton excitations in fractal structures

Along with FTRW processes, whose behavior is not restricted in space, fractons form an important class of dynamical eigendegrees of freedom consistent with the fractal geometry of the system [38]. Fractons are the localized (in accordance with Anderson's definition [182]) (quasi)-acoustic excitations corresponding to vibrations of fractal blobs. Examples are collective harmonic [$\sim \exp(\mathrm{i}\omega t)$] oscillations of turbulent magnetic field clots around some common equilibrium position (Fig. 21). Fracton modes correspond to the wavelength λ in the self-similarity range $a \lesssim \lambda \lesssim \xi$. In the harmonic approximation, fracton states have an infinite lifetime [183]. However, running excitations (phonons) with lengths from the self-similarity interval suffer strong scattering on spatial inhomogeneities caused by the fractal geometry of the system. The lifetime of phonon states is then of the order of the inverse wave frequency, $1/\omega$. This excludes phonons from vibrational eigenmodes of the fractal structure [183]. We note that the localization lengths of fracton modes substantially exceed the phonon scattering length in fractal media [183, 184]. Fractons with wavelengths $\lambda \gtrsim \xi$ are transformed into low-frequency phonons for which the fractal becomes transparent. Essentially, the fracton branch replaces the ordinary acoustic oscillations in passing from regular geometry to fractal distributions.

The statistics of fracton excitations have been discussed in detail in both original papers [38, 183, 185] and reviews [37, 186]. The direct observation of fracton modes in real physical systems is described in [184, 187]. The fracton mechanism of the Cooper pair formation in superconducting organic polymers [such as poly-(3-hexylthiophene) (P3HT)] is suggested in [43]. The 'relevance' of fractons to high-temperature superconductivity in ceramic compounds based on copper oxide is shown in [143, 103]. Nonlinear fracton effects are considered in [53, 54]; in particular, these effects include the fracton mode self-focusing and stabilization of an instability relative to the self-focusing due to diffraction smearing of the

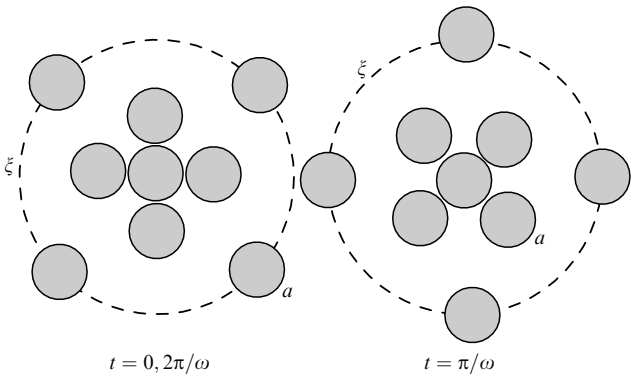

Figure 21. Fractons are vibrations of fractal blobs. Examples are collective harmonic oscillations of turbulent magnetic field clots around some common equilibrium point. Shown are the states of the clots separated by the oscillation half-period, $\Delta t = \pi/\omega$.

fracton wave function. The self-squeezing phenomenon is the key point in understanding the fluctuation spectra of the turbulent solar wind at intermediate frequencies [53].

11.2 Nonlinear dispersion relation

A distinctive feature of fracton excitations is the nonlinear dispersion relation having the power-law form [37]

$$\omega = \Lambda q^{\sigma}\,, \tag{11.1}$$

where the exponent σ depends on the connectivity index of the fractal structure [43],

$$\sigma = \frac{2+\theta}{2}\,, \tag{11.2}$$

and the wave vector q changes from $q_{\min} \sim 2\pi/\xi$ to $q_{\max} \sim 2\pi/a$. We note that the value of σ coincides with the parameter d_θ in Eqn (2.4),

$$\sigma = d_\theta\,. \tag{11.3}$$

The quantity d_θ has the meaning of the minimum of the Hausdorff dimensions of geodesic lines lying on the fractal set. This is a manifestation of the Fermat principle applied to fracton modes. The coefficient

$$\Lambda \sim c_* \times \left(\frac{\xi}{2\pi}\right)^{\theta/2} \tag{11.4}$$

defines the fracton phase velocity

$$c_\sigma(q) \sim c_* \times \left(\frac{q\xi}{2\pi}\right)^{\theta/2} \tag{11.5}$$

as a function of the wave vector q. The phase velocity c_σ is limited from above by the value

$$c_{\sigma\max} \sim c_* \times \left(\frac{\xi}{a}\right)^{\theta/2}. \tag{11.6}$$

Equations (11.5) and (11.6) imply that $c_\sigma \to c_*$ as $\theta \to 0$. The value of c_* is the phase velocity in low-frequency acoustic (phonon) oscillations and is independent of q. The dispersion relation for phonons is a particular case of Eqn (11.1) at $\theta = 0$, namely, $\omega = c_* q$. The low-frequency phonon branch satisfies the condition $\omega \lesssim \omega_{\min}$, where $\omega_{\min} \sim c_* q_{\min} \sim 2\pi c_*/\xi$. In contrast, fracton excitations correspond to the frequencies

$$\omega_{\min} \lesssim \omega \lesssim \omega_{\min} \times \left(\frac{\xi}{a}\right)^{\sigma}. \tag{11.7}$$

11.3 Spectral state density

The fracton state density has a power-law dependence on frequency [185]

$$D_{\rm fr}(\omega) \propto \omega^{d_{\rm s}-1}\,, \tag{11.8}$$

where $d_{\rm s} = 2d_{\rm f}/(2+\theta) = d_{\rm f}/\sigma$ is the spectral dimension of the ensemble — the same topological parameter that appears in describing transport processes on self-similar fractal structures (see Section 3). Interestingly, the term spectral dimension originates exactly from the power-law exponent on the right-hand side of Eqn (11.9) . Dependence (11.8) agrees with the physical meaning of $d_{\rm s}$ as an effective fractional number of the degrees of freedom in fractal sets [23]. Close to the percolation threshold ($d_{\rm s} = \mathcal{C} \approx 1.327\ldots \sim 4/3$), i.e., in the state corresponding to the NESS limit, we use Eqns (2.7) and (2.10) to obtain

$$D_{\rm fr}(\omega) \propto \omega^{\mathcal{C}-1} \sim \omega^{1/3}\,, \tag{11.9}$$

where $\mathcal{C}$ is the percolation constant. In the Euclidean limit $d_{\rm s} \to n$, dependence (11.8) transforms into the phonon state density [147]

$$D_{\rm ph}(\omega) \propto \omega^{n-1}\,. \tag{11.10}$$

Close to the percolation threshold, the fracton states ($d_{\rm s} = \mathcal{C} \approx 1.327\ldots \sim 4/3$) are significantly denser than the phonon ones ($d_{\rm s} = n \geqslant 2$),

$$D_{\rm fr}(\omega) \gg D_{\rm ph}(\omega)\,, \tag{11.11}$$

where $\omega \lesssim \omega_{\min} \times (\xi/a)^{\sigma}$ in accordance with condition (11.7). The dominance of the fracton modes over the phonon ones at $T \lesssim \hbar\omega_{\min} \times (\xi/a)^{\sigma}$ is likely to underlie the superconductivity phenomenon in materials with disordered microscopic structure [43, 103].

11.4 Fractional kinetic equation for fracton excitations

We now calculate the fracton wave function $\Psi(t,x)$ in a state with frequency ω and wave vector q. In the harmonic approximation, we have $\Psi(t,x) = \psi(x)\exp(\mathrm{i}\omega t)$, where the coordinate x is along the vector q. As usual [see Eqns (3.15) and (8.7)], we assume that the functions $\Psi(t,x)$ and $\psi(x)$ satisfy the natural normalization condition

$$\int_{-\infty}^{+\infty} |\Psi(t,x)|^2\,\mathrm{d}x = \int_{-\infty}^{+\infty} |\psi(x)|^2\,\mathrm{d}x = 1\,. \tag{11.12}$$

Replacing ω and q with the respective differentiation operators $\mathrm{i}\partial/\partial t$ and $-\mathrm{i}\partial/\partial x$, we pass from dispersion relation (11.1) to the fractional kinetic equation

$$\frac{\mathrm{i}\partial\Psi(t,x)}{\partial t} = \mathrm{i}^{-\sigma}\Lambda\nabla_x^{\sigma}\Psi(t,x) \tag{11.13}$$

with the Riesz–Weyl operator ∇_x^{σ} in the space variable x. The order of the integro-differentiation σ is determined from Eqns (11.2) and (11.3) in accordance with the Fermat principle. The space component $\psi(x)$ of the fracton wave function $\Psi(t,x) = \psi(x)\exp(\mathrm{i}\omega t)$ satisfies the stationary equation

$$\omega\psi(x) = -\mathrm{i}^{-\sigma}\Lambda\nabla_x^{\sigma}\psi(x)\,. \tag{11.14}$$

The general solution of this equation [such that $\psi(-x) = \psi(x)$] is given by Mittag-Leffler functions [100]. A solution in elementary functions can be obtained in the following limiting cases ($x \geqslant 0$ is assumed).

1. Central core, $\omega x^{\sigma} \lesssim \Lambda$,

$$\psi_m(x) \sim \exp\left(-\mathrm{i}^{\sigma}\,\frac{\omega x^{\sigma}}{\Lambda\Gamma(1+\sigma)}\right), \tag{11.15}$$

$$\Psi_m(t,x) \sim \exp(\mathrm{i}\omega t)\exp\left(-\mathrm{i}^{\sigma}\,\frac{\omega x^{\sigma}}{\Lambda\Gamma(1+\sigma)}\right), \tag{11.16}$$

$$\left|\Psi_m(t,x)\right|^2 = \left|\psi_m(x)\right|^2 \sim \exp\left(-\frac{2\omega\alpha_m x^{\sigma}}{\Lambda\Gamma(1+\sigma)}\right), \tag{11.17}$$

where $\mathrm{i}^{\sigma} \equiv \cos[\pi\sigma(4m+1)/2] + \mathrm{i}\sin[\pi\sigma(4m+1)/2]$, $m = 0, \pm1, \pm2, \ldots$, and $\alpha_m = \cos[\pi\sigma(4m+1)/2]$ is the real part of i^{σ}. Only solutions for which

$$\alpha_m \equiv \mathrm{Re}\,\mathrm{i}^{\sigma} = \cos\left(\pi\sigma\frac{4m+1}{2}\right) \geqslant 0 \tag{11.18}$$

have physical meaning. Under condition (11.18), the wave function $\Psi_m(t,x)$ takes finite values for all $-\infty \leqslant x \leqslant +\infty$. At $\alpha_m > 0$, the spatial component $\psi_m(x)$ has the shape of a fractional exponential distribution, $|\psi_m(x)| \sim \exp[-(x/\lambda_m)^{\sigma}]$, where $\lambda_m = [\Lambda\Gamma(1+\sigma)/\omega\alpha_m]^{1/\sigma}$. The scale λ_m (i.e., the characteristic core size) determines the localization length of fracton excitations. As follows from Eqns (2.7), (2.10), and (2.15), near the percolation threshold, the exponent $\sigma = (2+\theta)/2$ satisfies the double inequality

$$\frac{1}{\mathcal{C}} \leqslant \sigma \leqslant \frac{\mathcal{S}_n}{\mathcal{C}}\,, \tag{11.19}$$

where $\mathcal{S}_n \equiv \ln(3^n - 1)/\ln 3$ is the Hausdorff dimension of the Cantor cheese in E^n. We note that the upper limit for the parameter σ depends on the topological dimension of the embedding space: $2 \leqslant n \leqslant 5$. Condition (11.19) yields $0.75 \lesssim \sigma \lesssim 1.42$ for $n = 2$ and $0.75 \lesssim \sigma \lesssim 2.23$ for $n = 3$. In the Euclidean limit $\sigma \to 1$, the real part $\alpha_m \to 0$ for all m. Correspondingly, the fracton wave function $\Psi_m(t,x)$ degenerates into a plane (phonon) wave: $\Psi_m(t,x) \to \Psi(t,x) \sim \exp(\mathrm{i}\omega t - \mathrm{i}qx)$.

The fractional exponential distribution $|\psi_m(x)| \sim \exp[-(x/\lambda_m)^{\sigma}]$ for the fracton wave function kernel was first proposed in [188]. A great number of papers, both analytical and numerical (see review [37] and references therein), were later devoted to fractal dynamics in order to determine the parameter σ. (In the notation of Ref. [37], $\sigma \equiv d_{\phi}$). Remarkably, almost all the results in [37] fall within interval (11.19) that reflects fundamental topological properties of fractal structures at the percolation threshold [43].

2. The tail region, $\omega x^{\sigma} \gg \Lambda$. The asymptotic ($\omega x^{\sigma} \gg \Lambda$) investigation of fractal kinetic equation (11.14) is similar to deriving the Levy distribution from the generalized Riesz–Weyl operator [92]. With normalization (11.12), it follows from Eqn (11.14) that

$$\psi_m(x) \sim \left(\frac{\Lambda}{\omega\Gamma(-\sigma)}\right)^{1/2} \times x^{-(\sigma+1)/2}\,, \tag{11.20}$$

$$\Psi_m(t,x) \sim \left(\frac{\Lambda}{\omega\Gamma(-\sigma)}\right)^{1/2} \exp(\mathrm{i}\omega t) \times x^{-(\sigma+1)/2}\,, \tag{11.21}$$

$$\left|\Psi_m(t,x)\right|^2 = \left|\psi_m(x)\right|^2 \sim \frac{\Lambda}{\omega|\Gamma(-\sigma)|} \times x^{-(\sigma+1)}\,. \tag{11.22}$$

Distribution (11.21), (11.22) represents a power-law tail of the fracton wave function $\Psi_m(t,x)$. The tail appears only for fractional values σ in view of the analytic properties of the Riesz–Weyl operator [92]. For $\sigma = 1$ (i.e., for connectivity $\theta = 0$), the tail disappears because the gamma-function diverges, $\Gamma(-1) = \infty$. The slope of the tail (in logarithmic coordinates) is $-(\sigma+1)$. By Eqn (11.19), $1.75 \lesssim (\sigma+1) \lesssim 2.42$ for $n = 2$ and $1.75 \lesssim (\sigma+1) \lesssim 3.23$ for $n = 3$. The relatively slow [$(\sigma+1) \lesssim 3.5$] decay of the fracton wave function for $x^{\sigma} \gg \Lambda/\omega$ indicates a large probability for the fracton to be found outside the central core limits [43].

11.5 Self-squeezing of fracton modes and the fractional parabolic equation

Equations (11.13) and (11.14) are related to 'weak' excitations, for which the dependence of the frequency ω on the amplitude $|\Psi(t,x)|^2$ can be neglected. With increasing wave intensity, nonlinear corrections to the frequency must be taken into account. Restricting ourselves to the lowest order, we set

$$\omega = \omega_0 - \zeta\left|\Psi(t,x)\right|^2, \tag{11.23}$$

where ω_0 corresponds to the linear approximation and the second term is a nonlinear correction. We note that ω_0 has a power-law dependence on the wave number q, Eqn (11.1). Without loss of generality, we assume that the parameter $\zeta = \zeta(q)$ takes positive values $\zeta > 0$ for all q, i.e., the frequency decreases with the amplitude (Fig. 22). Because the amplitude $|\Psi(t,x)|^2$ decays with x [this dependence is due to the nonlocality of the operator ∇_x^{σ} in wave equation (11.13)], under condition (11.23), the fracton phase velocity ω/q increases from the core to the tail of the excitation. Simultaneously, for

$$\frac{\partial^2\omega}{\partial q^2} > 0\,, \tag{11.24}$$

the group velocity $\partial\omega/\partial q$ is always directed such that additional energy flows from the tail to the core during each oscillation. As a result, the fracton profile becomes distorted: oscillations in the core are enhanced, while those in the tail are suppressed (Fig. 22b). This effect can be treated as the self-squeezing (or self-focusing) of a fracton excitation. The phenomenon is analogous to the modulation instability of a plane wave packet with slowly varying amplitude and phase [189]. Replacing ω and q by the respective differential operators $\mathrm{i}\partial/\partial t$ and $-\mathrm{i}\partial/\partial x$, from Eqns (11.1) and (11.2) we obtain the nonlinear kinetic equation for unstable fracton modes:

$$\frac{\mathrm{i}\partial\Psi(t,x)}{\partial t} = \mathrm{i}^{-\sigma}\Lambda\nabla_x^{\sigma}\Psi(t,x) - \zeta\left|\Psi(t,x)\right|^2\Psi(t,x)\,. \tag{11.25}$$

The progressing self-focusing of the fracton is opposed by diffraction, which causes 'smearing' of the core. The narrower the core, the stronger the diffraction effects are. If the medium is sufficiently elastic and the nonlinearity is limited to a small correction to frequency, then further development of the modulation instability is suppressed by diffraction. As a rule, diffraction is associated with the term proportional to the second derivative $\nabla_x^2\Psi(t,x)$; the proportionality coefficient is here equal to one half of $\partial^2\omega/\partial q^2$ [189],

$$\text{d.t.} \sim \frac{1}{2}\left[\frac{\partial^2\omega}{\partial q^2}\right] \times \nabla_x^2\Psi(t,x) \tag{11.26}$$

(d.t. stands for the diffraction term). Equation (11.26) characterizes the diffraction as a 'diffusion' of oscillations with the coefficient $\mathcal{D} \sim \partial^2\omega/2\partial q^2$.

In the context of kinetic equation (4.1), it is relevant to introduce the notion of 'strange diffraction' corresponding to a fractional generalization of Eqn (11.26) with the Riesz–Weyl operator $\nabla_{-x}^{\beta}\nabla_x^{\beta}$ instead of ∇_x^2,

$$\text{d.t.} \sim \frac{1}{2}\left[\frac{\partial^2\omega}{\partial q^2}\right] q^{2-2\beta} \times \nabla_{-x}^{\beta}\nabla_x^{\beta}\Psi(t,x)\,, \tag{11.27}$$

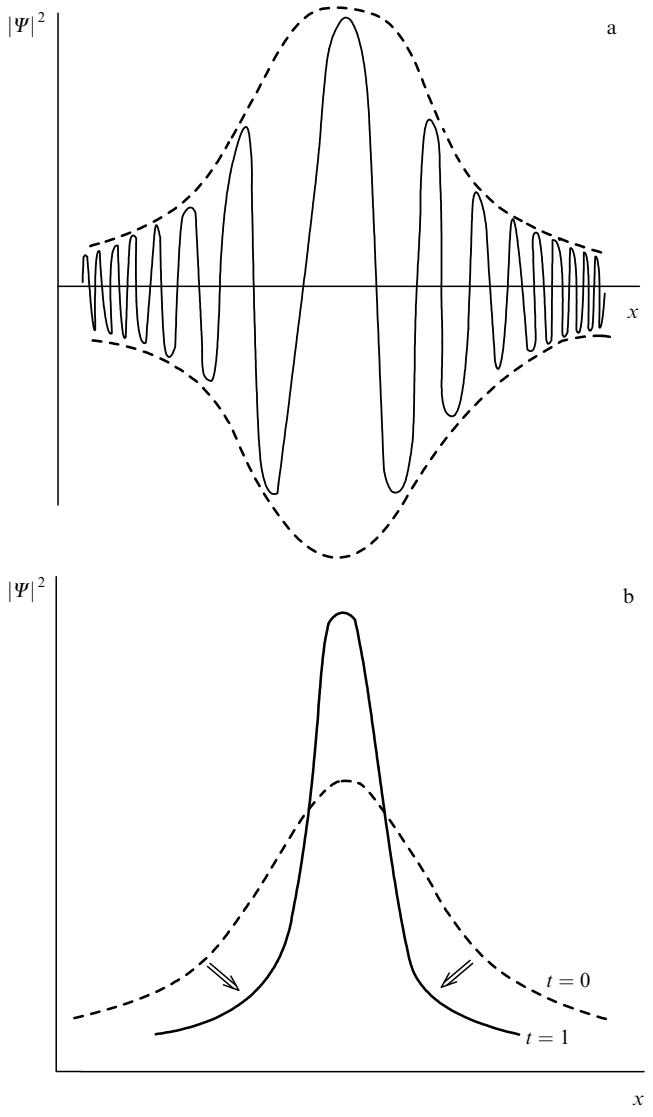

Figure 22. (a) The principal averaged nonlinear effect manifested as fracton oscillations increase is the dependence of the excitation frequency ω on the amplitude $|\Psi(t,x)|^2$. For $\zeta > 0$, the oscillation frequency in the tail exceeds the corresponding value in the central part of the fracton. The envelope of the nonlinear fracton mode is shown by the dashed line. (b) The development of the modulation instability leads to gradual energy transmission from the tail to the core of the fracton excitation. Shown is the position of the envelope at two successive moments of time $t = 0$ and $t = 1$. The phenomenon can be treated as a self-focusing (or self-squeezing) of the nonlinear fracton mode.

where the index β changes from zero to one and the factor $q^{2-2\beta}$ is introduced to preserve the overall dimensionality. The operator $\nabla^{\beta}_{-x}\nabla^{\beta}_{x}$ in Eqn (11.27) provides the necessary invariance of the diffraction term under the reflection symmetry $x \to -x$. The transition to the Riesz–Weyl operator in Eqn (11.27) can be associated with the nonlocality of diffraction effects in fractal media. A physical manifestation of the nonlocality is the strange (nondiffusive) smearing of the central core as the modulation instability develops. The strange diffusion is described by the 'turbulent transport coefficient' $\mathcal{D}_{\beta} \sim [\partial^2\omega/\partial q^2]\, q^{2-2\beta}/2$. The balance between diffraction and nonlinearity, with nonlocal phenomena taken into account, corresponds to fractional kinetic equation (11.25) with the addition of integro-differential term (11.27) describing the strange ('turbulent') diffusion of fracton excitations:

$$\frac{\mathrm{i}\partial\Psi(t,x)}{\partial t} = \mathrm{i}^{-\sigma}\Lambda\nabla^{\sigma}_{x}\Psi(t,x) + \mathcal{D}_{\beta}\nabla^{\beta}_{-x}\nabla^{\beta}_{x}\Psi(t,x) - \zeta\left|\Psi(t,x)\right|^2\Psi(t,x)\,. \tag{11.28}$$

The stabilizing role of diffraction leads to the existence of stationary self-squeezed fracton modes — a result that is quite similar to the well-known principles of nonlinear optics [189]. Equation (11.28) is nothing but a fractional generalization of the parabolic equation describing self-focusing and self-squeezing of wave packets in nonlinear media [189]. The local limit of kinetic equation (11.28) corresponds to the conditions $\sigma \to 1$ and $\beta \to 1$. An important argument for fractional equation (11.28) is the nonlocality (confirmed by direct measurements) of the so-called electrostriction and thermal effects that usually accompany propagation of nonlinear waves in dielectrics [190].

11.6 Self-delocalization of fractons and the fractional nonlinear Schrödinger equation

Up to now, we have assumed that wave excitations have no effect on topological properties of the medium, for example, on its connectedness. An intriguing effect of fracton self-delocalization can be related to changes in connectedness caused by a wave field. We consider this effect to be a theoretical prediction of the fractal model. Basically, the nonlinear dependence of the fracton frequency on the amplitude in this effect leads to an oscillation phase variation from the core to the tail of an excitation. Initial phase inhomogeneities increase with time and at some moment, the fracton 'decays' into oscillators with significantly mixed phases. The phase mixing affects the relative locations of fractal structural elements participating in oscillations. This destroys the nearest-neighbor relation between the elements: initially, neighboring elements can separate in the wave field and the distant ones can converge. This fact is crucial for determination of the connectivity parameter θ that determines the directions of the shortest 'paths' (geodesic lines connecting structural elements of the set) using microscopic characteristics of the fractal medium (for example, the shape of voids, see Section 2). The characteristics disappear at strong mixing and the index θ vanishes:

$$\theta \to 0\,. \tag{11.29}$$

At zero connectivity, conditions requiring the localization of excitations are relaxed and a fracton becomes free. The wave, as it were, creates a certain type of corridor with Euclidean connectedness, along which it freely propagates through the medium. The phenomenon can be treated as a 'strange soliton' for which the fractal distribution is transparent. The kinetic equation describing strange solitons can be easily derived from fractional parabolic equation (11.28) in the limit as

$$\sigma \to 1\,, \tag{11.30}$$

where we have taken Eqn (11.2) for fracton modes into account. The index β, which is responsible for the overall spatial nonlocality of the wave process, should then be

considered fractional, as before:

$$\frac{\mathrm{i}\partial\Psi(t,x)}{\partial t}+\mathrm{i}\Lambda\nabla_x\Psi(t,x)=\mathcal{D}_\beta\nabla_{-x}^{\beta}\nabla_x^{\beta}\Psi(t,x)-\zeta\left|\Psi(t,x)\right|^2\Psi(t,x)\,. \tag{11.31}$$

The time transformation $2t'=t+x/\Lambda$ reduces Eqn (11.31) to the fractional nonlinear Schrödinger equation

$$\frac{\mathrm{i}\partial\Psi(t',x)}{\partial t'}-\mathcal{D}_\beta\nabla_{-x}^{\beta}\nabla_x^{\beta}\Psi(t',x)+\zeta\left|\Psi(t',x)\right|^2\Psi(t',x)=0 \tag{11.32}$$

with the nonlocal operator $\nabla_{-x}^{\beta}\nabla_x^{\beta}$. The fractional nonlinear Schrödinger equation describes strange solitons of envelopes in media with complex microscopic structures, in which the fractal 'pattern' can change due to excitations. The local limit ($\beta\to 1$) of Eqn (11.32) yields the standard Schrödinger equation considered in [191]. Setting $\Psi(t',x)=\psi(x)\exp(-\mathrm{i}\omega t')$ in Eqn (11.32), we arrive at the equation for the envelope

$$-\mathcal{D}_\beta\nabla_{-x}^{\beta}\nabla_x^{\beta}\psi(x)+\omega\psi(x)+\zeta\left|\psi(x)\right|^2\psi(x)=0\,. \tag{11.33}$$

In contrast to Eqn (11.14) containing the complex factor $-\mathrm{i}^{-\sigma}\Lambda$ in front of the Riesz – Weyl operator ∇_x^{σ}, the coefficient $\mathcal{D}_\beta\sim[\partial^2\omega/\partial q^2]\,q^{2-2\beta}/2$ at the nonlocal term $\nabla_{-x}^{\beta}\nabla_x^{\beta}\psi(x)$ in Eqn (11.33) takes strictly real values.

11.7 The fractional Ginzburg – Landau equation

We next consider wave fields that are stable under self-squeezing. In view of condition (11.24), it is sufficient to change the sign of the nonlocal term in Eqns (11.32) and (11.33). The defining equation for the amplitude $\psi(x)$ is

$$\mathcal{D}_\beta\nabla_{-x}^{\beta}\nabla_x^{\beta}\psi(x)+\omega\psi(x)+\zeta\left|\psi(x)\right|^2\psi(x)=0\,. \tag{11.34}$$

The local limit ($\beta\to 1$) of Eqn (11.34) yields the Ginzburg – Landau equation

$$-\mathcal{D}\nabla_x^2\psi(x)+\omega\psi(x)+\zeta\left|\psi(x)\right|^2\psi(x)=0\,, \tag{11.35}$$

which plays the key role in the theory of second-order phase transitions [192]. We say that integro-differential equation (11.34) with the operator $\nabla_{-x}^{\beta}\nabla_x^{\beta}$ is the fractional Landau – Ginzburg equation. In the context of fractional equation (11.34), the quantity $\psi(x)$ can be treated as the order parameter describing coherent formation of a nonlinear wave field (for example, the condensate wave function below the transition point to the superconducting state [104]) due to the long-range correlation effects introducing a significant nonlocality into the behavior of the system as a whole. The nonlocality can then be associated with the macroscopic ordering, which affects the wave process kinetics. An illustration is provided by the widely debated issue of 'stripes' — one-dimensional ordering of charges (charge stripes) and spin (spin stripes) that in superconducting ceramics form a sort of 'runway' along which the condensate conducting liquid can flow without resistance [193 – 195]. At high temperatures, the superconducting current in ceramics can be carried by holes paired on the 'stripe' oscillations [43]. The holes are formed because the conductivity electrons are drawn in the insulating substrates separating the conducting planes [195].

The fractional Ginzburg – Landau equation can be formally derived from the extremum condition of the free energy [104]

$$\mathcal{F}=\mathcal{F}_0+\int_{-\infty}^{+\infty}\mathrm{d}x\left[\mathcal{D}_\beta\left|\nabla_x^{\beta}\psi\right|^2+\omega\left|\psi\right|^2+\frac{\zeta}{2}\left|\psi\right|^4\right] \tag{11.36}$$

with the nonlocal gradient term $\mathcal{D}_\beta|\nabla_x^{\beta}\psi|^2$. Functional (11.36) generalizes the expansion of the free energy $\mathcal{F}$ known in the Landau theory [192] to the case of arbitrary real values $0\leqslant\beta\leqslant 1$. Introducing the fractional differentiation operator in expansion (11.36) corresponds to a non-Gaussian distribution of the order parameter ψ with the power-law density correlator [104]

$$\Im(x)=\frac{\Im_0}{\Gamma(1-\beta)}\times x^{-\beta}\,. \tag{11.37}$$

Equation (11.37) implies that blobs of the 'symmetric' (superconducting fluid) phase corresponding to nonzero values of the order parameter ψ emerge near the transition point not randomly (as in the conventional Landau theory) but in some coherent way such that the probability of finding a blob at a distance x from another one, already found in the medium, decreases with x as $x^{-\beta}$ (as $\exp(-x^2)$ for a Gaussian distribution). In varying the free energy $\mathcal{F}$, the complex-conjugate fields ψ and ψ^* should be treated as independent; this method follows the derivation of the ordinary Ginzburg – Landau equation described in [192].

Varying Eqn (11.36) with respect to ψ^*, we obtain

$$\delta\mathcal{F}=\int_{-\infty}^{+\infty}\mathrm{d}x\left\{\mathcal{D}_\beta\nabla_x^{\beta}\psi\,\nabla_x^{\beta}\delta\psi^*+\omega\psi\delta\psi^*+\zeta|\psi|^2\psi\delta\psi^*\right\}. \tag{11.38}$$

Integrating the nonlocal term $\nabla_x^{\beta}\psi\nabla_x^{\beta}\delta\psi^*$ by parts using the well-known formula [100, 107]

$$\int_{-\infty}^{+\infty}\mathrm{d}y\varphi_1(y)\nabla_y^{\beta}\varphi_2(y)=\int_{-\infty}^{+\infty}\mathrm{d}y\,\varphi_2(y)\nabla_{-y}^{\beta}\varphi_1(y)\,, \tag{11.39}$$

we rearrange Eqn (11.38) as

$$\delta\mathcal{F}=\int_{-\infty}^{+\infty}\mathrm{d}x\left\{\mathcal{D}_\beta\nabla_{-x}^{\beta}\nabla_x^{\beta}\psi+\omega\psi+\zeta|\psi|^2\psi\right\}\delta\psi^*\,. \tag{11.40}$$

Setting $\delta\mathcal{F}=0$ at the extremum point, we arrive at the fractional Ginzburg – Landau equation in form (11.34). The solution of the fractional Ginzburg – Landau equation at $\zeta=0$ is (in the limit of large $|x|$) the Levy distribution, which we have already met in the context of kinetic equation (4.1). In fact, using explicit integro-differential representation (4.5) for the Riesz – Weyl operator ∇_x^{β} and taking natural normalization condition (11.12) into account, we find from fractional Ginzburg – Landau equation (11.34) that

$$\psi(x)\big|_{\zeta=0}\propto\frac{1}{|x|^{1+2\beta}}\,,\quad |x|\to\infty\,. \tag{11.41}$$

The derivation of the fractional Ginzburg – Landau equation from the free energy extremum illustrates the methods of strange kinetics in light of fundamental variational principles underlying modern theoretical physics. The fractional Ginzburg – Landau equation is applied in the high-temperature

superconductivity model [104] in which the condensate wave function $\psi(x)$ can acquire the necessary 'strength' due to the nonlocal symmetries 'keeping' the quantum liquid in the superconducting state. The balance between the nonlinearity ($\zeta|\psi|^2\psi$) and the nonlocality ($\mathcal{D}_\beta \nabla^\beta_{-x} \nabla^\beta_x \psi$) in Eqn (11.34) then provides (at the characteristic correlation length $a \sim 10^{-6}$ cm and the Fermi surface energy $\varepsilon_F \sim 3$ eV) the superconducting phase stability at absolute temperatures of the order of $T_c \sim 180$ K [104].

11.8 Topological nonlinear 'Landau damping' and the percolation constant

The self-delocalization effect can be associated with an 'elastic' perturbation of connectedness in the wave field. The soliton runs the track along which the excitation depresses spatial inhomogeneities of the medium. Fractality is restored behind the wave front, and hence the pulse propagation does not induce irreversible changes of the medium as such. The situation becomes quite different if fractons interact with the medium inelastically. In fact, by virtue of the Le Chatelieur principle, the medium response is then aimed at suppressing the fracton excitations. A consequence of this is a structural reorganization of the medium towards some 'resonant' distribution on which fractons experience strong scattering; a sort of topological 'Landau damping', caused by energy losses to a redistribution of fractal set elements under the action of (quasi)-acoustic oscillation eigenmodes, is observed.

We suppose that the structural reorganization of the medium in the fracton excitation field results in a new percolating fractal set F whose topology is described by the Hausdorff dimension d_f and the connectivity index θ. We assume that the system evolves to some NESS under the action of the wave ensemble. By the universal value theorem, we can then write condition (2.10) for d_f and θ. If the amplitude of the waves is sufficiently large, phase mixing occurs and $\theta \to 0$, Eqn (11.29). As follows from Eqns (11.15)–(11.17) and (11.20)–(11.22), the fracton wave function then degenerates into a plane wave: $\Psi_m(t,x) \propto \exp(i\omega t - iqx)$. On the other hand, if the topological dissipation on the whole is 'stronger' than the nonlinearity, the plane waves resulting from the fracton excitation decay simply have no time to form a soliton. Because the solutions of the form $\Psi_m(t,x) \propto \exp(i\omega t - iqx)$ are not eigenmodes of a fractal distribution [183], all radiation is scattered on spatial inhomogeneities of the medium within a short time interval (of the order of $1/\omega$). Combining Eqns (2.7) and (2.10), from condition $\theta \to 0$ we obtain the Hausdorff dimension of the set resonating with fracton excitations:

$$d_f \to \mathcal{C} \approx 1.327\ldots \sim \frac{4}{3}\,. \tag{11.42}$$

That this value coincides with the percolation constant $\mathcal{C}$ is a remarkable analytical result! The unconventional properties of distribution (11.42) were already discussed in Section 3 in studying non-Gaussian diffusion processes. In the context of wave processes, distribution (11.42) plays the role of a 'dissipative attractor' on which fracton excitations decay within a time scale of the order of the inverse oscillation frequency.

11.9 A fracton solar wind model

The mechanism of the topological 'Landau damping' can be applied to the formation of the fractal structure of the interplanetary magnetic field, influenced by magnetosonic fracton excitations. We here mean the possibility of a collective reorganization of the turbulent magnetic field clots such that it allows damping the oscillations that appear in the solar wind at the early stage of the expansion of the corona [52–54]. The structural reorganization of the field resonating with fractons results in the formation of clusters with the Hausdorff dimension d_f close to (11.42). The value $d_f \sim 4/3$ agrees with the aggregation model prediction [128, 129, 165] on the evolution of fractal geometry of clusters towards a universal distribution with Hausdorff dimension (10.2).

We recall that the convection of a fractal distribution with solar wind streams is interpreted by a rest-frame observer as self-affine variations of the field in time. The spectral power-law exponent for distribution (11.42) can easily be derived from formula (5.31):

$$\varpi = 2\mathcal{C} - 1 \approx 1.65\ldots \sim \frac{5}{3}\,. \tag{11.43}$$

Correspondingly, the fluctuation spectrum $P(f)$ is given by

$$P(f) \sim f^{-5/3}\,, \tag{11.44}$$

which brings us back to Eqn (10.4). By incorporating wave processes, the fracton model predicts the formation of the 'Kolmogorov' spectra of form (11.44) at smaller heliocentric distances than in 'pure' aggregation models [128, 129, 165]. This result agrees with the observed properties of the turbulent solar wind at heliocentric distances $R \sim 0.3$ a.u. [178]. The value of f in Eqn (11.44) exhibits the Doppler broadening that allows a small frequency 'smearing'

$$f \gtrsim f_* \sim \frac{|u \pm c_\sigma|}{\xi}\,, \tag{11.45}$$

where u is the convection velocity. With u assumed large compared to the phase velocity of fractons c_σ, inequality (11.45) implies estimate (10.5).

12. Conclusion

We have discussed a nontraditional analytic approach to the investigation of strong turbulence in complex nonlinear dynamical systems far from thermal equilibrium. This approach synthesizes the fractional dynamics and fractal topology, two nonstandard mathematical methods embodying the paradigms of the modern theory of turbulence and chaos. Combination of these methods allows unifying the kinetic and geometric characteristics of a turbulent ensemble, which opens up a path to the self-consistent description of its basic statistical properties. The connecting link between topology and kinetics is the notion of a nonequilibrium (quasi)-stationary state of a turbulent system. The stability of this state (both structural and dynamical) is provided by multi-scale correlations in space and time. The transition to the NESS is a complex compromise between self-organization mechanisms, which determine the tendencies of evolutionary processes in the system, and dynamical relaxation effects, which reflect the role of dissipative factors in the medium. The NESS topology represents a percolating (infinitely path-connected) fractal set lying 'at the percolation threshold' (i.e., near the critical point below which dynamical processes in the medium are limited within a finite domain of the phase space). The existence of the threshold is related to a number of

remarkable properties of nonequilibrium (quasi)-stationary states of the turbulent ensemble. These properties are expressed in the existence of a universal constant, the percolation constant $\mathcal{C}$, which is approximately equal to $1.327\ldots$.

In the context of turbulence theory, the percolation constant $\mathcal{C} \approx 1.327\ldots$ can be considered a universal value of the NESS spectral dimension. If the spectral dimension is known, two thirds of the useful information on the turbulent ensemble kinetics is available to us (one third of the information is contained in the Hausdorff dimension value, which is system-specific). We emphasize that the value $\mathcal{C} \approx 1.327\ldots$ automatically accounts for contributions from multi-scale correlations, which prevail in NESS formation. The study of correlations by other methods (for example, directly from microscopic equations of motion for individual particles) usually encounters severe analytical difficulties; the introduction of the percolation constant therefore significantly extends the possibilities for the analytic description of turbulence.

Among the general (independent of physical nature) properties of the NESS, we note the tendency to self-organized criticality. As is well known, the transition of a system to SOC is accompanied by the appearance of the characteristic rose noise $\sim f^{-1}$ at low frequencies. The SOC phenomenon can be understood in the context of fundamental physical principles, for example, the minimum-action principle. As the frequency increases, noises become darker, which is due to an increasing influence of structural properties of turbulence on the spectral energy distribution. The noise color at intermediate frequencies is fully determined by the Hausdorff dimension of the ensemble, and the color difference of the spectra is determined by specifics of physical processes controlling the NESS formation. At large values of the β parameter for plasma, the low-frequency rose noise $\sim f^{-1}$ indicates the existence of strange Fermi processes in the system. The strange Fermi acceleration gives rise to a population of energetic particles with a power-law energy distribution $\propto \mathcal{E}^{-\eta}$ with the exponent $6 \leqslant \eta < 7$. This result is in good agreement with the known phenomenological distributions of high-energy charged particles in the earth's magnetotail.

Acknowledgments. We are indebted to our Russian and foreign colleagues F Chiaravalloti, G Consolini, A A Galeev, A Greco, E Lazzaro, M Lontano, E I Mogilevsky, A I Neistadt, H Pecseli, A A Petrukovich, J J Rasmussen, K Rypdal, A L Taktakishvili, V Yu Trahtengertz, P Veltri, I S Veselovsky, G M Zaslavsky, G N Zastenker, and G Zimbardo for numerous and lively discussions on various aspects of the modern theory of turbulence discussed in this review This work was sponsored by the Science Support Foundation, the Russian Foundation for Basic Research (project 03-02-16967), the INTAS (grant 03-51-3738) and Minpromnauka (grant No NSh-1739.2003.2).

13. Appendix. Notation and abbreviations

E^n — n-dimensional Euclidean space,
F — fractal subset of the space E^n,
d_{f} — Hausdorff fractal dimension,
d_{s} — spectral fractal dimension,
d_θ — Hausdorff dimension of geodesic lines,
d_w — fractal dimension of dynamical trajectories,
θ — connectivity index of a fractal structure,
$\mathcal{C}$ — percolation constant,
Γ — Euler gamma-function,
$\mathcal{S}_n$ — Hausdorff dimension of the n-dimensional Cantor cheese in E^n,
$\mathcal{O}(t)$ — correlator of the past and future increments of a fluctuating variable,
$\mathcal{I}_S(t)$ — statistically self-affine time series,
δ_{f} — Hausdorff dimension of a time series,
S — similarity index,
J — completion of S to 1,
H — transport process index (along with $\mu = 2H$) ,
Ξ_{f} — topological entropy,
α — fractal time differentiation index,
β — fractal phase variable differentiation index,
$\mathcal{D}$ — turbulent transport coefficient,
Ω — solid angle,
P — Fourier transformation,
ϖ — power spectrum exponent,
ξ — correlation length for a fractal distribution,
a — elementary size of a turbulent field fluctuation,
NESS — nonequilibrium (quasi)-stationary state,
FTRW — fractal-time random walk,
SOC — self-organized criticality,
a.u. — astronomical unit (distance from the sun to the earth, 1 a.u $= 1.5 \times 10^{13}$ cm).

References

1. Hausdorff F *Math. Ann.* **79** 157 (1919)
2. Besicovitch A S *Math. Ann.* **101** 161 (1929)
3. Besicovitch A S *J. London Math. Soc.* **9** 126 (1934)
4. Besicovitch A S *Math. Ann.* **110** 321 (1935)
5. Good I J *Proc. Camb. Philos. Soc.* **37** 199 (1941)
6. Mandelbrot B B *Science* **155** 636 (1967)
7. Mandelbrot B B *Fractals: Form, Chance, and Dimension* (San Francisco: W.H. Freeman, 1977)
8. Mandelbrot B B *The Fractal Geometry of Nature* (San Francisco: W.H. Freeman, 1982) [Translated into Russian (Moscow: Institut Komp'yuternykh Issledovaniĭ, 2001)]
9. Feder J *Fractals* (New York: Plenum Press, 1988) [Translated into Russian (Moscow: Mir, 1991)]
10. McCauley J L *Phys. Rep.* **189** 225 (1990)
11. Paladin G, Vulpiani A *Phys. Rep.* **156** 147 (1987)
12. Peebles P J E *Physica D* **38** 273 (1989)
13. Coleman P H, Pietronero L *Phys. Rep.* **213** 311 (1992)
14. Labini S F, Montuori M, Pietronero L *Phys. Rep.* **293** 61 (1998)
15. Zaslavskiĭ G M, Sagdeev R Z *Vvedenie v Nelineĭnuyu Fiziku: ot Mayatnika do Turbulentnosti i Khaosa* (Introduction to Non-linear Physics: from Pendulum to Turbulence and Chaos) (M.: Nauka, 1988); see also Sagdeev R Z, Usikov D A, Zaslavsky G M *Nonlinear Physics: from the Pendulum to Turbulence and Chaos* (Chur: Harwood Acad. Publ., 1988)
16. Crownover R M *Introduction to Fractals and Chaos* (Boston: Jones and Bartlett, 1995) [Translated into Russian (Moscow: Postmarket, 2000)]
17. Sreenivasan K R, Prasad R R *Physica D* **38** 322 (1986)
18. Frisch U *Turbulence. The Legacy of A.N. Kolmogorov* (Cambridge: Cambridge Univ. Press, 1995) [Translated into Russian (Moscow: FAZIS, 1998)]
19. Gefen Y, Mandelbrot B B, Aharony A *Phys. Rev. Lett.* **45** 855 (1980)
20. Suzuki M *Prog. Theor. Phys.* **69** 65 (1983)
21. Havlin S, ben-Avraham D *Adv. Phys.* **36** 695 (1987)
22. ben-Avraham D, Havlin S *Diffusion and Reactions in Fractals and Disordered Systems* (Cambridge: Cambridge Univ. Press, 2000)
23. Bouchaud J-P, Georges A *Phys. Rep.* **195** 127 (1990)
24. Aharony A, Feder J (Eds) *Fractals in Physics: Essays in Honour of Benoit B. Mandelbrot: Proc. of the Intern. Conf. Honouring Benoit B.*

Mandelbrot on His 65th Birthday, Vence, France, 1–4 October 1989 (Amsterdam: North-Holland, 1990)
25. Pietronero L, Tosatti E (Eds.) *Fractals in Physics*: *Proc. of the 6th Triste Intern. Symp., Trieste, Italy, July 9–12, 1985* (Amsterdam: North-Holland, 1986) [Translated into Russian (M.: Mir, 1988)]
26. Takayasu H *Fractals in the Physical Sciences* (Manchester: Manchester Univ. Press, 1990)
27. Le Méhauté A *Fractal Geometries*: *Theory and Applications* (Boca Raton: CRC Press, 1991)
28. Schroeder M R *Fractals, Chaos, Power Laws*: *Minutes from an Infinite Paradise* (New York: W.H. Freeman, 1991) [Translated into Russian (Izhevsk: RKhD, 2001)]
29. Morozov A D *Vvedenie v Teoriyu Fraktalov* (Introduction to Theory of Fractals) (Moscow-Izhevsk: Institut Komp'yuternykh Issledovaniĭ, 2002)
30. Bozhokin S V, Parshin D A *Fraktaly i Mul'tifraktaly* (Fractals and Multifractals) (Izhevsk: RKhD, 2001)
31. Shklovskii B I, Efros A L *Electronic Properties of Doped Semiconductors* (Berlin: Springer-Verlag, 1984)
32. Stauffer D *Introduction to Percolation Theory* (London: Taylor & Francis, 1985)
33. Stauffer D, Aharony A *Introduction to Percolation Theory* 2nd ed. (London: Taylor & Francis, 1992)
34. Shante V K S, Kirkpatrick S *Adv. Phys.* **20** 325 (1971)
35. Stauffer D *Phys. Rep.* **54** 1 (1979)
36. Isichenko M B *Rev. Mod. Phys.* **64** 961 (1992)
37. Nakayama T, Yakubo K, Orbach R L *Rev. Mod. Phys.* **66** 381 (1994)
38. Alexander S, Orbach R L *J. Phys. Lett.* (Paris) **43** L625 (1982)
39. Coniglio A *J. Phys. A*: *Math. Gen.* **15** 3829 (1982)
40. Milovanov A V *Phys. Rev. E* **56** 2437 (1997)
41. Milovanov A V, Zimbardo G *Phys. Rev. E* **62** 250 (2000)
42. Milovanov A V, Rasmussen J J *Phys. Rev. B* **64** 212203 (2001)
43. Milovanov A V, Rasmussen J J *Phys. Rev. B* **66** 134505 (2002)
44. Dubrovin B A, Novikov S P, Fomenko A T *Sovremennaya Geometriya* (Modern Geometry) (Moscow: Nauka, 1979) [Translated into English: Dubrovin B A, Fomenko A T, Novikov S P *Modern Geometry*: *Methods and Applications* (New York: Springer-Verlag, 1984)]
45. Hirsch M W *Differential Topology* (New York: Springer-Verlag, 1976) [Translated into Russian (Moscow: Mir, 1979)]
46. Fomenko A T, Fuks D B *Kurs Gomotopicheskoĭ Topologii* (Course of Homotopic Topology) (Moscow: Nauka, 1989)
47. Milovanov A V et al. *J. Geophys. Res.* **106** 6291 (2001)
48. Rypdal K et al. *Nonlinear Proces. Geophys.* **10** 139 (2003)
49. Milovanov A V, Zelenyi L M, Zimbardo G *J. Geophys. Res.* **101** 19903 (1996)
50. Zelenyi L M, Milovanov A V, Zimbardo G, in *New Perspectives on the Earth's Magnetotail* (Geophys. Monograph, Vol. 105, Eds A Nishida, D N Baker, S W H Cowley) (Washington, DC: Am. Geophys. Union, 1998) p. 321
51. Milovanov A V et al. *J. Atmos. Sol.-Terr. Phys.* **63** 705 (2001)
52. Milovanov A V, Zelenyi L M *Phys. Space Plasmas* **14** 373 (1995)
53. Zelenyi L M, Milovanov A V *Geomag. Aeronomiya* **37** (1) 1 (1997) [*Geomag. Aeronomy* **37** 1 (1997)]
54. Milovanov A V, Zelenyi L M *Astrophys. Space Sci.* **264** 317 (1998)
55. Tetreault D *J. Geophys. Res.* **97** 8531 (1992)
56. Tetreault D *J. Geophys. Res.* **97** 8541 (1992)
57. Treumann R A *Phys. Scripta* **59** 19 (1999)
58. Treumann R A *Phys. Scripta* **59** 204 (1999)
59. Gefen Y, Aharony A, Alexander S *Phys. Rev. Lett.* **50** 77 (1983)
60. O'Shaughnessy B, Procaccia I *Phys. Rev. Lett.* **54** 455 (1985)
61. O'Shaughnessy B, Procaccia I *Phys. Rev. A* **32** 3073 (1985)
62. Giona M, Roman H E *Physica A* **185** 87 (1992)
63. Zaslavsky G M et al. *Phys. Plasmas* **7** 3691 (2000)
64. Chiaravalloti F, Milovanov A V, Zimbardo G *Phys. Scripta* (to be published) (2004); cond-mat/0404648 (v1)
65. Clement E, Kopelman R, Sander L M *J. Stat. Phys.* **65** 919 (1991)
66. La Porta A et al. *Nature* **409** 1017 (2001)
67. Kolmogorov A N *Dokl. Akad. Nauk SSSR* **119** 861 (1958)
68. Milovanov A V et al. *Kosmich. Issled.* **34** 451 (1996) [*Cosmic. Res.* **34** 415 (1996)]
69. Burlaga L F, Klein L W *J. Geophys. Res.* **91** 347 (1986)
70. Milovanov A V, Thesis for Doctorate of Physicomathematical Sciences (Moscow: Space Research Institute, 2003)
71. Boltyanskiĭ V G, Efremovich V A *Naglyadnaya Topologiya* (Visual Topology) (Moscow: Nauka, 1983) [Translated into English: *Intuitive Combinatorial Topology* (New York: Springer, 2001)]
72. van Kampen N G *Stochastic Processes in Physics and Chemistry* (Amsterdam: North-Holland, 1981) [Translated into Russian (Moscow: Vysshaya Shkola, 1990)]
73. Carreras B A et al. *Phys. Rev. Lett.* **80** 4438 (1998)
74. Carreras B A et al. *Phys. Rev. Lett.* **83** 3653 (1999)
75. Elhmaidi D, Provenzale A, Babiano A *J. Fluid Mech.* **242** 655 (1993)
76. Provenzale A *Annu. Rev. Fluid Mech.* **31** 55 (1999)
77. Nielsen A H, Pécseli H L, Rasmussen J J *Phys. Plasmas* **3** 1530 (1996)
78. Naulin V, Nielsen A H, Rasmussen J J *Phys. Plasmas* **6** 4575 (1999)
79. Milovanov A V, Zelenyi L M *Phys. Fluids B* **5** 2609 (1993)
80. Bolshov L A, Dykhne A M, Kondratenko P S *Pis'ma Zh. Eksp. Teor. Fiz.* **75** 291 (2002) [*JETP Lett.* **75** 246 (2002)]
81. Klafter J, Blumen A, Shlesinger M F *Phys. Rev. A* **35** 3081 (1987)
82. Zimbardo G, Greco A, Veltri P *Phys. Plasmas* **7** 1071 (2000)
83. Zimbardo G, Veltri P, Pommois P *Phys. Rev. E* **61** 1940 (2000)
84. Milovanov A V *Phys. Rev. E* **63** 047301 (2001)
85. Klafter J, Shlesinger M F, Zumofen G *Phys. Today* **49** (2) 33 (1996)
86. Shlesinger M F, Zaslavsky G M, Klafter J *Nature* **363** 31 (1993)
87. Montroll E W, Shlesinger M F, in *Nonequilibrium Phenomena II*: *from Stochastics to Hydrodynamics* (Studies in Statistical Mechanics, Vol. 11, Eds J Lebowitz, E W Montroll) (Amsterdam: North-Holland Phys. Publ., 1984) p. 1
88. Hughes B D, Montroll E W, Shlesinger M F *J. Stat. Phys.* **28** 111 (1982)
89. Scher H, Shlesinger M F, Bendler J T *Phys. Today* **44** (1) 26 (1991)
90. Mandelbrot B B, van Ness J W *SIAM Rev.* **10** 422 (1968)
91. Zaslavsky G M *Physica D* **76** 110 (1994)
92. Metzler R, Klafter J *Phys. Rep.* **339** 1 (2000)
93. Zaslavsky G M *Phys. Rep.* **371** 461 (2002)
94. Sokolov I M, Klafter J, Blumen A *Phys. Today* **55** (11) 48 (2002)
95. Chukbar K V *Zh. Eksp. Teor. Fiz.* **108** 1875 (1995) [*JETP* **81** 1025 (1995)]
96. Hilfer R *Phys. Rev. E* **48** 2466 (1993)
97. Zaslavsky G M *Physica A* **288** 431 (2000)
98. Weitzner H, Zaslavsky G M *Chaos* **11** 384 (2001)
99. Milovanov A V, Zelenyi L M *Phys. Rev. E* **64** 052101 (2001)
100. Nakhushev A M *Drobnoe Ischislenie i Ego Primenenie* (Fractional Calculus and its Application) (Moscow: Fizmatlit, 2003)
101. Biler P, Funaki T, Woyczynski W A *J. Differ. Equat. Appl.* **148** 9 (1998)
102. Hilfer R (Ed.) *Applications of Fractional Calculus in Physics* (Singapore: World Scientific, 2000)
103. Buttner H, Blumen A *Nature* **329** 700 (1987)
104. Milovanov A V, Rasmussen J J, cond-mat/0309577; submitted for publ. to *Phys. Rev. B*
105. Vladimirov V S *Uravneniya Matematicheskoĭ Fiziki* (Equations of Mathematical Physics) 5th ed. (Moscow: Nauka, 1988) [Translated into English (Moscow: Mir Publ., 1984)]
106. Oldham K B, Spanier J *The Fractional Calculus*; *Theory and Applications of Differentiation and Integration to Arbitrary Order* (New York: Academic Press, 1974)
107. Samko S G, Kilbas A A, Marichev O I *Integraly i Proizvodnye Drobnogo Poryadka i Nekotorye Ikh Prilozheniya* (Fractional Integrals and Derivatives and some Applications (Minsk: Nauka i Tekhnika, 1987) [Translated into English: *Fractional Integrals and Derivatives*: *Theory and Applications* (Philadelphia, Pa.: Gordon and Breach Sci. Publ., 1993)]
108. Monin A S *Dokl. Akad. Nauk SSSR* **105** 256 (1955)
109. Monin A S, Yaglom A M *Statisticheskaya Gidromekhanika* (Statistical Fluid Mechanics) Vol. 2 (Moscow: Nauka, 1967) [Translated into English (Cambridge, Mass.: MIT Press, 1975)]
110. Zaburdaev V Yu, Chukbar K V *Zh. Eksp. Teor. Fiz.* **121** 299 (2002) [*JETP* **94** 252 (2002)]
111. Jespersen S, Metzler R, Fogedby H C *Phys. Rev. E* **59** 2736 (1999)
112. Bak P, Tang C, Wiesenfeld K *Phys. Rev. Lett.* **59** 381 (1987)
113. Bak P, Tang C, Wiesenfeld K *Phys. Rev. A* **38** 364 (1988)
114. Vespignani A, Zapperi S *Phys. Rev. E* **57** 6345 (1998)

115. Krommes J A *Phys. Plasmas* **7** 1752 (2000)
116. Jensen H J *Self-Organized Criticality: Emergent Complex Behavior in Physical and Biological Systems* (Cambridge: Cambridge Univ. Press, 1998)
117. Mogilevskiĭ E I *Fraktaly na Solntse* (Fractals on the Sun) (Moscow: Fizmatlit, 2001)
118. Diamond P H, Hahm T S *Phys. Plasmas* **2** 3640 (1995)
119. Newman D E et al. *Phys. Plasmas* **3** 1858 (1996)
120. Garbet X, Waltz R E *Phys. Plasmas* **5** 2836 (1998)
121. Freeman M P, Watkins N W, Riley D J *Phys. Rev. E* **62** 8794 (2000)
122. Consolini G, Lui A T Y *Geophys. Res. Lett.* **26** 1673 (1999)
123. Chang T *Phys. Plasmas* **6** 4137 (1999)
124. Charbonneau P et al. *Solar Phys.* **203** 321 (2001)
125. Berry M V *J. Phys. A: Math. Gen.* **12** 781 (1979)
126. Ohtani S et al. *J. Geophys. Res.* **100** 19135 (1995)
127. Potapov A A *Fraktaly v Radiofizike i Radiolokatsii* (Fractals in Radiophysics and Radiolocation) (Moscow: Logos, 2002)
128. Milovanov A V, Zelenyi L M *Adv. Space Res.* **14** (7) 123 (1994)
129. Milovanov A V, Zelenyi L M, in *Solar System Plasmas in Space and Time* (Geophys. Monograph, Vol. 84, Eds J Burch, J H Waite (Jr)) (Washington, DC: Am. Geophys. Union, 1994) p. 43
130. Milovanov A V, Zelenyi L M *Adv. Space Res.* **30** 2667 (2002)
131. Zelenyi L M et al. *Nonlinear Proces. Geophys.* **7** 127 (2000)
132. Lui A T Y, Yoon P H *J. Geophys. Res.* **100** 19147 (1995)
133. Ohtani S et al. *J. Geophys. Res.* **103** 4671 (1998)
134. Paterson W R, Frank L A *Geophys. Res. Lett.* **21** 2971 (1994)
135. Lui A T Y *J. Geophys. Res.* **98** 13423 (1993)
136. Galeev A A, Zelenyi L M *Pis'ma Zh. Eksp. Teor. Fiz.* **25** 407 (1977) [*JETP Lett.* **25** 380 (1977)]
137. Coppi B, Laval G, Pellat R *Phys. Rev. Lett.* **16** 1207 (1966)
138. Nishida A et al. *Geophys. Res. Lett.* **21** 2951 (1994)
139. Hoshino M et al. *Geophys. Res. Lett.* **21** 2935 (1994)
140. Bauer T M et al. *J. Geophys. Res.* **100** 9605 (1995)
141. Russell C T *Planet. Space Sci.* **20** 1541 (1972)
142. Borovsky J E et al. *J. Plasma Phys.* **57** 1 (1997)
143. Borovsky J E et al. *J. Geophys. Res.* **103** 20297 (1998)
144. Milovanov A V, Zelenyi L M *Nonlinear Proces. Geophys.* **7** 211 (2000)
145. Lifshitz E M, Pitaevskiĭ L P *Fizicheskaya Kinetika* (Physical Kinetics) (Moscow: Nauka, 1979) [Translated into English (Oxford: Pergamon Press, 1981)]
146. Harris E G *Nuovo Cimento* **23** 115 (1962)
147. Landau L D, Lifshitz E M *Statisticheskaya Fizika* (Statistical Physics) (Moscow: Nauka, 1964) [Translated into English (Oxford: Pergamon Press, 1969)]
148. Lui A T Y, Najmi A-H *Geophys. Res. Lett.* **24** 3157 (1997)
149. Christon S P et al. *J. Geophys. Res.* **94** 13409 (1989)
150. Berezinskiĭ V S et al. *Astrofizika Kosmicheskikh Lucheĭ* (Astrophysics of Cosmic Rays) (Ed. V L Ginzburg) 2nd ed. (Moscow: Nauka, 1990) [Translated into English (Amsterdam: North-Holland, 1990)]
151. Zaslavskiĭ G M *Statisticheskaya Neobratimost' v Nelineĭnykh Sistemakh* (Statistical Irreversibility in Non-linear Systems) (Moscow: Nauka, 1970)
152. Fermi E *Phys. Rev.* **75** 1169 (1949)
153. Glockle W G, Nonnenmacher T F *J. Stat. Phys.* **71** 755 (1993)
154. Hasegawa A, Mima K, Duong-van M *Phys. Rev. Lett.* **54** 2608 (1985)
155. Ma C-Y, Summers D *Geophys. Res. Lett.* **25** 4099 (1998)
156. Zelenyi L M, Milovanov A V *Astron. Zh.* **69** 147 (1992) [*Sov. Astron.* **36** 74 (1992)]
157. Summers D, Thorne R M *J. Geophys. Res.* **97** 16827 (1992)
158. Collier M R *Geophys. Res. Lett.* **20** 1531 (1993)
159. Maksimovic M, Pierrard V, Lemaire J F *Astron. Astrophys.* **324** 725 (1997)
160. Ptuskin V S *Space Sci. Rev.* **111** 1 (2000)
161. Zelenyi L M, Milovanov A V *Pis'ma Astron. Zh.* **17** 1013 (1991) [*Sov. Astron. Lett.* **17** 425 (1991)]
162. Jullien R *Usp. Fiz. Nauk* **157** 339 (1989)
163. Smirnov B M *Fizika Fraktal'nykh Klasterov* (Physics of Fractal Clusters) (Moscow: Nauka, 1991)
164. Zelenyi L M, Milovanov A V *Pis'ma Astron. Zh.* **18** 622 (1992) [*Sov. Astron. Lett.* **18** 249 (1992)]
165. Zelenyi L M, Milovanov A V *Geomag. Aeronomiya* **33** 18 (1993)
166. Tajima T et al. *Astrophys. J.* **390** 309 (1992)
167. Tajima T, Cable S, Kulsrud R M *Phys. Fluids B* **4** 2338 (1992)
168. Cable S, Tajima T *Phys. Rev. A* **46** 3413 (1992)
169. Milovanov A V *Astron. Zh.* **71** 360 (1994) [*Astron. Rep.* **38** 314 (1994)]
170. Priest E R *Solar Magneto-Hydrodynamics* (Dordrecht: D. Reidel Publ. Co., 1984) [Translated into Russian (Moscow: Mir, 1985)]
171. Bray R J, Loughhead R E *Sunspots* (New York: Dover Publ., 1979) [Translated into Russian (Moscow: Mir, 1985)]
172. Milovanov A V, Zelenyi L M *Geophys. Res. Lett.* **19** 1419 (1992)
173. Parker E N *Astrophys. J.* **128** 664 (1958)
174. Burlaga L F, Mish W H, Roberts D A *J. Geophys. Res.* **94** 177 (1989)
175. Roberts D A, Goldstein M L *J. Geophys. Res.* **92** 10105 (1987)
176. Burlaga L F *Geophys. Res. Lett.* **18** 69 (1991)
177. Burlaga L F *Geophys. Res. Lett.* **18** 1651 (1991)
178. Tu C-Y, Marsch E, Thieme K M *J. Geophys. Res.* **94** 11739 (1989)
179. Tarbell T et al. *Bull. Am. Astron. Soc.* **22** 878 (1990)
180. Eselevich M V, Eselevich V G *Astron. Astrophys.* (2004) (to be published)
181. Mel'nikov Yu P *Geomag. Aeronomiya* (2004) (in press)
182. Anderson P W *Phys. Rev.* **109** 1492 (1958)
183. Orbach R *Physica D* **38** 266 (1989)
184. Courtens E, Vacher R, Stoll E *Physica D* **38** 41 (1989)
185. Aharony A et al. *Phys. Rev. Lett.* **58** 132 (1987)
186. Zosimov V V, Lyamshev L M *Usp. Fiz. Nauk* **165** 361 (1995) [*Phys. Usp.* **38** 347 (1995)]
187. Prester M *Phys. Rev. B* **60** 3100 (1999)
188. Entin-Wohlman O, Alexander S, Orbach R *Phys. Rev. B* **32** 8007 (1985)
189. Kadomtsev B B *Kollektivnye Yavleniya v Plazme* (Collective Phenomena in Plasma) (Moscow: Nauka, 1988) [Translated into English: "Cooperative effects in plasmas", in *Reviews of Plasma Physics* Vol. 22 (Ed. V D Shafranov) (New York: Kluwer Acad./ Cosultants Bureau, 2001) p. 1]
190. Akhmanov S A, Khokhlov R V, Sukhorukov A P, in *Laser Handbook* Vol. 1 (Eds F T Arecchi, E O Schulz-Dubois) (Amsterdam: North-Holland, 1972)
191. Ablowitz M J, Segur H *Solitons and the Inverse Scattering Transform* (Philadelphia: SIAM, 1981) [Translated into Russian (Moscow: Mir, 1987)]
192. Lifshitz E M, Pitaevsky L P *Statisticheskaya Fizika* (Statistical Physics) Pt. 2 *Teoriya Kondensirovannogo Sostoyaniya* (Theory of Condensed Matter) (Moscow: Nauka 1978) [Translated into English (Oxford: Pergamon Press, 1980)]
193. Kivelson S A, Fradkin E, Emery V J *Nature* **393** 550 (1998)
194. Ando Y et al. *Phys. Rev. Lett.* **88** 137005 (2002)
195. Cho A *Phys. Rev. Focus* **9** story 12 (2002)